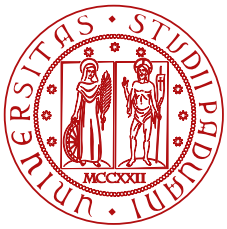

UNIVERSITÀ DEGLI STUDI DI PADOVA

UNIVERSITÀ DEGLI STUDI DI PADOVA

Dipartimento di Ingegneria Industriale DII

Corso di Laurea Magistrale in Ingegneria dell'Energia Elettrica

Numerical Methods for Topology Optimization in Electromagnetics

Relatore:
Dr. Francesco Lucchini

Correlatore:
Dr. Riccardo Torchio

Laureanda:
Caterina Bernardini
2020607

Anno Accademico: 2023/2024

"Pour élever quelqu'un, enfant ou adulte, il faut d'abord l'élever à ses propres yeux"
- Simone Weil, Lettre à l'ingénieur Victor Bernard -

Abstract

Topology Optimization (TO) is the process used to find the best material distribution of a design domain under given constraints. TO was used for the first time in the field of structural mechanics but it's recently applied also for electromagnetics (EMs) problems and other physics. In particular, in the field of EM, Topology Optimization can play a pivotal role in designing electric motors, induction heating devices, and components for Wireless Power Transfer (WPT) systems, for example, with the purpose of reducing the weight and cost of receiver coil in Electric Vehicles (EVs). Additive Manufacturing (AM) is becoming a feasible technology for creating industrial components by using, for instance, the UV-assisted 3D printing technique. These innovative methods offer the means to create intricate geometries that align with the outcomes of TO procedures, showing the strong connection between TO and AM. At the beginning of this thesis, a literature review of AM techniques for the design of components made by magnetic and conductive materials will be given. Then the work focuses on the development of numerical methods, by using commercial software, to perform TO in the field of EM. These techniques will be used for the realization of realistic electromagnetic devices.

Riassunto

La *Topology Optimization (TO)* è una metodologia impiegata per definire la migliore distribuzione di materiale in un dominio di progettazione nel rispetto di vincoli predefiniti. Originariamente concepita per applicazioni in ambito meccanico-strutturale, *TO* ha recentemente esteso il suo campo d'azione a differenti settori della fisica ed in particolare all'elettromagnetismo. In quest'ultimo contesto, *Topology Optimization* assume un ruolo di rilievo nella progettazione di dispositivi quali motori elettrici, sistemi di riscaldamento a induzione e componenti per il *Wireless Power Transfer (WPT)*, con l'obiettivo, per esempio, di ottimizzare peso e costi delle bobine nei veicoli elettrici. *Additive Manufacturing (AM)* sta diventando una tecnologia capace di realizzare componenti industriali utilizzando, in taluni casi, una tipologia di stampa UV-*assisted* 3D. *TO* ed *AM* consentono, fra l'altro, di progettare e realizzare componentistica efficientata a geometria complessa dimostrando la forte e proficua connessione che intercorre fra loro. Questa tesi si propone di utilizzare, integrandole, queste innovative metodiche d'indagine e di produzione. Dopo una inziale rassegna sullo stato dell'arte delle tecniche *AM* per la produzione di dispositivi e componenti realizzati con materiali magnetici e conduttivi, il lavoro si è focalizzato sullo sviluppo di metodi numerici, implementati mediante l'utilizzo di software dedicato, per eseguire la *TO* nel campo dell'EM. Queste tecniche saranno utilizzate per la realizzazione di dispositivi elettromagnetici.

Contents

List of Figures

List of Tables

List of Symbols

α	Penalization factor
$\boldsymbol{\sigma}$	Stress tensor $[Pa]$
$\boldsymbol{\varepsilon}$	Strain tensor
$\boldsymbol{u}$	Displacement $[m]$
$\mathbf{A}$	Magnetic vector potential $[Tm]$
$\mathbf{B}$	Magnetic flux density $[T]$
$\mathbf{D}$	Electric displacement $[C/m^2]$
$\mathbf{E}$	Electric field $[V/m]$
$\mathbf{f}$	External force vector $[N]$
$\mathbf{H}$	Magnetic field $[A/m]$
$\mathbf{J}$	Current density $[A/m^2]$
$\boldsymbol{C}$	Elasticity tensor $[Pa]$
$\boldsymbol{\mathcal{S}}$	Compliance tensor $[Pa^{-1}]$
μ	Magnetic permeability $[H/m]$
μ_0	Magnetic permeability of vacuum $[H/m]$
μ_r	Relative magnetic permeability
$\mu_{r,max}$	Maximum value of relative magnetic permeability
$\mu_{r,min}$	Minimum value of relative magnetic permeability
ρ	Design variable
σ	Electric conductivity in $[S/m]$
ε	Electric permittivity $[F/m]$

ε_0	Permittivity of vacuum $[F/m]$
ε_r	Relative permittivity
φ	Electrical scalar potential $[V]$
ϱ	Volume charge density $[C/m^3]$
E	Young's modulus $[Pa]$
M	Mutual inductance $[H]$
V_{frac}	Average volume factor
W_m	Total magnetic energy $[J]$
W_s	Total elastic strain energy $[J]$

List of Acronyms

AM Additive Manufacturing

AVM Adjoint Variable Method

BJ Binder Jetting

DED Direct Energy Deposition

EBM Electron Beam Melting

EM Electromagnetic

EVs Electric Vehicles

FDM Fused Deposition Modelling

FEM Finite Element Methods

GA Ground Assembly

IEMs Integral Equation Methods

MIS Material Interpolation Schemes

MMA Method of Moving Asymptotes

PBF Powder Bed Fusion

PDEs Partial differential equations

SIMP Solid Isotropic Material with Penalization

SLM Selective Laser Melting

SLS Selective Laser Sintering

TO Topology Optimization

UV Ultraviolet

VA Vehicle Assembly

WPT Wireless Power Transfer

Chapter 1

Introduction

Topology Optimization (TO), rooted in structural mechanics, is a mathematical and computational method employed in engineering and structural design to ensure the optimal material distribution within a defined space considering specific constraints and performance criteria [1]. Significant progress has been made in the field with pioneers like Martin Philip Bendsoe and Niels Olhoff in the late 1980s contributing to the development of mathematical methodologies focused on structural design and optimal topologies. In 1988, Bendsoe and Kikuchi introduced a fundamental homogenization method [2], marking a shift toward more sophisticated computational approaches. Ole Sigmund's innovative algorithms in the mid-1990s further advanced the discipline, especially in designing compliant mechanisms [3]. Since that time, Topology Optimization has grown beyond structural domains and is now utilized in fluid dynamics, heat conduction, and electromagnetics, transcending traditional boundaries. Ongoing research addresses scalability, robustness, and uncertainties, reflecting the interdisciplinary nature and dynamic evolution of the field. The main objective is to establish the most useful way of arranging the materials to achieve specific performance criteria for a structure or a device. This discipline has gained significant interest in the last decades due to its ability to redefine structural geometries innovatively and efficiently. In recent years, the integration of Topology Optimization with Additive Manufacturing (AM) has become prominent, enabling the design of intricate structures for various fields, particularly in electromagnetics. Additive Manufacturing, or 3D printing, stands as an advanced production technology enabling the creation of three-dimensional objects. Diverging from traditional manufacturing processes requiring material removal, Additive Manufacturing constructs objects layer by layer [4]. This innovative approach presents numerous benefits, unlocking opportunities across industries such as engineering, manufacturing, medicine, automotive, electronics, and aerospace. It enables the production of highly customized objects that are tailored to meet specific needs. It's particularly relevant in medical applications like personalized prostheses or implants. In comparison to traditional subtractive manufacturing, Additive Manufacturing significantly reduces material waste by building objects layer by

layer. Its on-demand production capability minimizes inventory costs and ensures a rapid response to market needs [5]. This study focuses on developing numerical methods for Topology Optimization in the field of electromagnetic (EM) devices, employing commercial software. The final step involves implementing the optimized designs using Additive Manufacturing. Leveraging the differential formulation of Maxwell's equations, the Finite Element Methods (FEM) is a well-established technique for solving electromagnetic problems. Extensively researched for various electromagnetic scenarios, FEM has also been integrated with other fields such as thermodynamics. The Finite Element Method has been extensively researched and refined for solving various electromagnetic problems, including electrostatics, magneto-statics, magneto-quasi-statics, and full-wave problems, involving all types of electromagnetic materials such as inhomogeneous, anisotropic, and non-linear media [6]. However, FEM faces challenges, including the need to discretize both active (i.e. conductive, dielectric different from the vacuum, and magnetic media) and inactive domains e.g. the air. In addition, to solve an open boundary problem with FEM, it is necessary to restrict the domain of analysis to a sufficiently large space surrounding the components and typically to introduce an artificial boundary. Alternative approaches like Integral Equation Methods (IEMs), which rely on the integral formulation of Maxwell's equations, have been considered, but they generate dense algebraic systems with quadratic complexity in terms of storage and basic arithmetic operations. Historically, Finite Element Method, available in commercial software, has been widely adopted for solving electromagnetic problems and solid-structural mechanics. It serves as a numerical technique for solving engineering and mathematical physics problems, breaking down complex problems into smaller finite elements [7]. COMSOL® Multiphysics, renowned for its comprehensive simulation capabilities, facilitates the application of FEM to solve Maxwell's equations, allowing nuanced modeling of diverse electromagnetic phenomena. The user-friendly interface enables seamless simulation setup, supporting various element types and mesh refinement for accuracy [8]. It accommodates complex material properties, constitutive models, and employs advanced solver techniques for accuracy and computational efficiency. Beyond electromagnetic problems, the software excels in facilitating multiphysics simulations, offering a unified environment for analyzing electromagnetic fields and mechanical structures. The capabilities extend to exploring electromechanical coupling, accommodating material nonlinearities, and enabling dynamic analysis for a comprehensive understanding of transient conditions. The application of static mechanics in this work, while the electromagnetic problem inherently involves variations over time and in frequency, underscores the need for advanced numerical methods and simulation tools to address the challenges posed by dynamic electromagnetic phenomena.

1.1 Mathematical Preliminaries

Over the past decade, the numerical analysis of three-dimensional eddy current problems using the Finite Element Method has been a major focus of research in computational electromagnetics. Nodal finite element techniques were among the first methods to be introduced, with vector and scalar potential functions typically used to represent the field quantities in mainstream applications. In these techniques, nodal-based functions are used to approximate both scalar and vector potentials, and a variety of formulations have been proposed, with particular emphasis on the inclusion of the Coulomb gauge on vector potentials in the governing equation [9]. Numerical robustness is guaranteed by this approach. Maxwell's equations are the starting point for electromagnetic problems. The complete set of Maxwell's equations in the frequency domain can be written as follows:

$$\text{Faraday's Law} \quad \nabla \times \mathbf{E} = -i\omega\mathbf{B} \tag{1.1}$$

where $\mathbf{E}$ in [V/m] is the electric field and $\mathbf{B}$ in [T] the magnetic flux density.

$$\text{Ampère's Law} \quad \nabla \times \mathbf{H} = \mathbf{J} + i\omega\mathbf{D} \tag{1.2}$$

where $\mathbf{H}$ in [A/m] is the magnetic field, $\mathbf{J}$ in [A/m^2] the current density and $\mathbf{D}$ in [C/m^2] the electric displacement.

$$\text{Gauss' Law} \quad \nabla \cdot \mathbf{B} = 0 \tag{1.3}$$

$$\text{Gauss' Law} \quad \nabla \cdot \mathbf{D} = \varrho \tag{1.4}$$

where ϱ in [C/m^3] is the volume charge density. Moreover, i, ω, ∇ are the imaginary unit, angular frequency, and the Nabla operator. Maxwell's equation in differential form gives local information concerning the relation between electromagnetic fields. They are valid at any point of the space in a vacuum and inside materials. Maxwell's equation can be combined to obtain other useful relations. From (1.2) is obtain:

$$\nabla \cdot \mathbf{J} = -i\omega\varrho \tag{1.5}$$

that is known as the continuity equation. In other words, if a net current flows out of an area, the charge in the area decreases.

Magnetostatics constitutes a subfield of electromagnetism that deals with static magnetic fields, such as those generated by steady electric currents or permanent magnets. The magneto-quasistatic formulation is concerned with electromagnetic problems where the magnetic fields vary relatively slowly over time compared to the characteristic time scales of the system. This occurs when the electric fields are quasi-

static, which means that they react instantaneously to changing magnetic fields. This approximation simplifies a mathematical description of a system and is often used in situations where it is possible to ignore dynamic effects. The following mathematical expressions will now introduce the magneto-quasistatic formulation:

$$\nabla \times \mathbf{E} = -i\omega\mathbf{B} \tag{1.6}$$

$$\nabla \times \mathbf{H} = \mathbf{J} \tag{1.7}$$

$$\nabla \cdot \mathbf{B} = 0 \tag{1.8}$$

$$\nabla \cdot \mathbf{D} = \varrho \tag{1.9}$$

where $i\omega\mathbf{D} = 0$ and $i\omega\varrho = 0$. In this case, the electric problem and the magnetic problem are linked but not as strongly as in the full Maxwell's equations. From $\nabla \cdot \mathbf{B} = 0$, if the domain is simply connected for surfaces it is always possible to write Eq. (1.10). Note that the magnetic version of Gauss's law implies that there are no magnetic charges. A further consequence of this law is that the magnetic flux density is solenoidal, or divergence-free. This means that the field can be written as the curl of another vector field. It is, therefore, possible to choose a magnetic vector potential $\mathbf{A}$ such that:

$$\mathbf{B} = \nabla \times \mathbf{A} \tag{1.10}$$

where $\mathbf{A}$ is a mathematical quantity that is introduced because it is useful in computations. However, it is not a physical quantity since it is not possible to directly measure it. Substituting Eq. (1.10) in Faraday's law yielding to:

$$\nabla \times (E + i\omega\mathbf{A}) = 0 \tag{1.11}$$

and using the property:

$$\nabla \times \nabla \cdot (\bullet) = 0, \tag{1.12}$$

the following expression is obtained:

$$\mathbf{E} = -i\omega\mathbf{A} - \nabla\varphi \tag{1.13}$$

where φ is the electrical scalar potential. Maxwell's equations can be completed by the following constitutive relations which locally link the electromagnetic fields depending on the characteristics of the materials:

$$\mathbf{D} = \varepsilon\mathbf{E} \tag{1.14}$$

$$\varepsilon = \varepsilon_0\varepsilon_r \tag{1.15}$$

where ε is the electric permittivity in [F/m] and ε_0, ε_r the permittivity of vacuum and

the relative permittivity respectively. The permeability links **H** to **B** as follow:

$$\mathbf{B} = \mu \mathbf{H} \tag{1.16}$$

$$\mu = \mu_0 \mu_r \tag{1.17}$$

where μ is the magnetic permeability in [H/m] and μ_0, μ_r the permeability of vacuum and relative permeability respectively. The third constitutive equation also known as Ohm's law is the following:

$$\mathbf{J} = \sigma \mathbf{E} \tag{1.18}$$

where σ is the electric conductivity in [S/m]. These laws enable a complete description of the physics of any electromagnetic problem. In COMSOL®, the Magnetic Fields physics interface is used to compute magnetic field and induced current distributions in and around coils, conductors, and magnets. In the last ten years, computational electromagnetics research has focused on numerically analyzing two/three-dimensional eddy current problems using the Finite Element Method. Vector and scalar potential functions are commonly used to characterize field quantities in mainstream applications. The Magnetic Fields interface supports stationary, frequency-domain, small-signal analysis, and time-domain modeling in both 2D and 3D. The physics interface solves Maxwell's equations using the magnetic vector potential and, optionally for coils, the scalar electric potential as dependent variables. Ampère's Law is the central node, incorporating the equation for the magnetic vector potential and offering an interface for defining constitutive relations and associated properties, such as relative permeability. The equations used in COMSOL® can be derived from the equations described above. As previously demonstrated, the following formula can be obtained:

$$\mathbf{B} = \nabla \times \mathbf{A'} \tag{1.19}$$

and substituting it in Faraday's law is possible to obtain:

$$\mathbf{E} = -i\omega \mathbf{A'} \tag{1.20}$$

where the electrical scalar potential can be neglected since there's no charge distribution. In this case:

$$\mathbf{A'} = \mathbf{A} - \int_t grad\varphi dt \tag{1.21}$$

it is so possible to understand that the function **A** is not unique [10]. The problem is that when using the scalar potentials to find a unique solution it was sufficient to impose the boundary conditions while in the case of vector potential, it is not sufficient. What is needed is to extract out of all the possible functions the specific one and this

is done by the technique called "gauging" that allows the problem to have a unique solution. The Gauge condition can be written as follows:

$$\nabla \cdot \mathbf{A'} = 0 \tag{1.22}$$

as it was already said, by doing this the unicity of the solution of the system is restored. The Ampère's Law can be written as follows:

$$\nabla \times \mathbf{H} = \mathbf{J} \tag{1.23}$$

The constitutive relation links **E** and **J** through the electric conductivity σ [S/m] as:

$$\mathbf{J} = \sigma \mathbf{E} + i\omega \mathbf{D} \tag{1.24}$$

These are the reference formulas that underpin the use of simulations carried out with the commercial software COMSOL® for the analysis of the behavior of the equipment in use under the electromagnetic profile. On the other hand, linear elasticity equations are employed to analyze the structural response of the components under the influence of mechanical loads. These equations involve stress-strain relationships, governing the deformation and mechanical behavior of components. It will now analyze mathematical preliminaries that underlie the analysis of the software COMSOL® about solid and structural mechanics of the equipment in use. Linear elasticity equations describe the relationship between stress and strain in a deformable material within the linear elastic range [11]. In the context of magneto-structural optimization, these equations are fundamental for analyzing the structural response of coil components subjected to mechanical and thermal loads. The general form of linear elasticity equations, often written in three dimensions, is given by:

$$\nabla \cdot \boldsymbol{\sigma} + \mathbf{f} = 0 \tag{1.25}$$

where $\boldsymbol{\sigma}$ is the stress tensor in [Pa] and **f** is the external force vector in [N]. The stress tensor can be related to the displacement vector ($\boldsymbol{u}$) through the constitutive relation

$$\boldsymbol{\sigma} = C\boldsymbol{\varepsilon} \tag{1.26}$$

where C is s the elasticity tensor in [Pa], and $\boldsymbol{\varepsilon}$ the strain tensor [12]. The strain tensor is related to the displacement vector through the strain-displacement relation:

$$\boldsymbol{\varepsilon} = \frac{1}{2}(\nabla \boldsymbol{u} + (\nabla \boldsymbol{u})^T) \tag{1.27}$$

where $\boldsymbol{u}$ is the displacement in [m]. Substituting this expression for $\boldsymbol{\varepsilon}$ into the consti-

tutive relation:

$$\boldsymbol{\sigma} = C\frac{1}{2}(\nabla \boldsymbol{u} + (\nabla \boldsymbol{u})^T). \tag{1.28}$$

In the context of magneto-structural optimization, it is crucial to consider material compliance, which measures the deformable response of the material under the application of stress [13]. Let's define the compliance tensor $\mathcal{S}$ as the inverse of the elasticity tensor:

$$\mathcal{S} = C^{-1} \tag{1.29}$$

Multiplying both sides of the constitutive relation by the compliance tensor:

$$\mathcal{S}\boldsymbol{\sigma} = \frac{1}{2}(\nabla \boldsymbol{u} + (\nabla \boldsymbol{u})^T), \tag{1.30}$$

compliance ($\mathcal{S}$) can be defined in terms of the stress tensor (σ) through the relation:

$$\boldsymbol{\varepsilon} = \mathcal{S}\boldsymbol{\sigma} \tag{1.31}$$

where $\boldsymbol{\varepsilon}$ is the stress vector, and $\boldsymbol{\sigma}$ represents stress tensor. The incorporation of compliance into analyses is crucial to evaluate the material's deformability under specific operating conditions and optimize the structure concerning the required magnetic and mechanical specifications. Furthermore, the total elastic strain energy (W_s) offers a comprehensive measure of the material's elastic response across its entire volume (Ω). It can be expressed as:

$$W_s = \frac{1}{2}\int_{\Omega} \boldsymbol{\sigma} : \boldsymbol{\varepsilon}\, d\Omega \tag{1.32}$$

This integral form provides a comprehensive measure of the material's elastic response throughout the entire volume (Ω). The inclusion of compliance and the consideration of elastic strain energy contribute significantly to the magneto-structural optimization analysis, offering insights into both the deformability and energy aspects of the material under varying conditions. The simultaneous consideration of Maxwell's equations and linear elasticity allows for a comprehensive analysis that addresses both electromagnetic and structural aspects.

As previously mentioned, commercial software such as COMSOL® are based on the Finite Element Method, which refers to differential formulations of Maxwell's equations. FEM is a numerical analysis technique used to obtain approximate solutions to a wide range of engineering problems [14]. A piece-wise approximation to the governing equations is provided by a finite element model. Partial differential equations (PDEs) are typically used to express the physical laws for space and time-dependent problems. In most cases, these PDEs cannot be solved analytically, so an approximation of the equations is constructed using different types of discretization methods. These

methods approximate the PDEs with numerical model equations, which can be solved using numerical methods. The numerical model equations provide an approximation of the real solution to the PDEs. To compute such approximations, the Finite Element Method is used. FEM converts differential equations into algebraic equations easily solved by computers. This method breaks down complex problems into smaller, more manageable pieces called finite elements.

The Finite Element Method involves assembling equations representing the elements into a comprehensive system that models the entire problem. To achieve this, the first step is to divide the solution region into elements, a process known as meshing. Then, nodes are assigned to each element and an interpolation function is chosen to represent the variation of the field variable over the element. Only at the nodes, which are the set of vertices of the finite elements (including the mid-side nodes), will the algorithm calculate the solution to the equation. Within the finite elements, the solution will be approximated using interpolating functions. Each function corresponds to a node in the mesh, assuming a unit value at the main node, zero at the edges of the node support, and nothing in the rest of the domain. The function inside the support can decrease linearly, quadratically, cubically, etc., depending on the desired interpolation type in the finite elements (Figure 1.1). After establishing the finite element model (i.e.,

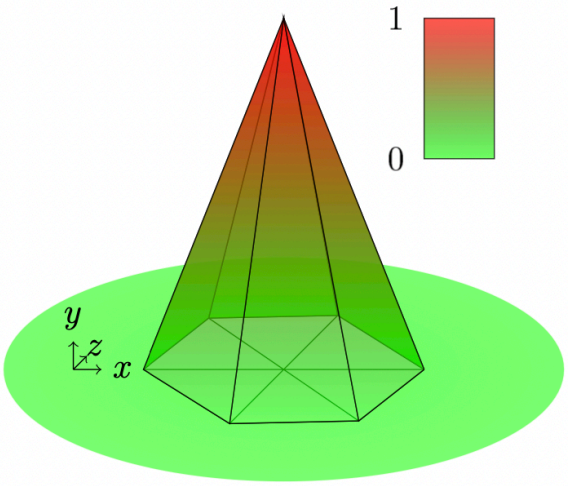

Figure 1.1. *Example of linear interpolating function.*

selecting the elements and their interpolation functions), it is possible to determine the matrix equations that express the properties of the individual elements. In the end, the algorithm's solution can be calculated by summing the various interpolating functions of form N_j, multiplied by the potential of the corresponding node U_j:

$$u_h = \sum_{j=1}^{N} N_j U_j \tag{1.33}$$

where N represents the total number of nodes. There are several methods for solving the problem of mesh node equations [6]. The variational approach is based on the calculus of variations and involves maximizing or minimizing functionals that map from a set of functions to real numbers. This method approximates a solution by minimizing an associated error function. The weighted residuals approach is based on mathematical relations. It starts with the governing equations of the problem and proceeds without reliance on a variational statement. The weighted residual approach is used to avoid finding a functional to be minimized, as it is based on the differential equations of the system. This approach is advantageous because it allows for the extension of the finite element method to problems where no functional is available. Because of its flexibility, finite element analysis is suitable for efficient and accurate solutions of problems involving partial differential equations.

1.1.1 Adjoint Variable Method

When addressing Topology Optimization constrained by partial differential equations through a gradient-based method, it is necessary to compute the sensitivity of the objective function with respect to the design variables [15]–[17]:

$$Sensitivity := \frac{dF}{d\rho} \tag{1.34}$$

In the following, a brief description of the Adjoint Variable Method (AVM) applied for sensitivity calculations is given [18]. In the discrete setting, where $\rho = \{\rho_i\}$ for $i = 1, \ldots, N$, with N the number of mesh elements, the total derivative of the objective function $F = F(u(\rho), \rho)$ is:

$$\frac{dF}{d\rho_i} = \frac{\partial F}{\partial \rho_i} + \frac{\partial F}{\partial u_j}\frac{du_j}{d\rho_i}. \tag{1.35}$$

The underlying PDE governing the physical problem can be written as:

$$\mathcal{L}(u(\rho), \rho) = 0. \tag{1.36}$$

For the kth equation, in the discrete setting, it is possible to write:

$$0 \equiv \frac{d\mathcal{L}_k}{d\rho_i} = \frac{\partial \mathcal{L}_k}{\partial \rho_i} + \frac{\partial \mathcal{L}_k}{\partial \rho_j}\frac{du_j}{d\rho_i}. \tag{1.37}$$

Multiplying the previous equation by λ_k and adding the result to (1.35) we obtain:

$$\frac{dF}{d\rho_i} = \left[\frac{\partial F}{\partial \rho_i} + \lambda_k \frac{d\mathcal{L}_k}{d\rho_i}\right] + \left[\frac{\partial F}{\partial u_j} + \lambda_k \frac{\partial \mathcal{L}_k}{\partial u_j}\right]\frac{du_j}{d\rho_i} \tag{1.38}$$

If the coefficients λ_k are chosen in such a way that:

$$\frac{\partial F}{\partial u_j} + \lambda_k \frac{\partial \mathcal{L}_k}{\partial u_j} = 0, \tag{1.39}$$

the non-trivial calculation of $du_j/d\rho_i$ terms can be avoided, thus the evaluation of the sensitivity reduces to:

$$\frac{dF}{d\rho_i} = \frac{\partial F}{\partial \rho_i} + \lambda_k \frac{d\mathcal{L}_k}{d\rho_i} \tag{1.40}$$

Application of AVM to a linear problem

Here the AVM is applied to a linear problem, whose discrete form is written as:

$$\mathbf{A}(\rho)\mathbf{u} = \mathbf{b}. \tag{1.41}$$

The problem is linear in the sense that the matrix $\mathbf{A}$ does not depend on the solution array $\mathbf{u}$ but it is only a function of the material distribution, that is, a function of design variables ρ. Equation (1.41) is the discrete form of the PDE (1.36). To apply the AVM first, the adjoint field $\boldsymbol{\lambda}$ must be obtained by solving (1.39) which, for this particular case, results in the system:

$$\mathbf{A}^\top \boldsymbol{\lambda} = -\frac{\partial F}{\partial \mathbf{u}}. \tag{1.42}$$

Next, the sensitivity is obtained through (1.40) which in this particular case is written as:

$$\frac{dF}{d\rho_i} = \frac{\partial F}{\partial \rho_i} + \boldsymbol{\lambda}^\top \frac{\partial \mathbf{A}(\rho)}{\partial \rho_i}\mathbf{u}. \tag{1.43}$$

Note that in general (1.40) also includes the derivative of $\mathbf{b}$ with respect to ρ_i, which is zero in this case since $\mathbf{b}$ is independent from ρ (see (1.41)).

Chapter 2

Additive Manufacturing

"Additive Manufacturing (AM) is the general term for those technologies that successively join material to create physical objects as specified by 3D model data. These technologies are presently used for various applications in the engineering industry as well as other areas of society, such as medicine, education, architecture, cartography, toys, and entertainment" [19]. In other words, AM is a versatile technique used to produce technical components with complex geometries. Its key advantage is waste minimization. The process involves depositing successive layers of material, each of which settles on the previous. The technology was introduced by Charles Hull in 1986, initially as stereolithography (SLA). Since then, many methods have been developed, including Powder Bed Fusion (PBF), Direct Energy Deposition (DED), Binder Jetting (BJ), Inkjet Printing, and Fused Deposition Modelling (FDM) [20], [21]. The concept of incrementally adding material during the manufacturing process to create functional tools and components is rooted in traditional craft techniques and reflects an ancient practice. However, Additive Manufacturing differs from these time-honored methods primarily in the incremental scale and spatial accuracy of the added material, typically in the range of 25-500 μm. Achieving repeatable accuracy at this scale requires fully digitized production systems, which explains the relatively short history of Additive Manufacturing. The earliest description of a modern metal printing system dates back to a 1972 patent by A. Ciraud, which outlined the concept of producing metal layers by selective melting of powders using electron, laser, or plasma beams [22]. In 1979, Housholder presented a powder laser sintering process and discussed the sequential deposition of planar layers and selective solidification of each layer [23]. However, at that time the technology was not mature enough for the prototyping of a complete printing system. Significant advances in digital computing and robotics in the 1980s and 90s laid the groundwork for AM systems. In 1998, Optomec launched the first metal Additive Manufacturing system, a printer based on Direct Energy Deposition (DED), followed a year later by a printing system based on Laser-PBF [24]. Subsequently, rapid advances were made in both the availability and versatility of metal 3D printing systems. By the mid-2010s, metal Additive Manufacturing systems began to reach the mainstream, having over-

come previous reliability and affordability challenges that had limited their use to niche commercial applications or scientific work. Between 2010 and 2020, Wohlers Associates' annual AM Trends, Prospects, and Forecasts report reports an impressive 27 percent annual growth rate for the AM industry [25]. Recent years have seen a proliferation of new applications, driven by the continued development of new materials and manufacturing processes. Originally adopted by architects and designers to produce aesthetic and functional prototypes quickly and inexpensively, 3D printing has expanded its reach [26]. Today, the system is used in various industries, from prototyping to final production. This transition addresses the challenge of product personalization, as AM enables the low-cost production of small quantities of individual parts, which is a significant departure from the traditionally high cost of bespoke product manufacture [27]. The sections below provide an overview of 3D printing techniques, focusing on the main methods used, the materials employed, their current status, and applications in different industries. Specific attention will be given to AM techniques that use metal compounds with particular reference to ferrites and copper.

2.1 Materials

The field of 3D printing covers a wide range of materials, including metals, polymers, ceramics, and concrete. Polylactic acid and acrylonitrile-butadiene-styrene are at the center of the polymer sector, particularly for 3D printing composites. The aerospace sector, seeking efficiencies over traditional processes, is turning to advanced metals and alloys, while ceramics play a key role in 3D printed scaffolds and concrete is becoming the mainstay of Additive Manufacturing for buildings [21]. Ceramics find their niche mainly in the construction of 3D printed scaffolds, while concrete plays a key role in the Additive Manufacturing of architectural structures. Materials such as titanium and its alloys, steel alloys, selected aluminum alloys, nickel alloys, and certain cobalt-based and magnesium alloys have been optimized for AM applications [27]. Titanium and its alloys, in particular, have been touted as high-performance materials with extensive applications in various industries [28], [29]. However, their adoption is fraught with inherent challenges, including increased machining costs and long lead times associated with conventional manufacturing methods. Functional materials, with particular attention to electromagnetic materials, have been explored in the field of AM. Magnetic materials, which play a key role in various applications (electronic devices, rotating electric machines, electric vehicles, etc.), have been the subject of a careful study of AM processes. Particular attention was paid to ferrites and copper. The present analysis of the AM of magnetic materials, in particular ferrites and copper, is motivated by the possibility that AM of functional materials could lead to novel magnetic components with improved performance and lower processing costs [20]. Soft Magnetic Materials, characterized by easy magnetization and demagnetization, encapsulate parameters such as low coercivity, high saturation magnetization, and

high permeability. Typical examples include iron-silicon, iron-nickel, iron-cobalt, low-carbon steel, iron, and soft ferrites [20]. Iron oxide, which is a ferromagnetic ceramic, exhibits higher electrical resistivity and lower saturation magnetization compared to conventional metallic magnetic materials, making it advantageous for applications requiring high-frequency functionality. Recent advances include the formulation of UV-curable NiZn and NiCuZn ferrite pastes tailored for 3D printing [30], [31]. Manipulation of the UV-sensitive monomer content imparts variations in cure rate, thereby influencing relative permeability [20]. Systematic changes to the composition of the magnetic paste and adjustments to the sintering temperature have enabled the production of ferrite cores with relative permeabilities of up to ~ 103 and a resonant frequency of 30 MHz [30]. Following sintering, a 3D-printed planar inductor has demonstrated an inductance of 792 nH and a resistance of 15 mΩ, closely matching the values predicted by 3D finite element analysis [20], [31]. Turning to hard magnetic materials, the appeal of Permanent Magnets goes beyond their versatile applications in computers, electric vehicles, electrical machinery, and various household appliances. Common Permanent Magnets materials include steels, ferrites, alnico, Sm-Co alloys, and Nd-Fe-B alloys [20]. In the field of electrically conductive materials, AM has received considerable attention. High-purity copper is emerging as the material of choice, with exploratory forays into aluminum (mainly $AlSi_{10}Mg$) and copper alloys (CuCrZr, CuNiSi, $Cu_{10}Zn$, CuCr, $CuSn_{0.3}$). These alternative materials offer improved printability or mechanical strength, albeit with a marginal loss in electrical conductivity [25].

2.2 AM Methods using ferrites and copper

Additive Manufacturing methodologies are classified based on various parameters, including the nature of the feedstock and the bonding mechanisms that connect successive material layers. This categorization underlines the dynamic and diverse nature of AM technologies as can be seen in the technical standards ISO/ASTM 52900:2022 mentioned above [19], [27], [32]. The integration of AM techniques with ferrite introduces new possibilities for the realization of magnetic components such as antennas, inductors, transformers and WPT components. Challenges inherent in AM, such as material purity and post-processing complexity, must be rigorously addressed to achieve the desired magnetic properties in the resulting ferrite components.

Advances in AM methodologies, particularly multi-material printing, are opening up a new frontier for the manufacture of complex ferrite structures. This capability goes beyond conventional approaches and enables the creation of multifunctional ferrite components characterized by different compositions within a single print [30]. The process of 3D printing metals typically involves melting metallic feedstock (powder or wire) using an energy source such as a laser or electron beam. The molten material transforms layer by layer to form a solid part. A 3D digital model of the object, created using computer-aided design (CAD) software, is the starting point of any process.

This digital model is then sliced into thin horizontal layers using specialized slicing software, with each layer representing a cross-section of the final object. Commonly used techniques for 3D printing metals are deep in the follow and include Powder Bed Fusion and Direct Energy Deposition, with other recently developed methods such as the Binder Jetting [21], [33]. For copper, Electron Beam Melting (EBM) [34] and Binder Jetting [33] are widely used. Pure copper components have been produced using AM processes such as Indirect Selective Laser Sintering (SLS) and Electron Beam Melting (EBM) [35], [36].

Powder-bed fusion

Powder Bed Fusion (PBF) is a key process in AM, where finely powdered materials are precisely deposited in thin layers to create intricate 3D objects. PBF involves the application of a thin layer of powder (thick metal or polymer) onto a bed, melting or sintering it layer by layer according to the CAD model data. This process is repeated until the desired object is achieved. Each layer of powder is methodically deposited and densely compacted on a platform. These layers are fused using either a laser or electron beam. Successive applications of powdered material layers are then consolidated, culminating in the formation of the final 3D component. Excess powder is then carefully removed, followed by additional processing steps such as coating, sintering, or infiltration to refine the final product [37]. Classified according to the energy source as either laser beam (Selective Laser Sintering (SLS) or Selective Laser Melting (SLM)) or electron beam (Electron Beam Melting (EBM)) processes, these methods have different applications [20]. Laser-based techniques are well suited for powders with lower melting or sintering temperatures, EBM for high-temperature metal powders. SLS proves versatile for various polymers, metals, and alloy powders, while SLM is predominantly reserved for specific metals such as steel and aluminum. In both EBM and SLM, the re-melting of the previous layer during the fusion of the subsequent layer creates a strong bond between the layers. Of note are several processing parameters, including scan speed, power, and scan strategy, which have a significant impact on the quality and integrity of the final product [20], [37]. Electron beam melting uses an electron beam as an energy source to selectively melt and fuse powdered metal materials layer by layer. Typically performed in a vacuum or low-pressure environment, EBM is well suited to various metals, particularly high-temperature alloys, making it a common choice in aerospace and medical applications. Despite its ability to produce parts with excellent mechanical properties, the need for a vacuum environment and specific material requirements contribute to the complexity and cost of EBM systems compared to some other Additive Manufacturing methods. Selective Laser Melting uses a high-powered laser beam to selectively melt and fuse powdered metal materials layer by layer. Typically performed in a controlled inert gas atmosphere (e.g. argon), SLM is a versatile technique capable of processing a wide range of metals, including stainless steel, and aluminum. Although it offers high precision and the ability to pro-

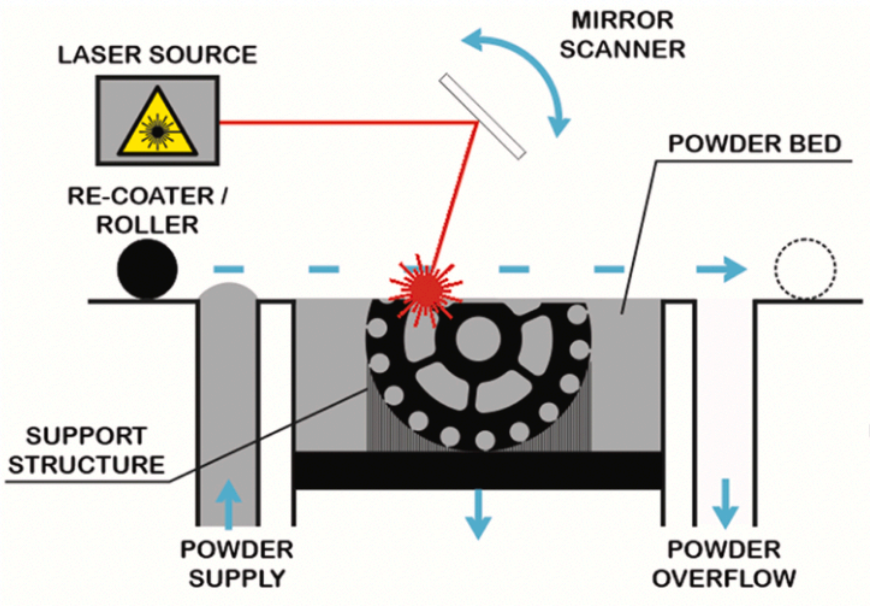

Figure 2.1. *Laser Powder Bed Fusion AM method. Image taken from [25].*

duce intricate geometries, SLM can require additional post-processing steps and the use of high-power laser systems can impact equipment costs. The choice between EBM and SLM depends on factors such as material requirements, specific application needs, and project considerations. Figure 2.1 presents a schematic representation of the SLM AM method. PBF is already widely used in a variety of industries for advanced applications, including scaffolds for tissue engineering, lattices, aerospace, and electronics. A key advantage is the use of the powder bed itself as a support, streamlining the removal of support material. However, challenges such as slow processing, increased cost, and potential problems associated with porosity when the powder is fused with a binder should be carefully considered [20], [21].

Direct energy deposition

Direct Energy Deposition (DED) is a pioneering approach known for its versatility and adaptability. Using focused energy sources, namely laser or electron beam, DED facilitates the controlled deposition of materials, making it an indispensable tool for applications ranging from component refurbishment to the creation of intricate, bespoke structures (see Figure 2.2). The taxonomy of DED techniques depends on whether the deposition head is mobile while the workpiece is stationary or, conversely, whether the deposition head is stationary while the workpiece is mobile. This feature gives DED processes a distinct advantage over Powder Bed Fusion systems, enabling them to produce voluminous structures and refurbish worn or damaged components. Moreover, DED can be combined easily with conventional subtractive processes to complete machining. Unlike PBF systems, where the powder is deposited on a substrate, DED uses inert gases to propel powders through nozzles and onto the build

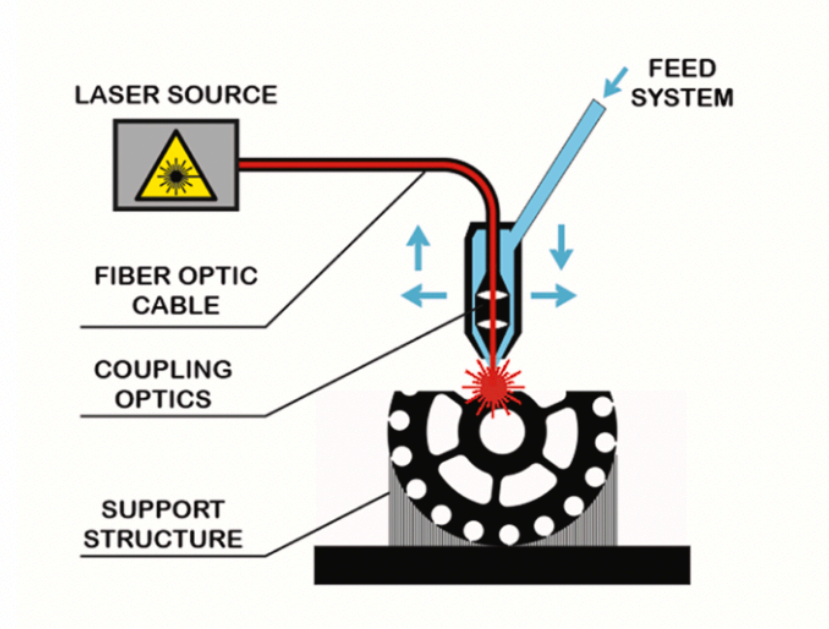

Figure 2.2. *Direct Energy Deposition AM method. Image taken from [25].*

platform. The energy source (laser or electron beam) creates a melt pool and as the powder passes through the nozzles, it is deposited onto the substrate or preceding layer. The molten material is deposited, fused into the substrate, and solidifies when it is passed through, e.g. by a laser beam [20], [38]. DED has the advantage of high build rates and large build quantities, but at the cost of reduced accuracy (0.25 mm), reduced surface quality and limited ability to produce complex parts compared to methods such as SLS and SLM [38]. As a result, DED has traditionally been used for the production of large, relatively straightforward parts and the replication of larger components. Despite its challenges, DED systematically reduces manufacturing times and costs and offers excellent mechanical properties, regulated microstructures, and meticulous composition control. This modality is finding applications in the improvement of turbine engines and various niche sectors within the automotive and aerospace industries [21]. The scalability inherent in DED facilitates the rapid printing of expansive structures, making it suitable for size-critical applications and the rapid prototyping of intricate metal components. However, DED is not without its challenges; achieving a smooth surface finish is challenging and resolution can lag behind some alternatives. The thermal energy generated during the process can affect material properties in the vicinity of the deposition. The complexity of DED processes requires careful control and post-processing steps may be essential for certain applications.

Binder Jetting

The Binder Jetting (BJ) process in Additive Manufacturing plays a key role in the production of metal components. It involves the precise inkjet deposition of a liquid binder onto a powder bed, followed by the sintering of the printed green part. This

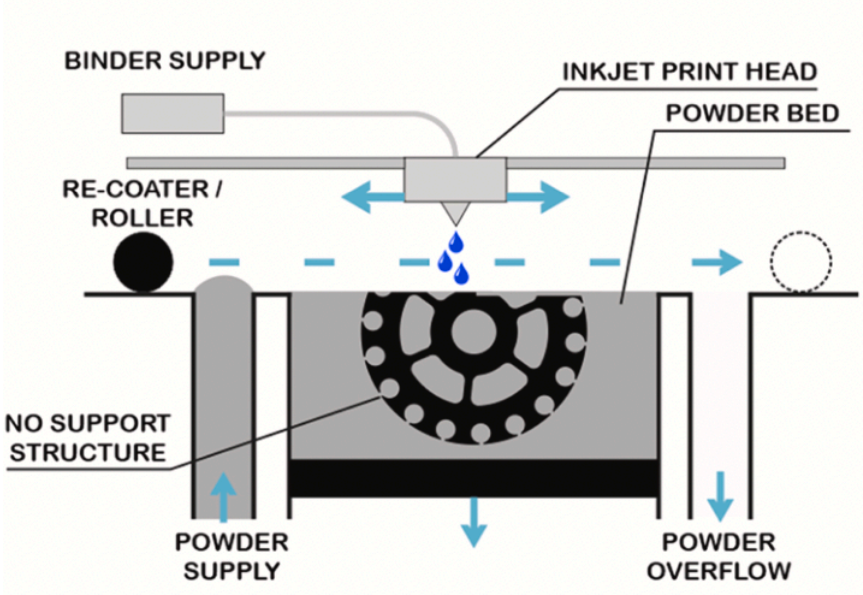

Figure 2.3. *Binder Jetting AM method. Image taken from [25].*

complex process involves the interaction of jetted binder droplets with powder particles, culminating in the formation of primitives that are intricately stitched together to form a cross-sectional layer. Each layer is meticulously printed and bonded together by the sprayed binder. The repetition of this layer-by-layer process results in the creation of the entire green part. Loose, unbound powder surrounding the part provides structural support for overhanging structures during the build phase and can be efficiently removed after printing by the application of compressed air. The depowdered green part undergoes thermal treatment, which involves the combustion of the binder and sintering of the powder particles, ultimately leading to the achievement of final density and strength [39]. See Figure 2.3 for a schematic illustration of the process. This process involves two basic materials: a powder and a binder, with the binder acting as the agent to bind the layers together. Typically, the build material is in a powdered form, while the binder is in a liquid form. Bonding of the layers is achieved by selective injection of the binder liquid, which forms the desired shape of the printed parts. Throughout the printing process, the coating head deposits alternating layers of build material and binder material as it traverses the x and y axes [20], [40]. This approach is versatile and compatible with permanent binders, low-melting metals, or sacrificial binders that can be de-bonded, ultimately achieving full density through solid-state sintering [41]. Upon completion of each layer, the printed object is lowered onto its build platform, mirroring the Powder Bed Fusion process. After the build, curing is performed to increase mechanical strength. After curing, the part typically undergoes a $24 - 36$ hours heat treatment to sinter the loose powder while removing the binder. Additional post-processing steps can significantly increase the total processing time [20]. Binder jetting is proving to be a versatile method for a wide range of

materials, including soft magnetic metal powders, ceramics, and polymers [41]–[43]. A comprehensive overview of the advantages and disadvantages is given in Table 2.1.

Table 2.1. *Advantages and disadvantages of BJ [41].*

Advantages	**Disadvantages**
Relatively difficult but large parts can be fabricated	Needs extensive postprocessing
Can print both metals and ceramics	Porosity and sacrificed carbon remains in the material that degrades magnetic property
Provides freedom of debound or injecting additional material post printing	Infiltration is required for better mechanical properties in most of the cases
Can process all kinds of powders	Tolerance maintenance is a great problem
No support structure is required	
Cheaper to fabricate parts than e-beam and SLM	

Inkjet printing

Inkjet printing, an advanced technology in the field of Additive Manufacturing, is characterized by the controlled deposition of droplets to build layer upon layer of intricate three-dimensional structures. The versatility of inkjet printing emerges from its adaptability to a wide range of materials, including polymers, metals, and ceramics, offering diverse applications across various sectors. Anyway, the use of ceramics is a distinctive aspect of inkjet printing. It is used in a variety of applications, including scaffolding for tissue engineering. It can also be used to make complex and sophisticated ceramic structures. The process involves systematically pumping a stable ceramic suspension, such as zirconia powder in water [44] through an injection nozzle and dropping it onto the substrate. These droplets collectively form a continuous pattern that solidifies to a sufficient strength to facilitate the support of successive layers of printed materials. The process is notable for its speed and efficiency, providing a versatile platform for designing and printing complex structures. Critical factors affecting the quality of inkjet printed parts include ceramic particle size distribution, ink viscosity, solids content, extrusion rate, nozzle size, and print speed [45]. However, challenges remain in maintaining processability, achieving coarse resolution, and overcoming interlayer adhesion issues, which are the primary limitations associated with this method [21]. Compared to Directed Energy Deposition and Powder Bed Fusion, inkjet printing offers advantages in material versatility and precision in creating intricate details. While DED excels in rapid production and material deposition onto existing components, and PBF provides high production speed and a wide range

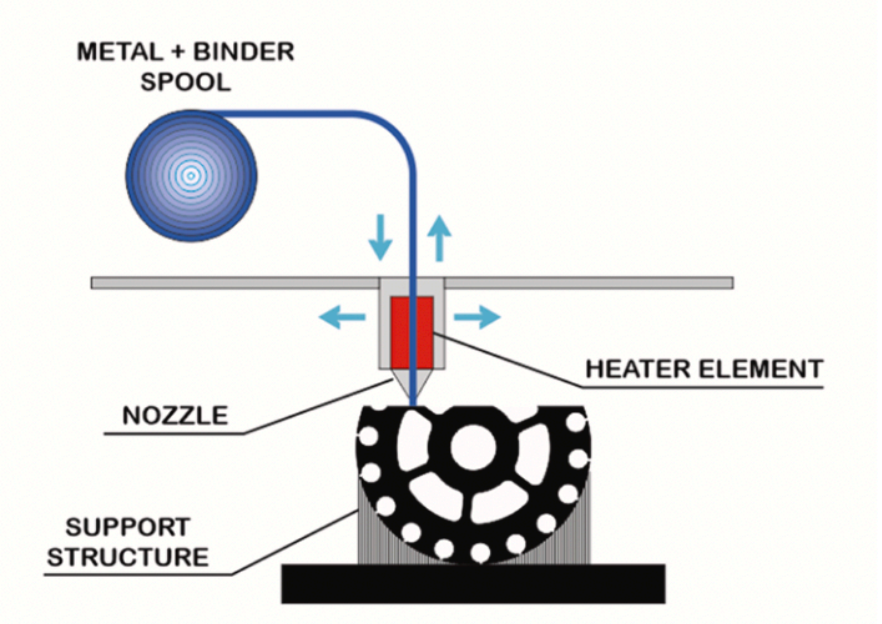

Figure 2.4. *Fused Deposition Modelling AM method. Image taken from [25].*

of materials, inkjet printing is competitive in scenarios requiring a combination of versatility and precise detailing.

Fused Deposition Modelling

Fused Deposition Modelling (FDM) uses a filament that is loaded onto a spool connected to the 3D printer to prepare the material. The printer heats the thread to its melting point and extrudes the melted substance through a nozzle. See Figure 2.4 for a visual representation of FDM process.

The printer's nozzle maneuvers in the X, Y, and Z axes, depositing the molten material layer by layer following the sliced cross-sections. Each layer integrates seamlessly with the previous one, progressively forming a solid structure. As each layer is deposited, the molten material cools and solidifies rapidly, ensuring the structural integrity of the entire object. This layer-by-layer deposition process continues until the entire object is meticulously constructed. Support structures of the same or different material can be used for overhanging or intricate features and can be removed after printing. Once 3D printing is complete, the printed object can undergo additional post-processing steps such as support structure removal, sanding, or surface finishing to achieve the desired final result. FDM is easy, cost-effective, and versatile, making it popular for applications including rapid prototyping and custom parts. Peng et al. [46] printed and characterized ferrite-based soft magnets ($NiFe_2O_4$) with unique 3D structures using an extrusion-free forming technique coupled with a high-temperature solid-state reaction process. While the printed samples exhibited commendable magnetic properties, they were susceptible to drying cracks, highlighting the need for careful control of the drying rate. FDM technology, on the other hand, operates under

relatively simpler printing conditions and can accommodate a wide range of materials, from pure polymers to metal composites that can form a fused slurry. In particular, FDM can facilitate the printing of large-volume artifacts without the strict requirements of an inert atmosphere. For the next generation of manufacturing industries, these advances in FDM printing of large parts hold great promise. Table 2.2 shows FDM's advantages and drawbacks [41].

Table 2.2. *Advantages and disadvantages of FDM [41].*

Advantages	**Disadvantages**
Can print any kind of magnetic materials	Saturation magnetization M_s is reduced because of non-magnetic polymer
Eddy current loss can be greatly reduced with high resistivity of polymers	Thermal conductivity is reduced
Low-temperature processing is useful to preserve the magnetic properties during printing	Mechanical properties are poor, especially in build direction
Improved corrosion resistance	Frequent nozzle clogging
Large parts production is possible	Limited to thermoplastic polymers
Machinery easy and safe to operate	
Multimaterial printing is possible	

In summary, powder bed fusion systems, including both electron beam (EB-PBF) and laser (L-PBF) fusion, binder jetting, directed energy deposition, and various extrusion-based techniques commonly referred to as fused deposition modeling, are the primary Additive Manufacturing methods used for ferrite and copper fabrication. Both BJ and L/EB-PBF are based on powder bed technologies in which the printed components are immersed into the powder bed layer by layer during the printing process. In L/EB-PBF, the raw powder is solidified by an energy beam, while BJ uses a binder [25]. In contrast, both DED and extrusion-based methods allow the printed part to remain stationary while the print head undergoes three-dimensional movement. In these approaches, the raw material is fed directly from the print head. In DED this is facilitated by a pressurized powder/inert gas mixture or a wire feeder, while in FDM a filament containing mixed metal particles in a thermoplastic binder is used [25]. In particular, techniques employing binders to melt raw materials, such as FDM and BJ, require additional post-printing processes. These include debinding and furnace sintering of the green part to remove binder from the part and facilitate densification of the metallic phase. To provide an overall comparative analysis, the advantages and disadvantages of each process are summarised in Table 2.3 [25].

Research into AM and in particular FDM for magnetic ferrites opens up opportunities for bespoke and rapid prototyping, offering a tailored approach to component

Table 2.3. *Comparison of common AM printing methods [25].*

AM Method	Advantages	Disadvantages
PBF	• High printed material density typically > 99% for iron alloys [47] • High spatial accuracy-printing resolution up to 15 μm (dependent on the powder and laser spot size) [48]. • Promising future multi-material printing possibilities [49].	• Low build rate: L-PBF processes are well known for their low build rate. The reported rates are anywhere between 5 (single laser 200 W) [50] to ~ $90 cm^3/h$ (manufacturer declaration-dual 1 kW lasers [51]). Most of the reported rates in the literature fall somewhere in between. • Printing systems are typically more expensive. • Requires extensive support during printing; support removal can be time-consuming and complicated.
DED	• Excellent for repair or feature addition can print directly on parts [21]. • Fast build rate: depending on the feed mechanism: 70 (powder)-700 (wire) cm^3/h [22]. • High printed material density-typically > 99% for iron alloys [52]. • Simple integration with subtractive manufacturing	• Low accuracy and surface finish-limited complexity of printed parts [21]. • Very limited maximum overhang angle [53]. • increased waste material-parts are typically printed larger and machined to net-shape.
BJ	• No printing supports-less post-processing, more design options [54] • Fast build rate some authors claim practical speeds up to 200 cm^3/min [55] are achievable. • Best for indirect production preparation of sand-casting cores and molds.	• Shrinkage typically 1520% [55], [56], depending on the density of the green part, alloy type, and sintering temperature. Unpredictable shrinkage can result in non-desired part dimensions. • Low density-obtaining 50 – 90% relative density is common for BJ sintered iron alloy sample [56], [57] in the literature; some studies describe obtaining densities above 99% [58] but with unspecified ratio of metallic to binder phase
FDM	• Most simplistic and least expensive approach to metal 3D printing [21]. • Largest extrusion-based printers (BAAM) are well known for their impressive size (in multiple meters) and build rate (50 kg/h) [59]. • Currently the most capable multi-metal printing options [60]. • Machinery can be considered the easiest and safest to operate [41].	• Shrinkage-similar to the BJ process, FDM metal parts undergo debinding and sintering post-printing. FDM parts have shown similar shrinkage: in the range of 1520% [61]–[63]. • Low relative density results range from 93−95% dense steel samples [64], [65] to insignificant metallic phase content samples [66], [67].

design. In this context, it is essential to understand how the physicochemical properties of soft magnetic ferrites can be integrated to achieve the best possible results.

Soft magnetic ferrites are low coercivity cubic spinel structures formed by alloying Ni-Zn, Mn-Zn, or Co-Zn with magnetite (Fe_3O_4) [68]. In the late 1940s, they were reported to be a promising soft magnetic material with large resistivity [69]. Their high resistivity makes ferrites very useful in high-frequency electrical components such as transformer cores and antenna toroidal cores [70]. The relative magnetic permeability can be in the range of 350 to 20.000 for Mn-Zn and an effective frequency range from 10 kHz to 10 MHz, whereas the relative permeability of Ni-Zn can be in the range of 15 to 2000 [71]. Ni-Zn ferrites can have an effective frequency range from 1 to 100 MHz [72], [73]. They hold great promise for future multi-material AM processes [41]. Table 2.4 summarizes the main ferrite used in electromagnetic applications and the

Table 2.4. *Ferrites main characteristic and AM methods.*

Ferrite	Relative permeability (μ_r)	AM Methods
MnZn	350 to 20.000	-
NiZn	15 to 2.000	FDM [74], FDM+UV [30]
NiCuZn	-	FDM+UV [31], [75]

respective AM methods. In recent studies, researchers have demonstrated compelling applications of AM that underscore its transformative potential across industries. Of particular interest is the integration of ultraviolet Ultraviolet (UV) rays into some of the AM techniques described above. This has enabled new standards to be set in the production of advanced components. The use of UV in various AM techniques has not only redefined the parameters of precision and detail but also paved the way for new materials and advanced designs. One notable study delves into ceramic paste extrusion 3D printing for fabricating ferrite inductors, aiming to minimize the size of power electronic devices. The investigation places a significant emphasis on the role of UV curing in preventing feedstock slumping, resulting in the development of a practical guideline connecting yield stress to achievable dimensions. While effective for cylindrical shapes, caution is advised for non-cylindrical designs, offering valuable insights for optimizing 3D printing parameters [75]. In a parallel endeavor, another study explores the use of paste-extrusion-based 3D printing to fabricate soft ferrite magnetic components within power electronics circuits. The formulation of a UV-sensitive low-temperature sinterable NiCuZn ferrite paste enables the successful 3D printing of a planar inductor with one-turn winding embedded in the core. This not only demonstrates the feasibility of integrating ferrite materials through 3D printing but also underscores the crucial role of UV sensitivity in achieving successful outcomes. The paste exhibit compatibility with 3D printing and showcase comparable properties to commercial magnetic cores after sintering. This research exemplifies the potential of paste-extrusion-based 3D printing to seamlessly integrate soft ferrite magnetic components, promising improved power density and efficiency [31]. These exemplary applications showcase the versatility and innovation inherent in AM methodologies. By reducing waste, enhancing efficiency, and enabling rapid prototyping, these studies

contribute valuable insights into the evolving landscape of Additive Manufacturing across diverse industries. The successful utilization of ferrite materials and the strategic incorporation of UV sensitivity highlight the dynamic capabilities of AM in advancing material science and manufacturing technologies.

AM technology has emerged also as a highly effective solution for prototyping complex radio frequency circuits, offering a versatile and rapid approach. In this context, the study delves into the application of "Electrifi", a conductive filament with the potential to replace traditional copper traces in AM. The research highlights the pivotal role of copper in radio frequency circuits and explores the transformative potential of using conductive filaments, such as "Electrifi", in place of traditional copper elements. A case in point is a 3D-printed microstrip patch antenna using fused filament fabrication. Optimized for an operating frequency of 2.56 GHz in the S-band, this antenna is designed for space-born applications, aligning seamlessly with NASA's recent interests in 3D-printed satellites, space-suits, and zero gravity experiments [76]. A detailed comparative analysis between a full-wave model and the 3D-printed prototype showcases excellent agreement, underscoring the significance of conductive filaments, particularly in copper replacement, for space-oriented applications. The developed prototype demonstrates compatibility with NASA's in-space manufacturing program, emphasizing the pivotal role of copper in this transformative application of AM technology [76].

Simultaneously, the incorporation of AM with copper, employing inventive conductive filaments, signifies a departure from conventional manufacturing paradigms. This shift accelerates production timelines and seamlessly aligns with the demands of space applications, signifying a transformative phase in space-oriented electronics. Topology Optimization emerges as a crucial strategy, enhancing conductivity, reducing waste, and trimming costs in electronic component manufacturing. In essence, this exploration encapsulates a pioneering journey into the future of electronics. The collaborative synergy between cutting-edge materials, innovative manufacturing, and strategic design choices promises to redefine the landscape of electronic innovation.

Shifting gears, another facet of AM's versatility is explored in the realm of inductive Wireless Power Transfer (WPT) systems, with a keen focus on copper elements. Metal 3D printing takes center stage, offering a novel approach to coil fabrication. The study's innovative method involves using metal AM to enhance design flexibility, reduce costs, and production time, and improve transmission efficiencyall while emphasizing the central role of copper in these power transfer systems. Finite Element Analysis guides the selection of a pentagonal cross-section, identified as the optimal compromise between 3D printer constraints, material savings, and low AC resistance, with a specific emphasis on optimizing copper usage. Experimental validations affirm the effectiveness of this approach, underscoring copper's importance and highlighting AM's ability to minimize waste material, lower costs, and enhance manufacturing efficiency [77].

The investigation into Additive Manufacturing techniques for ferrite and copper materials marks a groundbreaking stride in electronic component production. Leveraging sophisticated methods like paste extrusion and UV-sensitive formulations, AM unveils novel possibilities for customized WPT systems using ferrite.

Chapter 3

Topology Optimization

Historically, optimization referred to modifying the topology of holes in a certain domain from a material perspective to minimize a user-defined objective function. Nowadays, optimization has evolved to denote the process of identifying the best solution to a problem from among a set of possible solutions. Optimization stands as a foundational concept employed across diverse disciplines to refine and enhance systems, designs, processes, and decision-making. The main goal is to achieve the best possible outcome within given limitations, often requiring a careful balance between competing objectives. It provides a fundamental framework for improving complex systems and it is present in many academic disciplines. The objective is the maximization or minimization of a certain function, subject to specific constraints. It is important to note that optimization does not necessarily lead to a topology change of the domain from a mathematical point of view. The optimization process may involve modifying the geometry of the device by adding or removing material to create a hole or cavity. Topology Optimization is distinguished from conventional size and shape optimization methods by its unique capability to dynamically alter the structure's topology throughout the solution process. Unlike size and shape optimization, which maintains the initial design's topology, Topology Optimization facilitates a more advantageous distribution of material, rendering it an indispensable preprocessing tool for sizing and shape optimization [78].

Optimization methods fall into two primary categories: gradient-free methods and gradient-based methods, each possessing distinctive characteristics. Gradient-free methods offer flexibility as they do not necessitate knowledge of objective function derivatives, making them suitable for a diverse range of problems, even those with non-smooth or complex objective functions. However, they often incur higher computational costs, especially when employing stochastic algorithms, requiring a larger number of function evaluations to achieve optimal solutions [79]. These include Particle Swarm Optimization and evolutionary algorithms such as Differential Evolution and have been stated of the art for decades. In general, such algorithms allow for a global solution of the optimization problem, but with slow convergence rates, and

only require the evaluation of the cost function. They also have the advantage that the objective function does not have to be smooth, and they are generally noise-tolerant.

On the other hand, by using the gradient of the objective function to the design variables, gradient-based methods are known for their fast convergence. However, they are less effective in non-convex scenarios, as they are susceptible to local optima. Gradient-based optimization approaches converge to a local optimum under the guidance of the sensitivity of the objective and constraints to the design variables, which must be calculated at additional cost. In particular, the so-called adjoint method, by solving a set of adjoint equations as many times as the number of objective and constraint functions, allows these gradients to be evaluated at a cost that is almost independent of the number of design parameters. As shown in Figure 3.1, there is a minimum where the function curve bottoms out and the tangent line is flat. At this point, the value of the function is lower than its value at the nearest points. This point can be a global minimum if it is the absolute lowest point in the whole function, but more often than not there will be more than one minimum in a function. In this case, they are called local minima. In optimization, the gradient is an important tool in the search for minima. The gradient is a vector that points to the steepest slope of the function at a given point.

The gradient is zero at a function's minimum point. Gradient-based optimization algorithms will continue to iterate until the gradient is very close to zero, indicating that the algorithm has reached a minimum. Typically, if we define ρ as the design variable of the optimization problem and as a function of the space associated with each mesh element, the gradient of the objective function is calculated from an initial value of ρ, namely ρ_0. In the direction indicated by the gradient, another value of ρ will be obtained to minimize the function. This process is repeated until convergence is reached. As shown in Figure 3.1, the selection of the starting point ρ_0 is fundamental, as

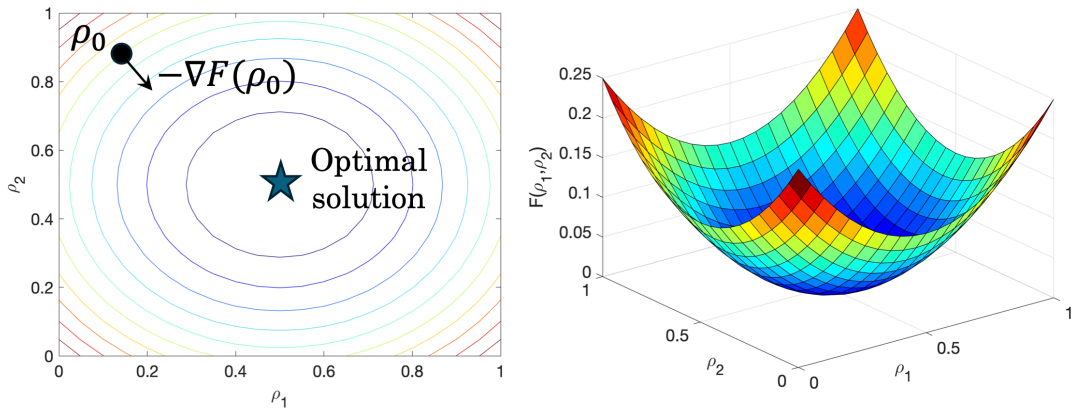

Figure 3.1. *Graphical illustration of gradient-based optimization. The minimization is retrieved by following the direction of the gradient in the parameter space, starting from an initial guess* ρ_0.

by changing it, if the objective function has many minima, different final configurations

can be obtained. This can be seen as an example in Figure 3.2, where the figure on the left shows the configuration obtained by choosing as initial value $\rho_0 = 1$ instead of the one on the right with $\rho_0 = 0.1$. The two final configurations are different, meaning

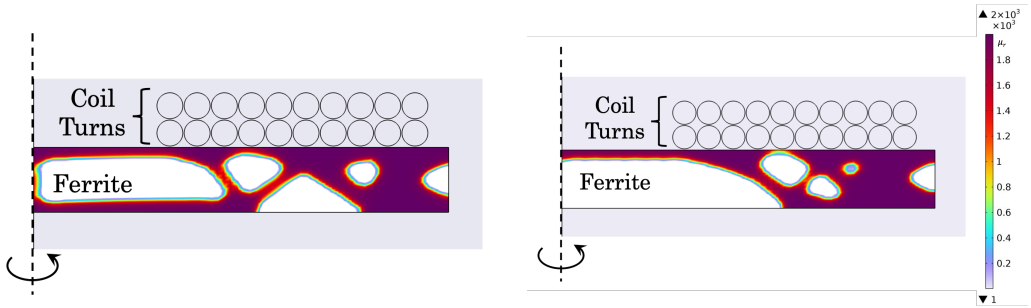

(a) Final solution initialized with ρ_0=1. **(b)** Final solution initialized with ρ_0=0.1.

Figure 3.2. *Final optimized solutions initialized whit* $\rho_0 = 1$ *(a) and* $\rho_0 = 0.1$ *(b).*

that different local minima are reached in the two simulations. In particular, denoting $\rho(x)$ as the material distribution at each point of the design domain $D \subset \mathbb{R}^d$, the mathematical formulation of the optimization problem can be expressed as follows:

$$\text{find } F^* = \min_{\rho} F(u(\rho), \rho) \tag{3.1}$$

$$\text{under given constraints}$$

where F represents the objective function and the problem constraints can be of both equality and inequality types. The objective function is dependent on the solution $u(\rho)$ of an electromagnetic problem, where u is the solution of a PDE. The optimization problem in Equation (3.1) is PDE-constrained, meaning that at least one of the constraints is expressed as a Partial Differential Equation. The governing PDE for the physical problem can be expressed as follows:

$$\mathcal{L}(u(\rho), \rho) = 0 \tag{3.2}$$

where ρ is the material distribution. This elucidates the optimization challenge as an intricate interplay between achieving the optimal material distribution and fulfilling the constraints imposed by the governing PDE.

The fundamental engineering question of how to distribute material within a given design domain to achieve optimum structural performance is solved by Topology Optimization [80]. Fig. 3.3 depicts a sketch of an MBB beam to show how to distribute material by using 1/2 of the material. Topology Optimization is the process used to find the best material distribution of a design domain. TO is nowadays used not only for mechanical but also for electromagnetics equipment [79], [82]–[91]. Designing electromagnetic devices is a complex task as they must meet requirements for compactness, high performance, efficiency, and low cost. Two approaches to solving design problems exist: empirical and methodological. The former is empirical, while the latter

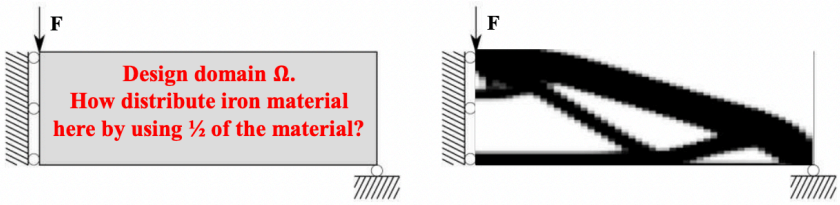

Figure 3.3. *Sketch of MBB beam with loads and constraints [81].*

uses finite element analysis approximation and numerical optimization models and algorithms. Topology Optimization aligns with the latter approach [92]. It involves determining the connectivity, shape, and location of voids within a given design domain. The design significantly impacts the performance of the final devices [93]. Topology Optimization often produces structures with complex and irregular geometries, which can be difficult to manufacture using conventional methods. However, recent advances in Additive Manufacturing and 3D printing have helped to overcome these limitations, making it possible to create intricate structures [31], [79], [94]. As in solid mechanics topology optimization, also in the field of electromagnetic problems an additional optimization problem Equation (3.1) can include a supplementary volume inequality constraint as:

$$G(\rho) = \int_D \rho(x)\, dx - V_{trg} \leq 0 \tag{3.3}$$

where V_{trg} is the desired maximal volume of the device. To solve the problem in Equation (3.1) it is essential to numerically solve the Partial Differential Equation that governs the underlying physics of the objective function. When using volume discretization techniques, this requires discretizing (i.e. meshing) the computational domain $D \subset \mathbb{R}^d$ into N_e elements, usually triangles or quadrilaterals in two dimensions ($d = 2$) and tetrahedral or hexahedral in three dimensions ($d = 3$). Each mesh element is assigned a material property and the PDE is then transformed into a system of equations using well-established methods such as Finite Element Method.

Recently, also Integral Equation Methods [95]–[97] have been applied to solve the electromagnetic problem for the Topology Optimization of devices involving open boundary problems, such as antennas [98] and Wireless Power Transfer systems [99].

In Topology Optimization problems, the design variable related to the ith mesh element $\rho_i \in \mathbb{S}$, with $i = 1, \ldots, N_e$, defines the elemental material property g with the map:

$$\mathbb{S} \to \mathbb{R} \tag{3.4}$$

$$\rho \to g(\rho) \tag{3.5}$$

A first distinction between TO approaches concerns the space $\mathbb{S}$ where the design variable ρ_i is defined, that can be continuous or binary, i.e., [80]:

$$if \begin{cases} 0 \leq \rho_i \leq 1 & \rightarrow \text{continuous TO} \\ \rho_i = \{0, 1\} & \rightarrow \text{binary TO} \end{cases}, \tag{3.6}$$

where the discrete problem, also termed ON/OFF method [100], is the most common approach for Topology Optimization. When the design variable is in the continuous space, the intermediate values (0,1) are represented as "gray scales", which do not have a clear material specification [79]. Continuous TO has the advantage of allowing for the definition of derivatives. As a result, sensitivity analysis results hold and first-order optimization algorithms can be used, which are more efficient, especially when dealing with large problems. In contrast, the drawbacks aim to guarantee that the solutions obtained are manufacturable (with ρ values of 0 or 1). For instance, if a solution has any components with ρ values between 0 and 1, then it is not manufacturable [15]. The use of continuous density design variables enables the application of efficient gradient-based optimization algorithms, which ensures convergence within a reasonable number of iterations. For the analysis of this work, only the continuous TO will be considered as explained in the following section. In the field of gradient-based methods different approaches exist, among them, the density method is the one analyzed and used in this work.

3.1 Density Method

To obtain a well-posed problem that can be effectively solved by a local continuous optimization algorithm, a common approach involves following several steps. The first step is continuous relaxation, which uses methods based on homogenization theory, density, and sensitivity filtering. The next step is to apply penalization techniques. This approach may additionally introduce supplementary constraints into the design problem, such as constraints on total material volume or the perimeter of the design domain. It is important to note that these approaches can make managing the reformulated optimal design process difficult and may even result in practical infeasibility [92]. The density method was originally developed for Topology Optimization in solid mechanics. Recently, it has garnered noteworthy attention in the realm of electromagnetic Topology Optimization, particularly for multi-material scenarios, owing to its straightforward approach [101]–[103]. Density methods employed in these contexts often rely on interpolation, filtering, and projection schemes. An objective function, a set of constraints (which may include a material usage constraint), and a discretized representation of the physical system are typically included in the mathematical formulation of a density-based Topology Optimization problem. Density-based methods are used to optimize the distribution of solid material and voids within a fixed domain

of finite elements. The primary objective is to minimize the objective function, which is achieved by determining the material type for each element. In structural Topology Optimization, compliance is frequently the primary objective, with constraints governing the permissible amount of material usage. The density method is applied to a discretized domain to determine the material type for each element and minimize the objective function. The design variables should be continuous instead of discrete, and an interpolation function can be used to interpret these variables as the material density of each element. Subsequent application of penalty methods guides the solution towards desirable "0/1," "black/white," or "solid/void" topologies. The density method can be implemented using commercial software tools. Figure 3.4 presents a flowchart outlining the necessary operational steps [79], [93]. The initial steps in-

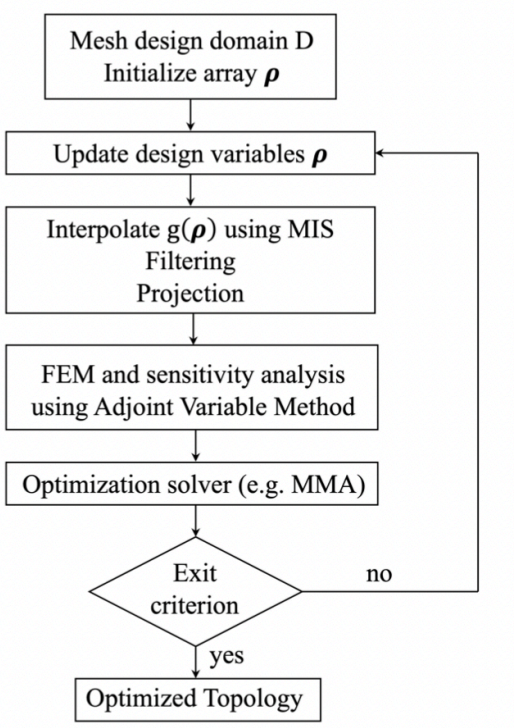

Figure 3.4. *Possible flowchart of TO using density method. The exit criterion groups convergence of objective function and fulfillment of additional constraints, for example, volume ones [79].*

volve meshing the design domain and initializing the design variables ρ. Through the Material Interpolation Schemes (MIS), these design variables are then mapped to their corresponding material properties. The original density method employed a simple power-law material penalization, resulting in what is known as the Solid Isotropic Material with Penalization (SIMP) approach. From a numerical point of view, the choice of an appropriate MIS for penalizing properties is crucial. Within the framework of density methods, an erroneous selection of the material penalization function can give rise to numerical challenges, such as singularities in the system matrices attributable

to inadequate coefficient scaling. Subsequently, by solving the equality constraints with the Finite Element Method, the state variables needed to evaluate the objective function are found. To update ρ for the next iteration, the sensitivity of the problem is required. This sensitivity corresponds to the gradient of the objective and constraint functions concerning the design variables. The Adjoint Variable Method (AVM), ex explained in 1.1.1, is implemented to calculate these sensitivities. An optimization method, such as the Method of Moving Asymptotes (MMA) [104], is used to approximate the problem convexly by internal iterations, allowing us to locally update the design variables for the next global iteration. This iterative process continues until convergence is achieved, marked by a negligible change in the objective function between two iterations or upon reaching the maximum prescribed iterations. It can also require post-processing to analyze the data [101]. Figure 3.4, highlights a pivotal step in the density method involving interpolation, filtering, and projection, each of which will be explained in the following sections.

3.1.1 Interpolation

The MIS used to assign material properties to individual elements are explained in this section. Starting from the discretization of the design domain D, a continuous variable ρ, where $0 \leq \rho \leq 1$, is assigned to each mesh cell. In the context of a two-material scenario, mesh cells characterized by $\rho = 1$ are populated with material property 1 (p_{mat1}), while material property 2 (p_{mat2}) is assigned to cells where $\rho = 0$. When ρ takes values between 0 and 1, the cell is partially occupied by the material, resulting in a condition called a "gray scale". It is generally advisable to avoid such partial occupancy situations since, in most applications, partially occupying a cell with the desired material is not feasible, unless the material density can also be controlled which is not common in most applications [79]. The density method was originally developed utilizing a simple power law as material penalization, leading to the Solid Isotropic Material with Penalization approach [92]:

$$g(\rho) = p_{mat1} + (p_{mat2} - p_{mat1})\rho^{\alpha} \tag{3.7}$$

where g(x) is the material property at the point $x \in D$, property $g(0) = p_{mat1}$, $g(1) = p_{mat2}$ and α a penalization parameter. Due to the continuous nature of $\rho(x)$, the optimization process may give rise to regions characterized by "gray scales," signifying layouts that are impractical for manufacturing. As discussed earlier, whether or not to introduce material into these gray regions must be decided during the physical realization of the device. Increasing the value of α serves to refine the optimization process by minimizing the generation of these problematic "gray scale" regions. This entails a broader assignment of material property 1 over a broader range of ρ values with material property 2 allocated primarily only when $\rho(x)$ approaches one. However, it's essential to note that excessively high values of α can cause convergence

issues as depicted in Figure 3.5 illustrating the variation of $g(\rho)$ for different α values. Consequently, a delicate balance is required, striking a trade-off between a rapid con-

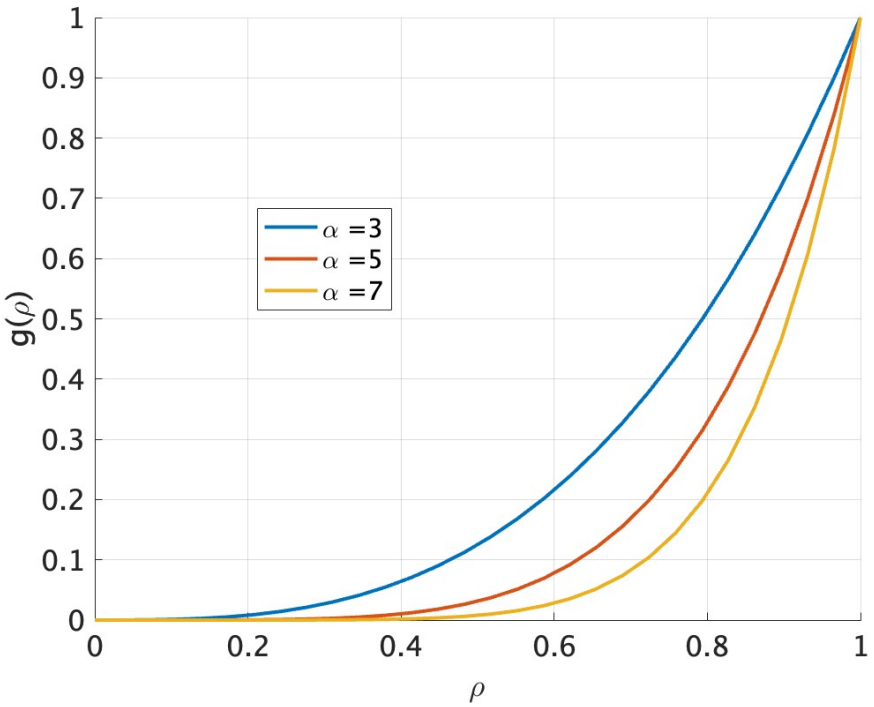

Figure 3.5. *Material proprerty as function of ρ for different values of α.*

vergence facilitated by a pronounced increase in the penalty term (potentially leading to suboptimal local outcomes) and a more gradual increase that yields better overall performance but extends computation time significantly [101].

3.1.2 Filtering

The use of ρ as direct input for the Material Interpolation Scheme may result in oscillations in the material distribution across the finite element discretization, as observed in [105]. Therefore, the adoption of spatial filtering becomes necessary. Specifically, the Helmholtz filter can be used [106], [107]:

$$-R_h^2 \Delta\tilde{\rho} + \tilde{\rho} = \rho \tag{3.8}$$

where R_h is a filtering parameter and $\tilde{\rho}$ filtered design variables.

3.1.3 Projection

The projected variables, denotes as $\hat{\rho}$ are derived from the filtered design variables $\tilde{\rho}$ using a smoothed Heaviside function:

$$\hat{\rho} = H_\eta(\tilde{\rho}) = \frac{\tanh(\beta\eta) + \tanh(\beta(\tilde{\rho} - \eta))}{\tanh(\beta\eta) + \tanh(\beta(1 - \eta))} \tag{3.9}$$

where β controls the sharpness of the projection and η is a threshold level. In summary, the design variables ρ in the continuous setting, before being used as input of MIS are firstly filtered and projected.

3.2 Numerical Tests

To evaluate the effect of filtering and projection an illustrative example is analyzed across various values of parameters α. The study focuses on a coil with a square cross-section, which has been simulated using the commercial software COMSOL® and in 2D axisymmetric mode. Topology Optimization has been applied to the ferrite material surrounding the coil. The material property $g(x)$ represents the relative permeability μ_r. Figure 3.6 provides a visual representation where both projection and filtering are considered, and the analysis is conducted for α values of 3,5 and 7 respectively. The scale legend in Figure 3.6 indicates the value of ρ ranging from 0 to 1. Figure 3.6 shows that the color of the red zone is more homogeneous in $\alpha = 7$ to the lower value of α. Therefore, increasing α helps the optimization process in mitigating the generation of "gray scale" but at the same time achieving convergence may become more challenging at higher α values. A higher penalization factor (larger α) tends to produce designs with more uniform material distribution, as the optimizer reduces the total amount of material in the design space. Conversely, a lower penalization factor allows for more heterogeneous material distributions. A well-tuned penalization factor can lead to faster and more stable convergence, while an inappropriate choice may result in slow convergence or convergence to suboptimal solutions. Adjusting the penalization factor involves finding a trade-off between achieving optimal performance (e.g., efficient power transfer), controlling the amount of material used in the design, and achieving convergence easily.

To deeply understand the effect of the Helmholtz filter a further simulation has been performed for $\alpha = 3$ with and without the filtering applied. The results are shown in Figure 3.7 The filtering process enhances the attainment of smoother and more regular solutions by mitigating oscillations and irregularities in the material distribution. This improvement significantly contributes to the overall stability of the solution. Without the filter, the red area surrounding the coil is not homogeneous. This depends on the mesh utilized but it also clearly underlines the pivotal role of the filter in achieving a more uniform distribution. Conversely, the external limit/border

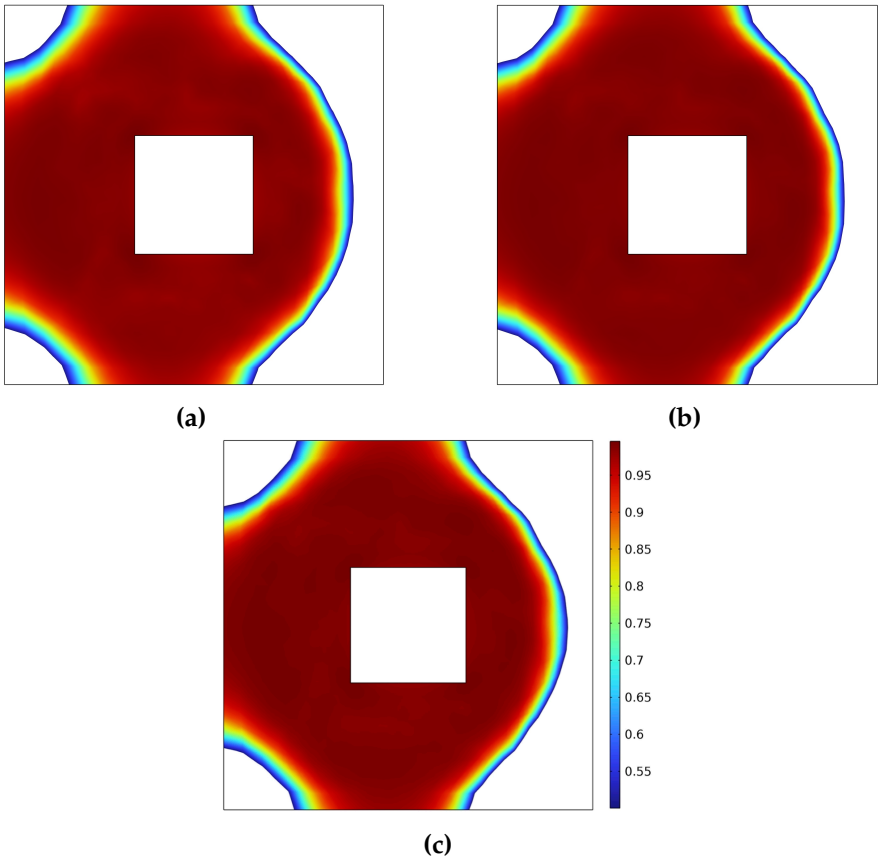

Figure 3.6. *Material distribution during the optimization produced by different values of the penalization parameter:* $\alpha = 3$ *(a),* $\alpha = 5$ *(b), and* $\alpha = 7$ *(c). The color bar refers to the value of* μ_r *for the regions with* $\rho > 0.5$*. Parts with* $\rho < 0.5$ *are not shown.*

of the final geometry appears less well-defined in the configuration with the filtering making the distinction among materials more challenging. This is because a steep change can lead to numerical instability. In summary, Helmholtz filtering plays a crucial role in Topology Optimization by providing a regularization mechanism that improves the numerical stability, convergence, and realism of the optimized designs. It is a technique used to ensure that the obtained material distributions are physically plausible and suitable for manufacturing.

In the realm of these simulations, a foundational aspect lies in the utilization of the Magnetic Fields COMSOL® physics interface. This specialized approach allows us to delve into the intricacies of magnetic interactions and their effects. However, in the case of more complex geometry, recognizing the inherent interplay between magnetic fields and structural components arises a need for a more holistic perspective. The integration of solid mechanics into simulations becomes crucial, offering a comprehensive understanding of how structural elements respond to magnetic forces.

The method proposed for improving the interconnection of structural elements entails integrating both magnetic and structural aspects. This holistic approach, though promising in its potential benefits, mandates the numerical resolution of intricate struc-

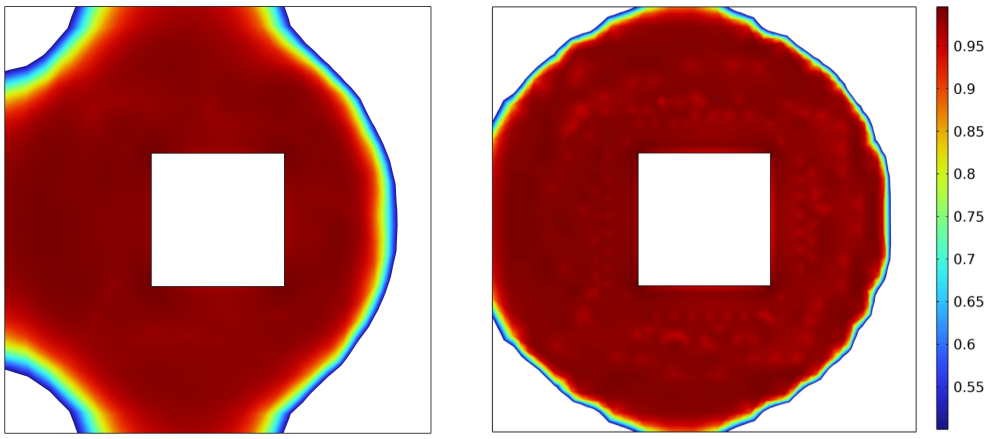

(a) **(b)**

Figure 3.7. *Material distribution during optimization produced by using* $\alpha = 3$ *with Helmholtz filter (a) and without Helmholtz filter (b). The color bar refers to the value of* μ_r *for the regions with* $\rho > 0.5$*. Parts with* $\rho < 0.5$ *are not shown.*

tural dynamics. The computational cost escalates as this inclusive analysis demands advanced simulations to precisely capture and comprehend the interplay between magnetic and structural behaviors.

In the pursuit of achieving optimal structural connectivity, especially through topology optimization, it is recognized that using only the magnetic field interface may encounter challenges such as producing disconnected geometries. To address these complexities and ensure a more realistic representation of the final geometry, it's used the Solid Mechanics physics interface present on COMSOL® Multiphysics. The incorporation of solid mechanics provides a valuable layer of understanding, allowing us to navigate through potential issues like checkered solutions and non-connected geometries.

Therefore, it's interesting to investigate a simulation framework that utilizes both Magnetic Field physics and Solid Mechanics within COMSOL®. This combined approach enables a comprehensive exploration of the intricate relationship between magnetic and structural dynamics, ensuring a more accurate representation of the system's response.

Chapter 4

Numerical Experiments

Wireless Power Transfer is a technology that allows electrical energy to be transferred without a physical connection. It is used in a wide range of applications including electric vehicles [108], [109], medical devices [110], aerospace technologies [111], cell phone charging [112], road infrastructures [113], and Internet of Things [114], [115]. WPT demonstrates its versatility and potential impact across industries and technology frontiers by enabling wireless charging, improving convenience, and overcoming the challenges associated with wired connections. At its core, WPT harnesses the fundamental principle of utilizing electromagnetic fields for the wireless conveyance of power. This intricate process relies on two essential components: the transmitting coil and the receiving coil. The source of the electromagnetic field is the transmitting coil. It generates a magnetic field around it when it is subjected to an alternating current. According to the principles of electromagnetic induction, the dynamic nature of this magnetic field induces an Electromotive Force in the adjacent receiver coil [116]. The receiving coil is strategically positioned within the effective range of the transmitting coil's magnetic field to capture the induced Electromotive Force. Electromagnetic (EM) induction in the receiving coil generates an alternating current, which can be converted into electrical energy for various applications. The receiving coil is a focal point for scientific exploration. Researchers aim to enhance its efficiency, optimize power transfer, and address safety considerations. Ongoing advancements in the design and characteristics of the receiving coil significantly contribute to the overall efficacy and applicability of WPT systems. This scientific investigation explores the complexities of electromagnetic phenomena and coil configurations, driving advancements in modern technology [117]. This work focuses on the optimization of the receiving coil, specifically within the framework of Topology Optimization applied to the ferrite material on the vehicle assembly side of a Wireless Power Transfer system. It has led to interesting progress in optimizing a power transmitter and WPT. This investigation leverages the capabilities of the commercial software COMSOL®. The analytical exploration will encompass presentations of results from both 2D axisymmetric simulations and 3D simulations analyses, each executed utilizing the magnetic field physics interface

within the COMSOL® platform. Additionally, a simulation that integrates both the magnetic field and solid mechanics interfaces will be conducted for the power transmitter device, offering a comprehensive understanding of the electromagnetic and structural interactions governing the WPT system. In section 4.1 the optimization on the power transmitter is analyzed by comparing, in particular, the configuration obtained for two initial values of ρ, 1 and 0. Then in section 4.2 a 2D axisymmetric configuration of a WPT is considered and finally in section 4.3 the 3D WPT device with massive coil first and then coil with turns. The aforementioned analytical exploration establishes the basic framework for an in-depth investigation of a power transmitter device and Wireless Power Transfer systems, in which a spectrum of simulations is performed to delineate the electromagnetic and structural intricacies that dictate device behavior. As this investigation progresses, the primary equations pivotal to our analysis are delineated below. When dealing with the mutual coupling of the coil the mutual inductance M is evaluated as follows:

$$M = \frac{\oint_C \mathbf{A} \cdot d\mathbf{l}}{I} \tag{4.1}$$

where M represents the mutual inductance between transmitter and receiver coils, $\mathbf{A}$ is the magnetic vector potential, and I is the current flowing through the coils. C represents the closed path along which the line integral of the magnetic vector potential is calculated. This formula serves as the cornerstone for evaluating the electromagnetic interactions within the WPT system. In the subsequent sections, the implications and applications of this formula will be explored in detail through analytical and computational analyses. The coupling factor is indicated as follows:

$$k = \frac{M}{\sqrt{L_t L_r}} \tag{4.2}$$

where L_t and L_r are respectively the self-inductance of the transmitter coil and the self-inductance of the receiver coil. The coupling values must be kept between determined values to avoid problems like a bifurcation. The self-inductances of the transmitter and receiver coils can be easily calculated starting from the expression of the total magnetic energy W_m:

$$W_m = \frac{1}{2} \int_\Omega \mathbf{A}^* \cdot \mathbf{J} \, d\Omega \tag{4.3}$$

where * is the complex-conjugate operator, and Ω is the space in which the WPT device lays. The self-inductance can therefore be calculated as:

$$L = 2\frac{W_m}{I^2} \tag{4.4}$$

where I is the supplied current of the coil.Simulations have been performed in COMSOL®. For the Magnetic Field physic interface, the interpolation function needed in the Topology Optimization analysis is related to the relative permeability and defined as:

$$\mu_r = \mu_{r,min} + (\mu_{r,max} - \mu_{r,min})\rho^{\alpha} \tag{4.5}$$

where $\mu_{r,min}$ is the minimum value for the relative permeability that is set equal to 1, and $\mu_{r,max}$ is the maximum value of relative permeability that can be assigned to each element of the design domain. By varying $\mu_{r,max}$ Topology Optimization will lead to different final configurations of the optimized domain.

4.1 Magneto-Structural Optimization

Magneto-structural Topology Optimization involves the simultaneous consideration of Maxwell's equations and linear elasticity [118]. Maxwell's equations describe electromagnetic behavior, while linear elasticity equations govern the structural mechanics of the components. The main equations that will be used in the following analysis have already been presented in Chapter 1 in Section 1.1. This optimization considers both magnetic and structural aspects, employing Finite Element Analysis to model magnetic fields and structural responses. Linear elasticity equations are employed to analyze the structural response of the coils under the influence of mechanical loads. The choice of linear elasticity equations is justified by their ability to provide accurate predictions of the mechanical behavior of materials under various conditions. The simultaneous consideration of Maxwell's equations and linear elasticity allows for a comprehensive analysis that addresses both electromagnetic and structural aspects. The incorporation of both the magnetic field physics interface and the solid mechanics physics interface will increase the computational cost of the simulation. In this section, a power transmitter device is examined. The shape of the coil is inspired by that of the Qi wireless power standard, whose detailed geometrical features can be found in [119]. The Primary Coil is of the wire-wound type and consists of litz wire having 30 strands of 0.1 mm diameter or equivalent. The Primary Coil has a circular shape and consists of two layers. Both layers are stacked with the same polarity. Shielding protects the Power Transmitter Product from the magnetic field that is generated in the Primary Coil. The Shielding should be Ni-Zn or Mn-Zn ferrite and should be at least 0.2 mm thick. The Shielding extends to at least 2 mm beyond the outer diameter of the Primary Coil and is placed below the Primary Coil at a distance of at most 0.1 mm. The operating frequency is 140 kHz. The main geometry dimensions are presented in Figure 4.1. The Topology Optimization is applied to the ferrite below the coils. The starting point of TO is the definition of the objective function and the constraints:

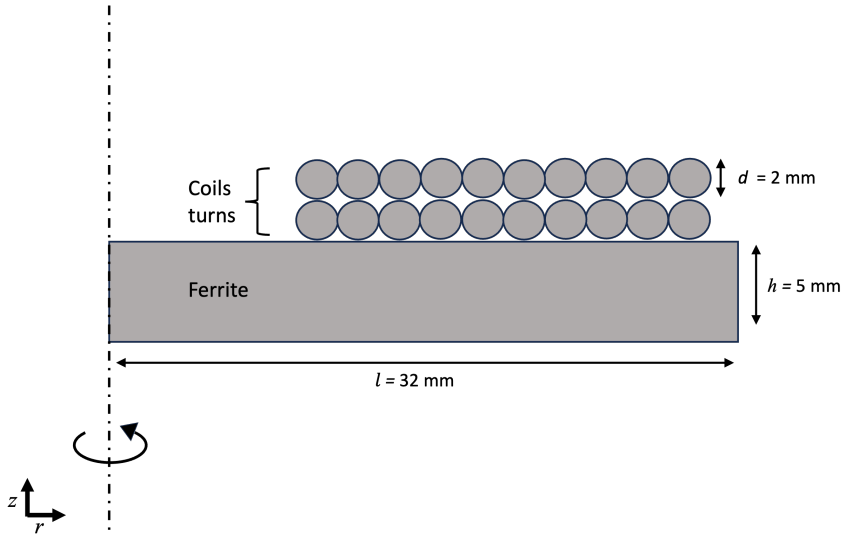

Figure 4.1. *Main geometrical dimensions of power transmitter device.*

$$\min W_s \tag{4.6}$$

$$V/V_d \leq 0.7 \tag{4.7}$$

$$W_m \geq 0.7 W_{max} \tag{4.8}$$

where W_s is the total elastic strain energy and V_d the whole volume of the design domain. W_m is the total magnetic energy and $W_{max} = 5.12$ J. The total elastic strain energy is calculated as in Equation (1.32) while the maximum value of the total magnetic energy has been evaluated directly on COMSOL® considering the ferrite completely filled with material using Equation (4.3). Then interpolation, filtering, and projection are considered. The filter type is Helmholtz while hyperbolic tangent projection is selected with a projection slope (β) equal to 8 and a projection point of 0.5. Two interpolation functions are considered, one for each physics selected. For the Magnetic Field physic interface, the interpolation function is related to the relative permeability and defined as in Eq. (4.5). On Solid Mechanics physic interface the interpolation function is instead related to the Young's modulus. The final formula can be written as follows:

$$E = E_{min} + (E_{max} - E_{min})\rho^{\alpha} \tag{4.9}$$

where E [Pa] is the Young's modulus, E_{min} and E_{max} respectively $2 \cdot 10^{-5}$ [N/m^2], and $2 \cdot 10^{11}$ [Pa]. α is the penalization factor set in $\alpha = 6$.

Simulations are performed for two different starting points of the design variable ρ.

As can be seen in Figure 4.2 the simulation has been performed in 2D axisymmetric

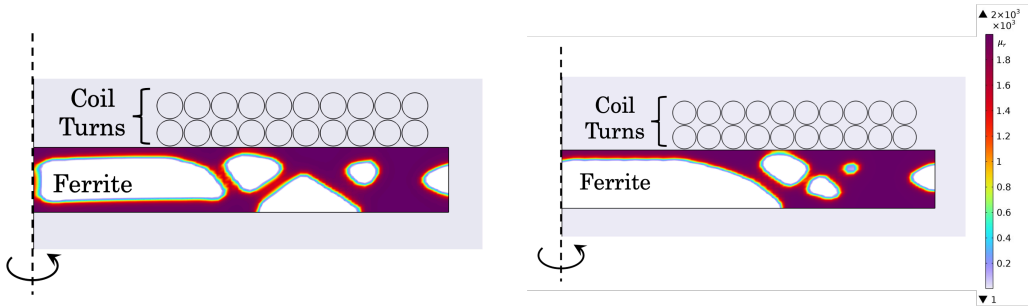

(a) Final solution initialized with ρ_0=1. **(b)** Final solution initialized with ρ_0=0.1.

Figure 4.2. *Comparison of TO of the ferrite initialized for different values of* ρ_0.

mode. The results indicated how, by starting from different values of ρ, the solutions can be very different. This, as already mentioned in Chapter 3, is related to the gradient-based method used on Topology Optimization in COMSOL®. The gradient-based method strictly depends on the initial value and by changing it, diverse local minimums can be reached meaning different final configurations of the ferrite optimized. In these simulations, both the Helmholtz filter and projection are considered.

4.2 Axisymmetric WPT device

In this section, 2D axisymmetric WPT has been simulated in COMSOL® multi-physics. The geometrical features are taken from that indicated in SAE standard [120] for WPT3/Z3. The length of the Ground Assembly (GA) ferrite is l_{GA} = 650 mm while the height is h = 5 mm. The ferrite on the Vehicle Assembly (VA) side has a length of l_{VA} = 400 mm and the same height as the transmitter's ferrite. There are 8 coils on VA while on the GA there are 16 coils but in the simulation will be considered 8 equivalent inductors. The diameter of the coil is d = 5 mm. The current supplied on GA coils is I = 1 A. A schematic representation of the main geometry dimensions is shown in Figure 4.3.

The optimization is performed on the ferrite on the VA side and simulations with massive under ferrite and inside ferrite are done. The objective function and constraints are:

$$\max M \tag{4.10}$$

$$V/V_d \leq 0.7 \tag{4.11}$$

where M denotes the mutual inductance calculated as in Equation (4.1) and V_d is the whole volume of the design domain. Topology Optimization, as already said in Chapter 3, required interpolation function. Since the physics used is Magnetic Fields, the material property is the relative permeability (μ_r), and the linear interpolation function is the same as Eq. (4.5). Simulations have been performed for

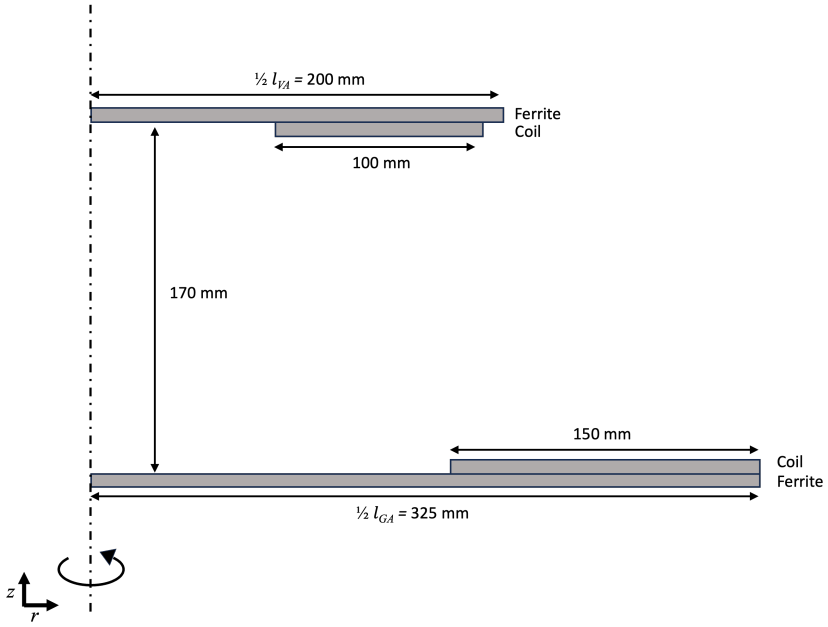

Figure 4.3. *Main geometrical dimensions of WPT device.*

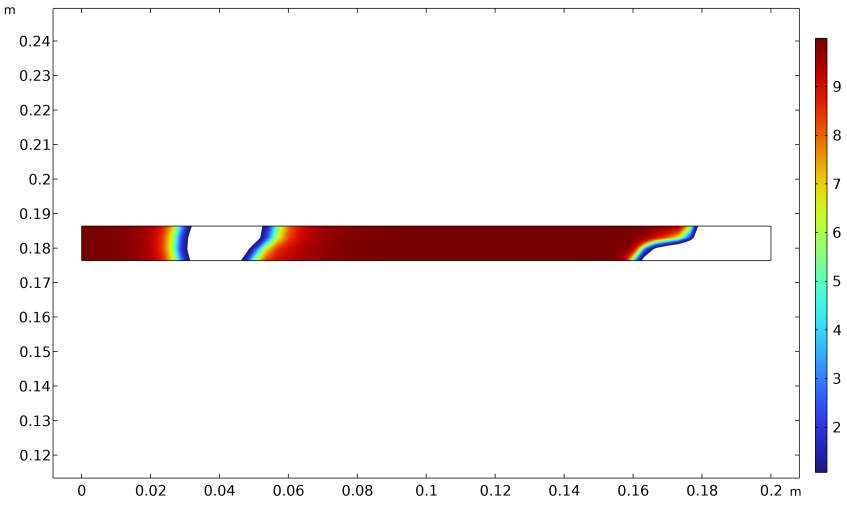

Figure 4.4. *TO of the ferrite for* $\mu_{r,max} = 10$*. The color bar refers to the value of* μ_r *for the regions with* $\rho > 0.5$*. Parts with* $\rho < 0.5$ *are not shown.*

$\mu_{r,max} = [10, 50, 100, 500, 1000, 2000]$. In Figures 4.4, 4.5, 4.6, and 4.7 the optimized configurations of the VA ferrite for $\mu_{r,max} = [10, 50, 500, 2000]$ are reported. In this case massive coil positioned under the ferrite is considered. The optimized solution for $\mu_{r,max} = 2000$ shows an evident "gray scale". This is due to the saturation phenomena as explained later in this section. Due to saturation optimization solver will tend to distribute material in overall the domain as considering material with lower permeability. In the context of these simulations, both the Helmholtz filter and projection techniques have been deliberately incorporated. The hyperbolic tangent projection is selected with a projection slope (β) equal to 8. The Helmholtz filter plays a crucial role in the optimization process by smoothing and regularizing the design,

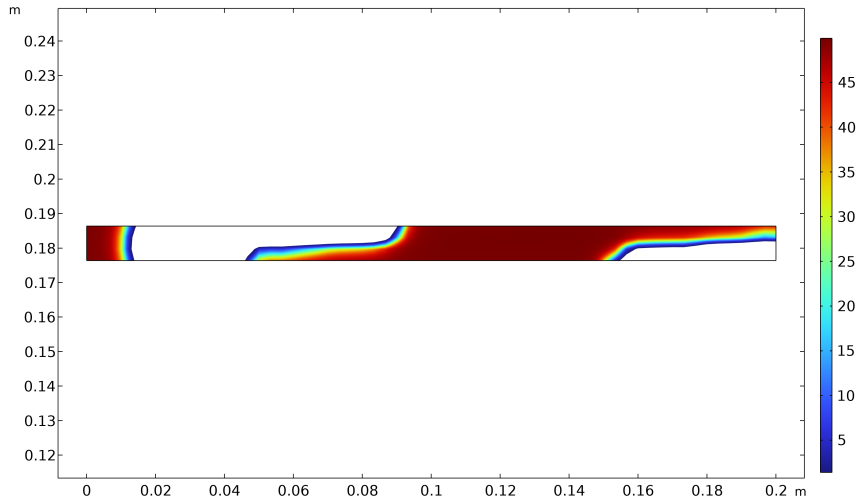

Figure 4.5. *TO of the ferrite for $\mu_{r,max} = 50$. The color bar refers to the value of μ_r for the regions with $\rho > 0.5$. Parts with $\rho < 0.5$ are not shown.*

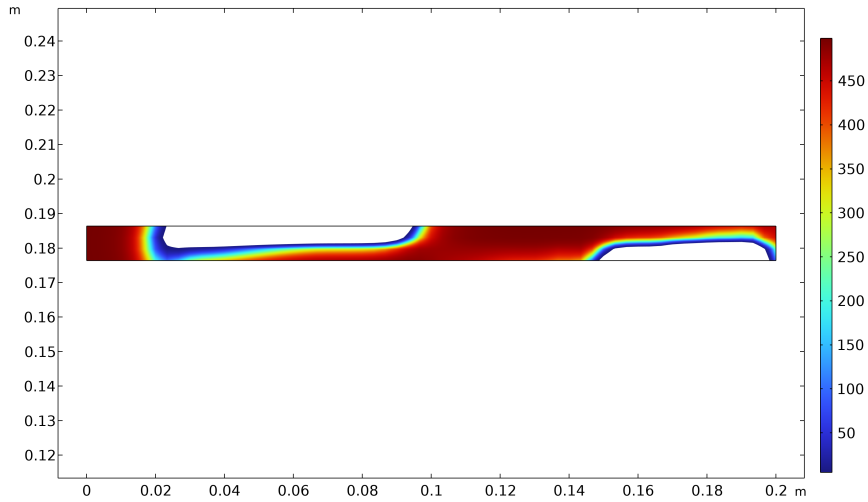

Figure 4.6. *TO of the ferrite for $\mu_{r,max} = 500$. The color bar refers to the value of μ_r for the regions with $\rho > 0.5$. Parts with $\rho < 0.5$ are not shown.*

which not only aids in reducing numerical artifacts but also promotes the convergence of the optimization algorithm. Simultaneously, the inclusion of projection techniques ensures that the optimized structure adheres to specified constraints, contributing to the maintenance of design feasibility. The combined utilization of the Helmholtz filter and projection techniques synergistically enhances the accuracy, robustness, and physical validity of the final Topology Optimization outcomes. Graphs in Figure 4.8 show the objective function, varying with the number of iterations for four values of $\mu_{r,max} = [10, 50, 500, 2000]$.

The x-axis represents the iteration number, in this case, set at 250.

The corresponding graphs for the volume occupancy are shown in Figure 4.9. The average volume factor on the y-axis represents the volume occupancy. The constraint in Eq. (4.10) is satisfied and $V/V_d = V_{frac}$ reaches 0.7.

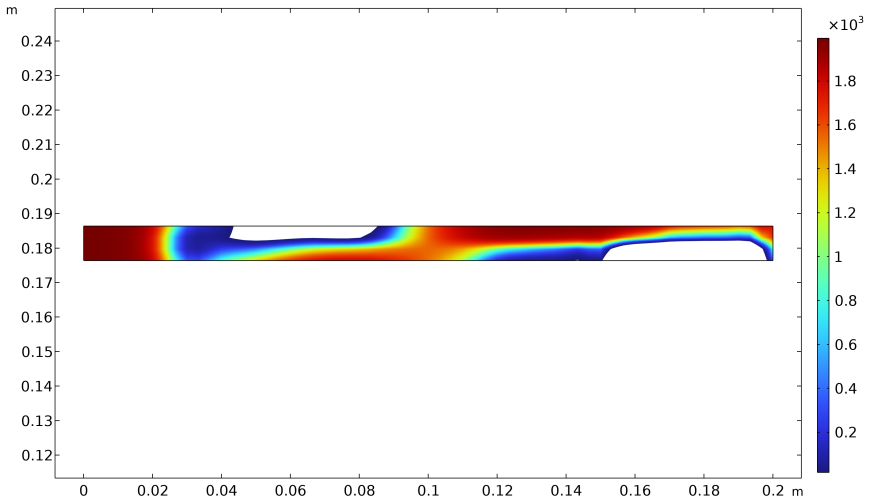

Figure 4.7. *TO of the ferrite for* $\mu_{r,max} = 2000$. *The color bar refers to the value of* μ_r *for the regions with* $\rho > 0.5$. *Parts with* $\rho < 0.5$ *are not shown.*

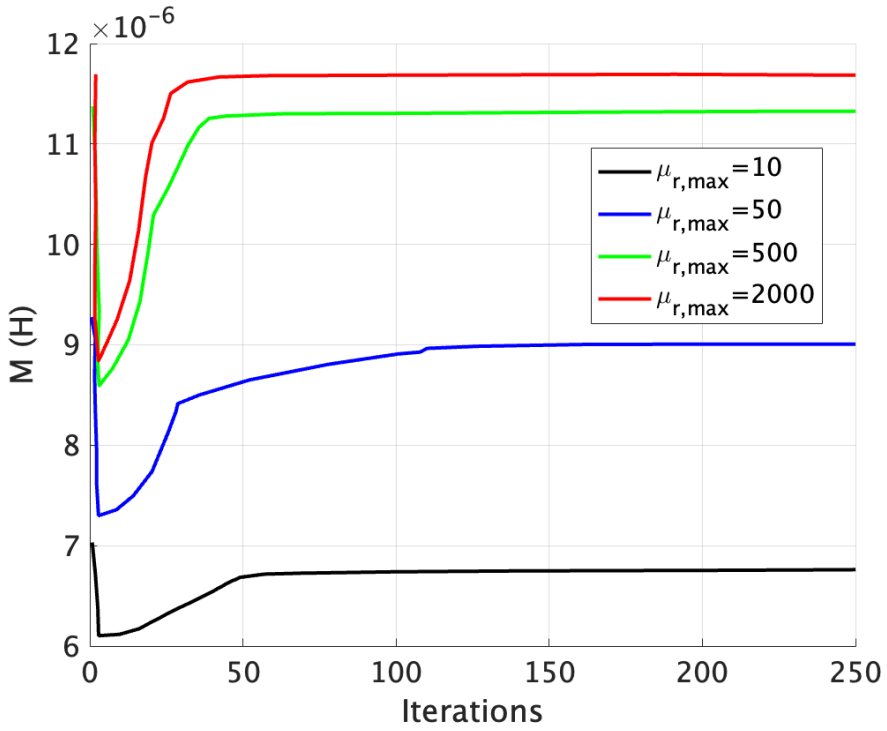

Figure 4.8. *Plot of the objective function M during the optimization produced for* $\mu_{r,max} = [10, 50, 500, 2000]$. *Massive coil considered.*

The trend of the mutual inductance as a function of iteration number can be understood by comparing it with the average volume factor graphs. At the beginning, the value of mutual inductance considers the total volume of the ferrite occupied by material as indicated on V_{frac} graphs. Then the volume occupied by ferrite will reach almost zero and so there's decreasing in the mutual inductance. In the end, M will almost reach the initial value. The initial decrease in M may be associated with the

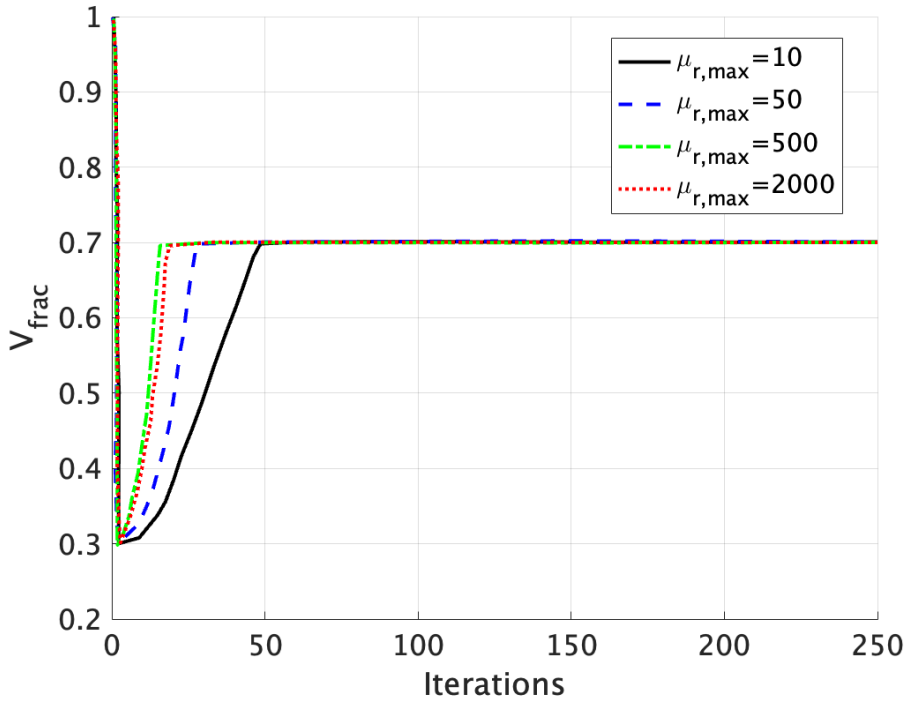

Figure 4.9. *Plot of the volume factor ($V_{frac} = 0.7$) during the optimization produced for $\mu_{r,max} = [10, 50, 500, 2000]$. Massive coil considered.*

optimization algorithm exploring various configurations of the ferrite material above the coil. As the optimization progresses, M returns to a value close to the initial one, indicating that the algorithm is converging to a design that satisfies both the optimization objective and practical constraints. That happens for values of $\mu_{r,max} = 2000$, it reaches more or less the same value because optimization tends to distribute the material over the entire ferrite as if it had lower permeability. For lower values of $\mu_{r,max}$, M reaches lower values.

The trend of the mutual inductance coefficient, as a function of the relative permeability is investigated in the case of a design domain filled with ferrite. This curve represents the relationship between mutual inductance M and the relative permeability of a material. It illustrates how changes in the material's relative permeability influence the magnetic coupling between coils in the system. The trend reported in Figure 4.10 shows a saturation of the mutual inductance when $\mu_{r,max} \approx 500$. The saturation region corresponds to an optimal range of relative permeability where the material is effectively conducting magnetic flux and contributing to improved mutual inductance. Once this range is reached, further changes in relative permeability may not lead to significant improvements in M. The corresponding mutual inductance values are listed in Table 4.1. In the table of mutual inductance M and relative permeability (μ_r) shown, there is a recognizable pattern that reflects the effect of different μ_r on the magnetic coupling between the coils. The values of M exhibit a notable trend, starting from $6.78 \cdot 10^{-6}$ H, increasing rapidly as μ_r rises, and eventually reaching a

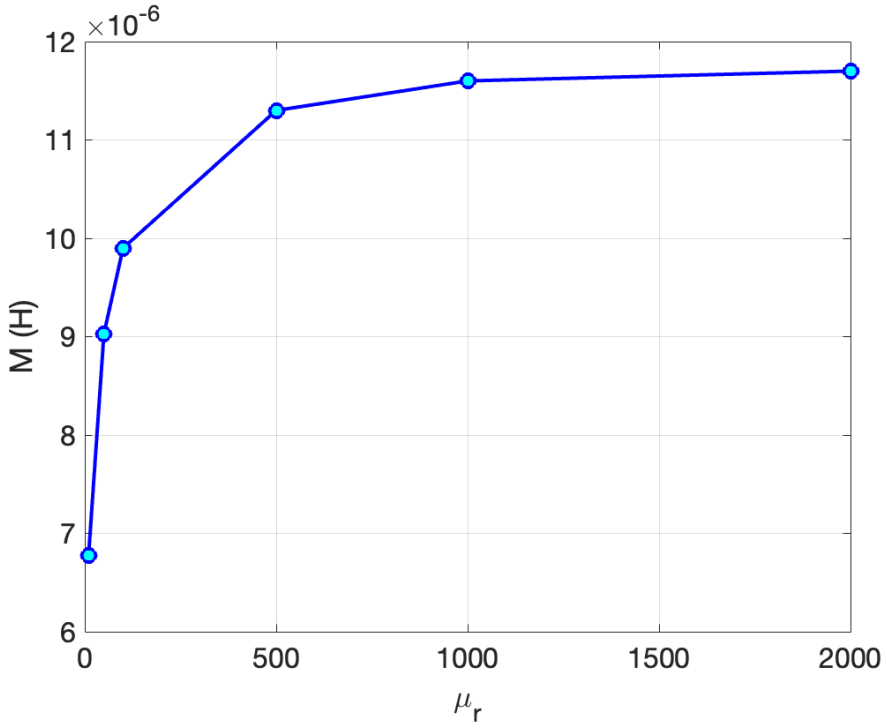

Figure 4.10. *Trend of mutual inductance M as a function of relative permeability μ_r. Massive coil considered.*

Table 4.1. *Mutual inductance of optimzed 2D axisymmetric WPT. Massive coil considered.*

Relative permeability (μ_r)	Mutual inductance (M) [H]
10	$6.78 \cdot 10^{-6}$
50	$9.03 \cdot 10^{-6}$
500	$1.14 \cdot 10^{-5}$
2000	$1.17 \cdot 10^{-5}$

plateau at approximately $1.14 \cdot 10^{-5}$ H. The plateau indicates that the system is saturated with respect to mutual inductance, and any further increase of μ_r will produce less improvement of M. The saturation point, where the increase in M flattens out, represents an optimal range of μ_r where the magnetic properties of the material are effectively utilized. Beyond this point, the material's magnetic characteristics are saturated, and additional increases in μ_r do not significantly enhance the magnetic coupling. The observed saturation behavior is crucial in understanding the limits of the magnetic properties of the material and helps identify the range where the material exhibits optimal performance in terms of mutual inductance. This information is valuable for designing and optimizing systems that rely on efficient magnetic coupling, such as Wireless Power Transfer applications.

Other simulations were then carried out taking into account the ferrite surrounding the coils. Coils are still considered massive coils. The modified geometry on the VA side is presented in Figure 4.11.

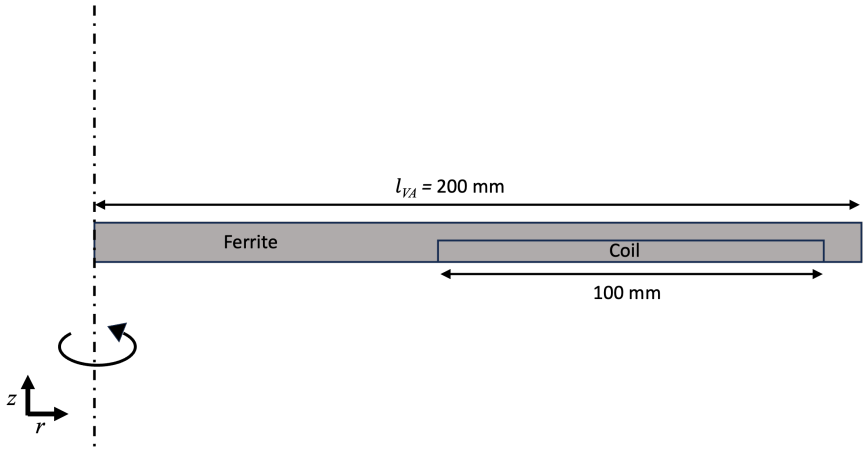

Figure 4.11. *Main geometrical dimensions of the Vehicle Assembly considering massive coil inside ferrite.*

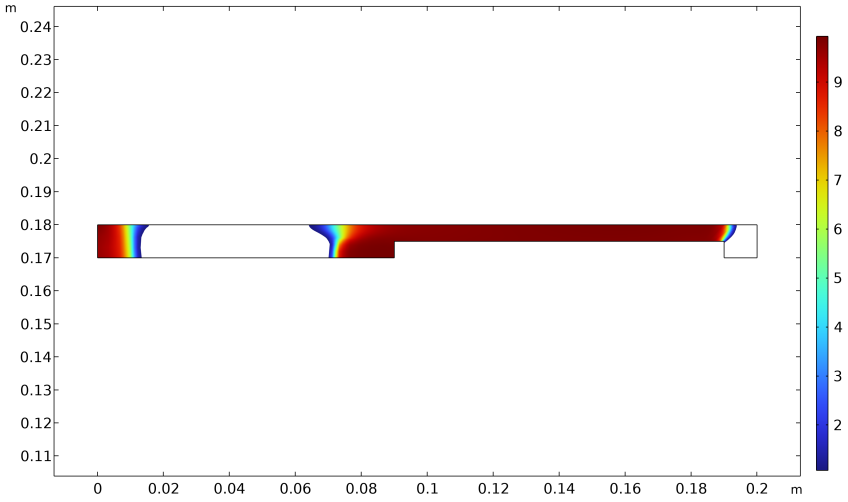

Figure 4.12. *TO of the ferrite for $\mu_{r,max} = 10$. The color bar refers to the value of μ_r for the regions with $\rho > 0.5$. Parts with $\rho < 0.5$ are not shown. Massive coil inside ferrite is considered.*

As can be seen in Figures 4.12, 4.13, 4.14, and 4.15 after the optimization, ferrite will be preferably positioned in the area above the coils. Topology Optimization is applied for $\mu_{rmax} = [10, 50, 500, 2000]$. In the course of these simulations, the Helmholtz filter as well as the projection technique have been deliberately integrated. A hyperbolic tangent projection is selected with a projection slope (β) equal to 8. The Helmholtz filter plays a pivotal role in enhancing the optimization process by smoothing and regularizing the design, thereby minimizing numerical artifacts and assisting in the convergence of algorithms. Simultaneously, the incorporation of projection techniques guarantees that the optimized structure adheres to predefined constraints, thereby maintaining design feasibility. By combining projection techniques and Helmholtz's filter, the ultimate outcomes' precision, resilience, and physical relevance in Topology Optimization are enhanced. The graphs in Figure 4.16 show the trend of the mutual

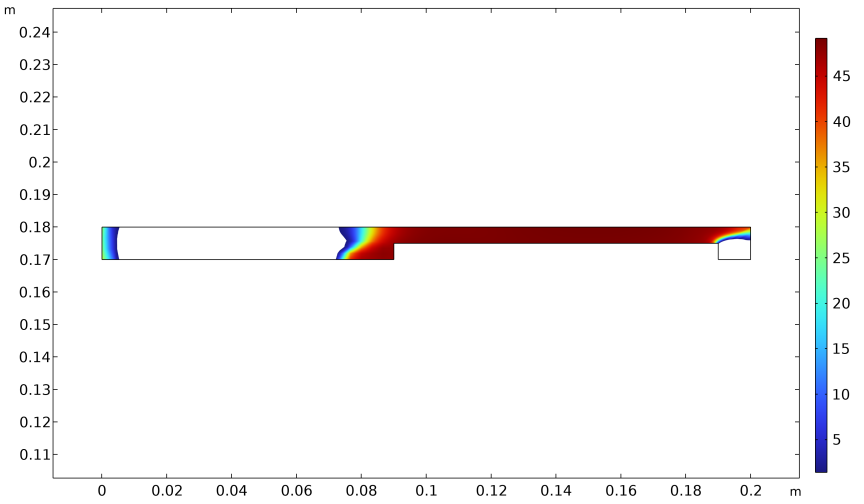

Figure 4.13. *TO of the ferrite for $\mu_{r,max} = 50$. The color bar refers to the value of μ_r for the regions with $\rho > 0.5$. Parts with $\rho < 0.5$ are not shown. Massive coil inside ferrite is considered.*

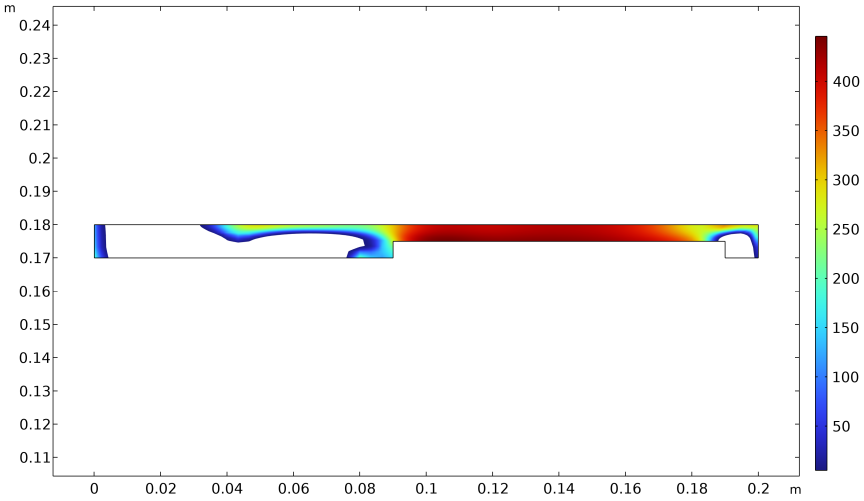

Figure 4.14. *TO of the ferrite for $\mu_{r,max} = 500$. The color bar refers to the value of μ_r for the regions with $\rho > 0.5$. Parts with $\rho < 0.5$ are not shown. Massive coil inside ferrite is considered.*

inductance as a function of the number of iterations.

The x-axis represents the number of iterations, here set to 150. The volume occupancy constraint is satisfied: V_{frac} reaches 0.7 for each of the chosen permeability values. This can be seen in Figure 4.17.

The variation in mutual inductance throughout the optimization iterations can be elucidated by juxtaposing it with the average volume factor graphs. Initially, the mutual inductance considers the entire volume of the ferrite, as indicated on the volume fraction graphs. Subsequently, the volume occupied by the ferrite material approaches nearly zero, leading to a decline in mutual inductance. Towards the end of the iterations, M converges to an approximation of its initial value. The initial decrease

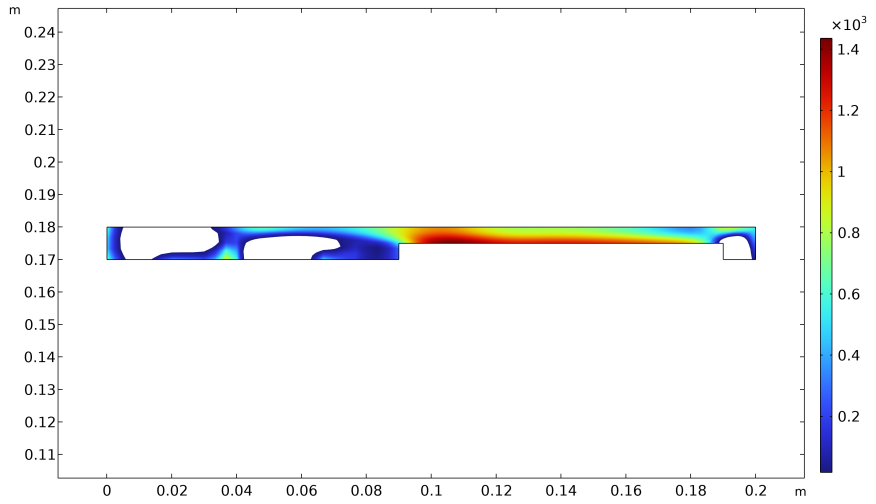

Figure 4.15. *TO of the ferrite for* $\mu_{r,max} = 2000$. *The color bar refers to the value of* μ_r *for the regions with* $\rho > 0.5$. *Parts with* $\rho < 0.5$ *are not shown. Massive coil inside ferrite is considered.*

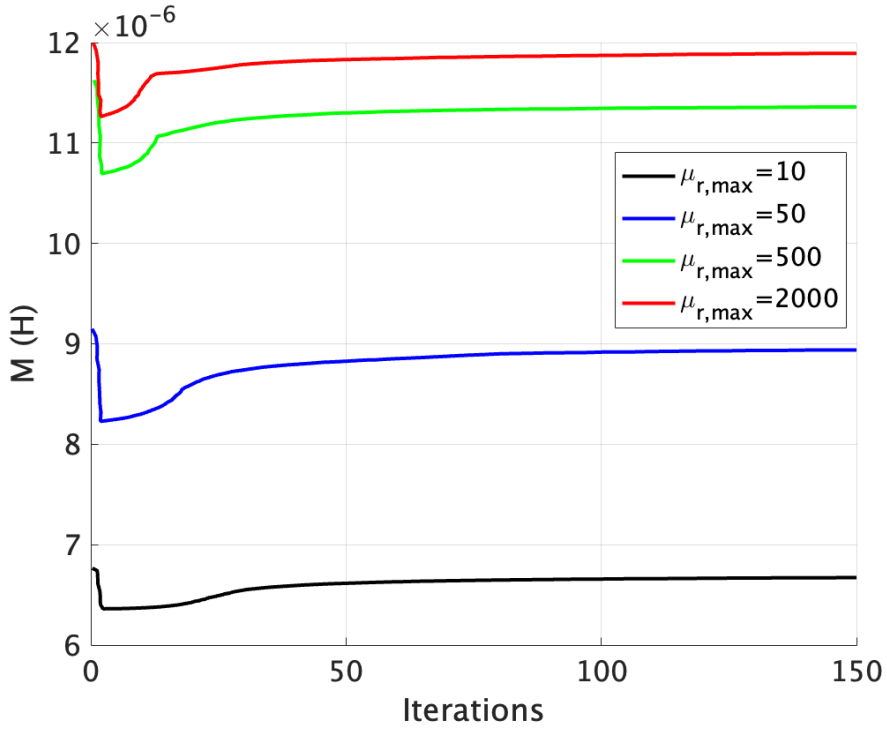

Figure 4.16. *Plot of the objective function M during the optimization produced for* $\mu_{r,max} = [10, 50, 500, 2000]$. *Massive coil inside ferrite considered.*

in M is linked to the optimization algorithm exploring diverse configurations of the ferrite material positioned around the coil. As the optimization unfolds, M returns to a value close to the initial one, signifying the algorithm's convergence toward a design that aligns with both optimization objectives and practical constraints. Generally, the final value of M attains lower values compared to the initial one due to the optimization

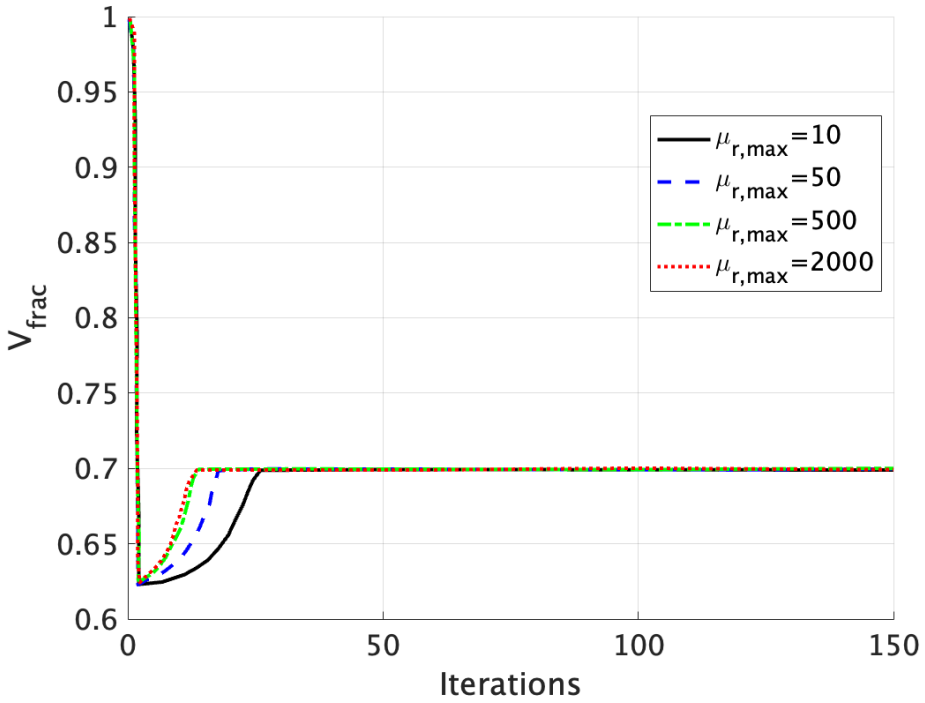

Figure 4.17. *Plot of the volume factor ($V_{frac} = 0.7$) during the optimization produced for $\mu_{r,max} = [10, 50, 500, 2000]$. Massive coil inside ferrite considered.*

strategy and volume constraint.

Saturation of the mutual inductance appears for $\mu_{r,max} \approx 500$ as shown in Figure 4.18.

The investigation into the behavior of the mutual inductance coefficient, concerning the relative permeability, is conducted within a design domain where ferrite surrounded the massive coil. The plotted curve in Figure 4.18 delineates the connection between mutual inductance M and the relative permeability of the material. This graphical representation elucidates how alterations in the material's relative permeability impact the magnetic coupling between coils within the system. The observed pattern in Figure 4.18 reveals a saturation phenomenon in the mutual inductance when the maximum relative permeability ($\mu_{r,max}$) reaches approximately 500. This saturation phase designates an optimal range of relative permeability, wherein the material efficiently conducts magnetic flux, thereby enhancing mutual inductance. Once this optimal range is attained, subsequent adjustments to the relative permeability may not yield substantial improvements in M. In essence, the graph highlights the critical interplay between relative permeability and mutual inductance, emphasizing the presence of an optimal saturation region where the material's magnetic properties contribute maximally to the efficiency of magnetic flux conduction and the enhancement of the mutual inductance. The mutual inductance for $\mu_{r,max} = [10, 50, 500, 2000]$ are listed on Table 4.2.

In the provided Table detailing mutual inductance M and relative permeability

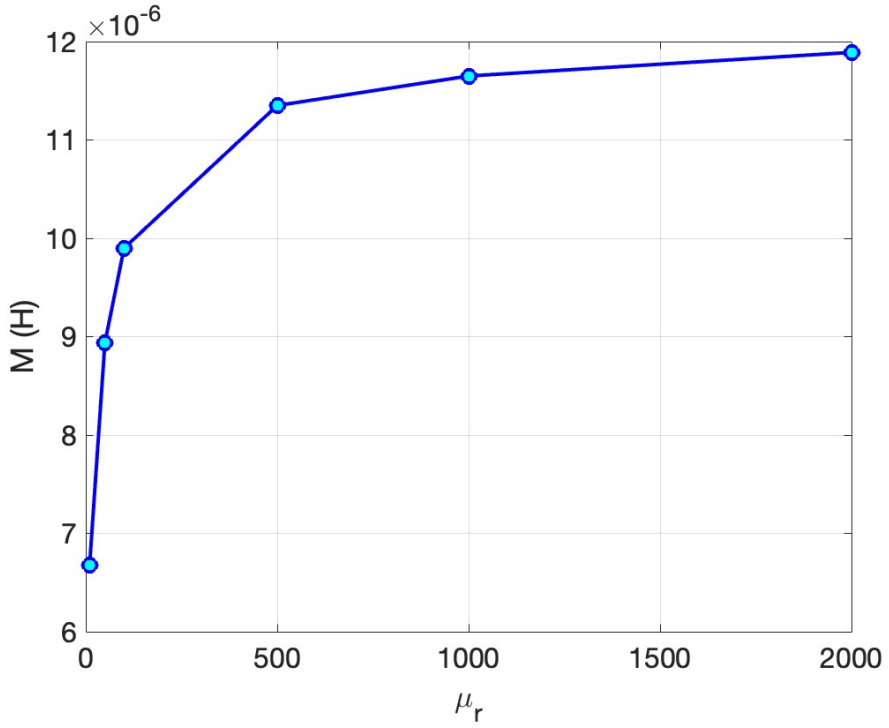

Figure 4.18. *Trend of mutual inductance M as a function of relative permeability μ_r. Massive coil inside ferrite considered.*

Table 4.2. *Mutual inductance of optimzed 2D axisymmetric WPT. Massive coil inside ferrite considered.*

Relative permeability (μ_r)	Mutual inductance (M) [H]
10	$6.68 \cdot 10^{-6}$
50	$8.94 \cdot 10^{-6}$
500	$1.14 \cdot 10^{-5}$
2000	$1.19 \cdot 10^{-5}$

($\mu_{r,max}$) values, a clear pattern emerges that sheds light on how changes in $\mu_{r,max}$ affect the magnetic coupling between coils. Starting at $6.68 \cdot 10^{-6}$ H, the M values exhibit a significant upward trend with increasing $\mu_{r,max}$ until reaching a plateau about $1.188 \cdot 10^{-5}$ H. This plateau signifies system saturation, indicating that further increments in $\mu_{r,max}$ result in diminishing returns for improving M. The saturation point, where M levels off, represents an optimal $\mu_{r,max}$ range where the material's magnetic properties are maximally utilized. Beyond this point, the material's magnetic characteristics become saturated, and further increases in $\mu_{r,max}$ do not significantly improve the magnetic coupling. Understanding this saturation behavior is crucial for recognizing the limits of the material's magnetic properties and identifying the range where optimal performance in mutual inductance is achieved. This information holds particular significance for the design and optimization of systems reliant on efficient magnetic coupling, such as Wireless Power Transfer applications. Engineers

and researchers can leverage this understanding to tailor material characteristics for optimal mutual inductance, enhancing the overall efficiency of systems employing magnetic coupling principles.

4.3 3D WPT device

Building on the previous discussion of WPT, the analysis now focuses on the dynamic interface between WPT technology and the automotive industry. The automotive sector is at the forefront of technological innovation. Sustainable and electric mobility is becoming increasingly important. Electric mobility is becoming increasingly popular due to growing awareness of CO_2 emissions and the lower total cost of ownership of Electric Vehicles (EVs) [108], [121].In this context, WPT is emerging as a disruptive solution, ushering in a new era for Electric Vehicles and redefining the infrastructure that supports them. The WPT technique offers a new strategy for improving the driving experience of Electric Vehicles, which are increasingly being studied for environmental reasons [117]. There are two types of power transfer coupling: capacitive coupling and inductive coupling. Capacitive coupling involves the transfer of power through the electric field between two closely spaced capacitive elements. Inductive coupling, on the other hand, relies on the magnetic field between coils for the Wireless Power Transfer. This work, as seen in the previous paragraph focuses on inductive coupling as the predominant approach to achieving wireless power transfer. Ampere's and Faraday's laws (see Chapter 1 formulas (1.1) and (1.2)), the two basic principles of Inductive Power Transfer, are fundamental and have opened countless applications and led to the development of modern electric machines [122]. With no electrical or mechanical contacts, Inductive Power Transfer technology for EVs charging is more user-friendly and safer than conventional wired charging. In addition, the technology offers the opportunity to dynamically charge the EVs battery during operation [123]–[125]. Many important international standards have been developed in recent years to regulate inductive wireless charging systems for Electric Vehicles [126]. The Society of Automotive Engineers (SAE) and Underwriters Laboratories (UL) provide the SAE J2954 and UL 2750 standards [127] and other related standards such as SAE J2847/6, SAE J2931/6, SAE J2836/6 and UL 2735 [128]. The former is an American organization that sets standards for the automotive and aviation industries, and the latter is a U.S.-based organization that performs safety testing and certification for a wide range of products, including wireless power systems. SAE published J2954 for *Wireless Power Transfer for Light-Duty Plug-In/Electric Vehicles and Alignment Methodology* for stationary charging starting from 2016 [120]. In this section, a 3D WPT device is examined. The geometry features are inspired by that indicated in the SAE standard [120]. In particular, for the following analysis, it will refer to the WPT3/Z3. WPT power classes are defined by the maximum input volt-amps drawn from the grid connection. SAE J2954 set WPT3 as 11.1 kVA to align with the European three-phase outlet rating. The vertical

distance over which the power must be transferred is an important parameter for the WPT system specification. Three Z-classes are defined to classify the range of ground clearances over which systems operate and are specified as Vehicle Assembly (VA) coil ground clearance. For Z3 the VA coil ground clearance is between 170 to 250 mm. The current supplied to the coil on the Ground Assembly (GA) side is $I = 1$ A while the ferrite below the coil has a width of $w = 510$ mm and a length of $l = 650$ mm. The optimization is performed on the VA side. The coil is open, meaning that no current is impressed on it while the ferrite above the coil has a dimension of $w = 400.5$ mm and a length of $l = 400$ mm. Topology Optimization is applied on the receiver ferrite (D).In this case, the objective function is the maximization of the mutual inductance and it is evaluated as in Equation (4.1). On the SAE standard, the boundary values for the coupling factor are indicated between 0.087 and 0.229 where the coupling factor is calculated as in Equation (4.2).

The simulation is solved as a single objective problem even if, in general, multi-objective problems are of great interest in the scientific community especially when dealing with WPT devices. Anyway, multi-objective analysis results are very complicated when using gradient-based methods in optimization problems [121], [129].

4.3.1 WPT with massive coil

In these subsections, the WPT coil is first considered to be a massive coil for ease of simulation. Topology Optimization has been applied to the ferrite of the vehicle assembly (D). In COMSOL®, first, the entire geometry has been constructed and the different materials assigned to each object as well as the mesh discretization. It is important to note that, during the simulations, it has been employed a geometry symmetrization strategy. Essentially, the simulation was conducted on only one-quarter of the total geometry, and subsequently, symmetry was applied to reflect the results across the entire structure. This approach optimizes the simulation process, reducing computational load and enabling an efficient evaluation of results, as symmetric conditions influence the system's behavior across the entire domain. When dealing with the objective function of Eq. (4.1) the symmetry must be considered and the just mentioned equation must be multiplied by 4. Figure 4.19 shows the main geometry parameters of the WPT with the massive coil. The objective function of the problem is the maximization of the mutual inductance and the starting point of the simulation is chosen as $\rho = 1$. The constraint is in the final volume occupied. The Topology Optimization problem can be summarized as follows:

$$\max M \tag{4.12}$$

$$V/V_d \leq 0.7 \tag{4.13}$$

where M denotes the mutual inductance and V_d is the whole volume of the design domain. As said in Chapter 3 the interpolation is an important step in the optimization

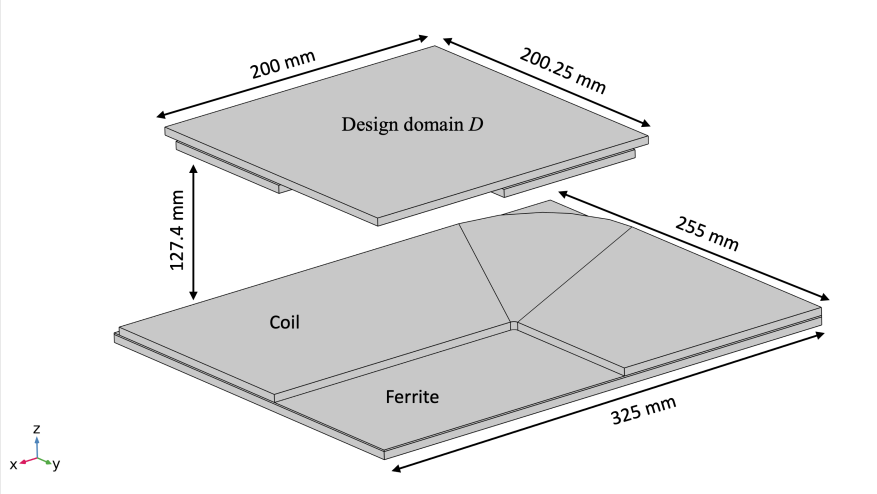

Figure 4.19. *Main geometrical dimensions of WPT device with massive coil.*

process. Since the physics chosen in this analysis is in the Magnetic Fields physics interface, therefore the material property needed to be interpolated is the relative permeability μ_r. The interpolation functions mapping the design variable ρ to the elemental material property μ_r is described using the power-law in Equation (4.5). In particular, in this analysis the values of μ_{rmax} considered are 10, 50, 500, 3300. The optimized domain will be obtained for each value of permeability chosen. In the simulation, both the Helmholtz filter and the projection are considered. A hyperbolic tangent projection is selected with a projection slope (β) equal to 8. The tolerance considered is 10^{-6} and the volume factor representing the final volume occupied is considered as $V/V_d = V_{frac} = 0.7$. In Figures 4.20, 4.21, 4.22, and 4.23 are presented the four optimization geometries each for every value of μ_{rmax} chosen.

As mentioned before, the objective function is the mutual inductance M. The change of M as a function of the iteration is shown in the different plots of Figure 4.24.

Equation (4.13) places a constraint on the occupied volume. In particular, the ratio V/V_d should be less or equal to 0.7. Figure 4.25 shows that this constraint is respected for $\mu_{r,max} = [50, 500, 3300]$ within 100 iterations. More iterations are needed for $\mu_{r,max} = 10$.

For the case where the $\mu_{r,max}$ is set to 10, a distinct behavior is observed in the optimization process. In this specific scenario, achieving the target volume fraction of 0.7 demands a higher number of iterations compared to other cases with different relative permeability values. The influence of $\mu_{r,max} = 10$ results in a more prolonged convergence towards the specified volume fraction constraint, indicating a distinctive sensitivity of the optimization process to this particular permeability setting. Simulation with 400 iterations has been performed and the results are plotted in Figure 4.26. The increase in the number of iterations corresponds to an increase in the simulation time, in this case up to 48 hours.

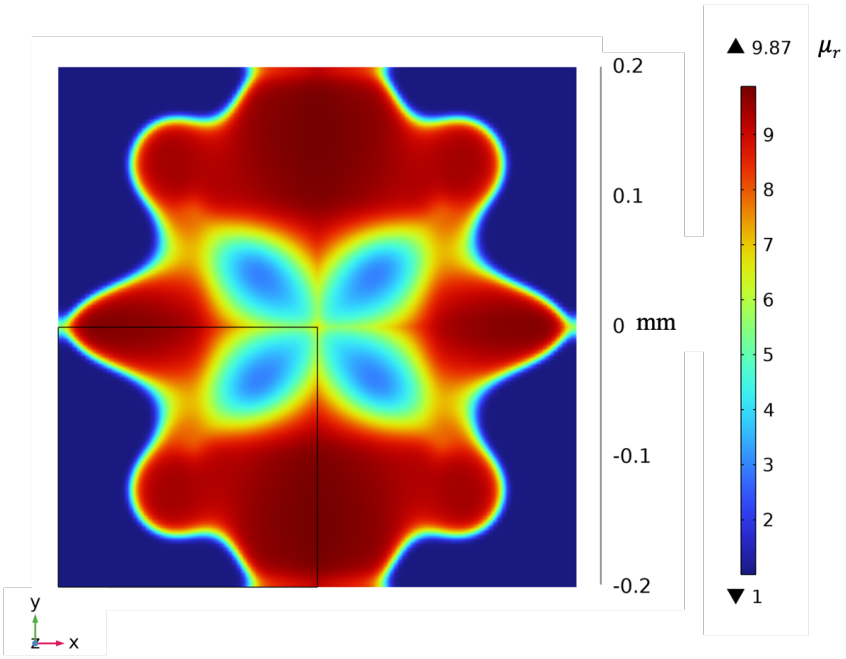

Figure 4.20. *TO of the ferrite for* $\mu_{r,max} = 10$. *The color bar refers to the value of* μ_r.

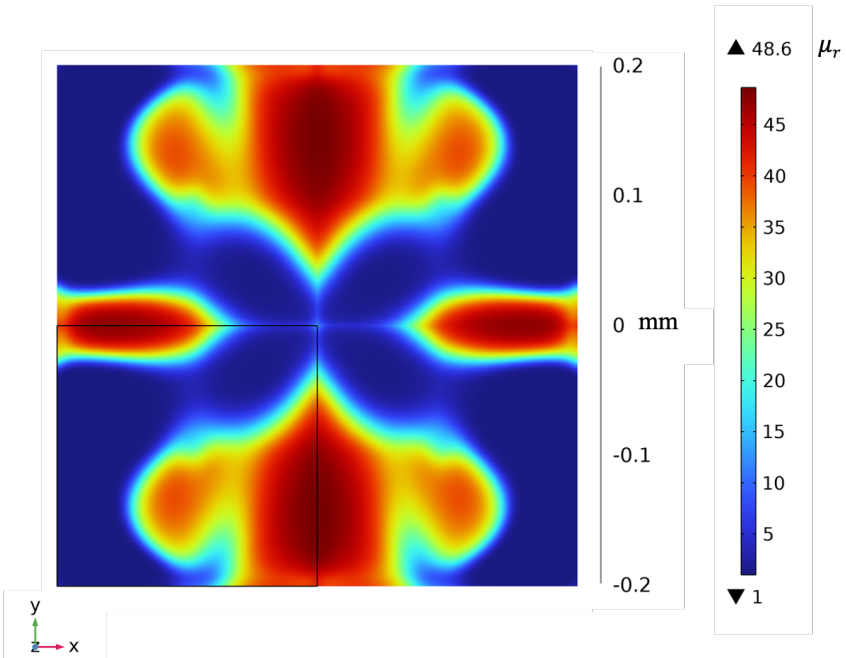

Figure 4.21. *TO of the ferrite for* $\mu_{r,max} = 50$. *The color bar refers to the value of* μ_r.

In the context of Topology Optimization, the influence of reduced relative permeability emerges as a critical factor affecting how the optimization process converges. The algorithm faces the challenge of determining an optimal material distribution to satisfy the prescribed volume fraction constraint as the material's susceptibility to magnetic fields decreases. The complex interaction between magnetic response and material distribution introduces complexity, which may require an increased num-

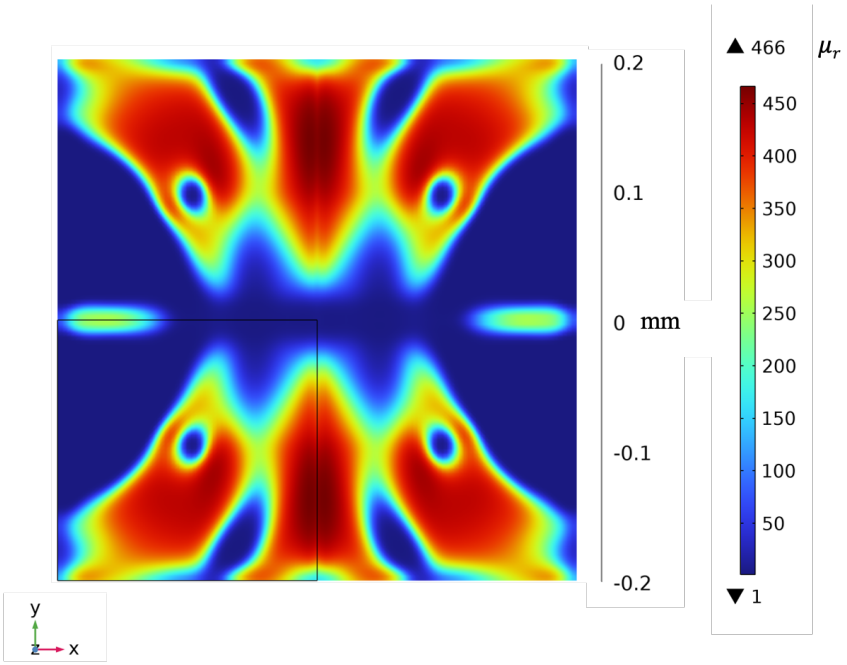

Figure 4.22. *TO of the ferrite for* $\mu_{r,max} = 500$. *The color bar refers to the value of* μ_r.

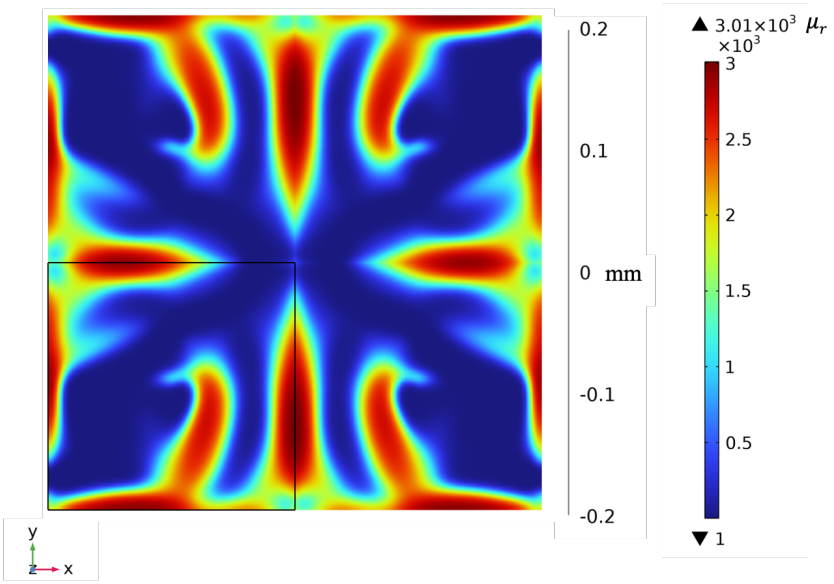

Figure 4.23. *TO of the ferrite for* $\mu_{r,max} = 3300$. *The color bar refers to the value of* μ_r.

ber of iterations for the algorithm to iteratively improve the topology and adapt to the specified volume fraction constraint. This phenomenon highlights the intricate relationship between the properties of the material, the magnetic behavior, and the efficiency of the topology optimization algorithm in achieving the desired results.

To comprehend the evolution of mutual inductance throughout iterative processes, meaningful insight can be gained by examining its relationship with average volume factor graphs. In the initial stages, the mutual inductance value takes into account the entirety of the ferrite volume occupied by material, a depiction manifests in the V_{frac}

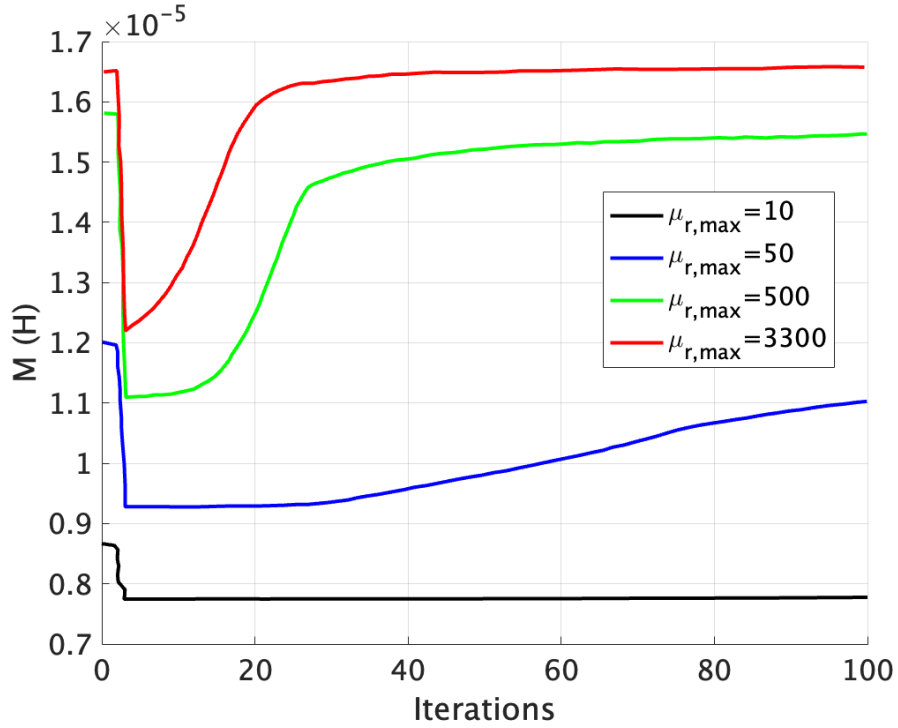

Figure 4.24. *Plots of the objective function M during the optimization produced by the value of* $\mu_{r,max} = [10, 50, 500, 3300]$. *3D massive coil considered.*

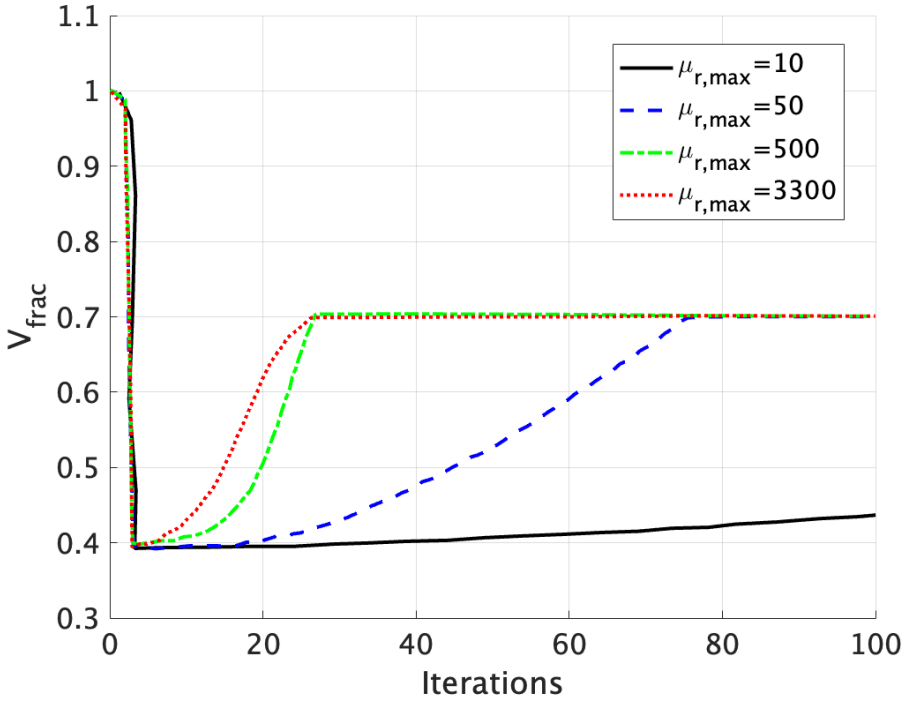

Figure 4.25. *Plots of the volume factor* ($V_{frac} = 0.7$) *during the optimization produced by value of* $\mu_{r,max} = [10, 50, 500, 3300]$. *3D massive coil considered.*

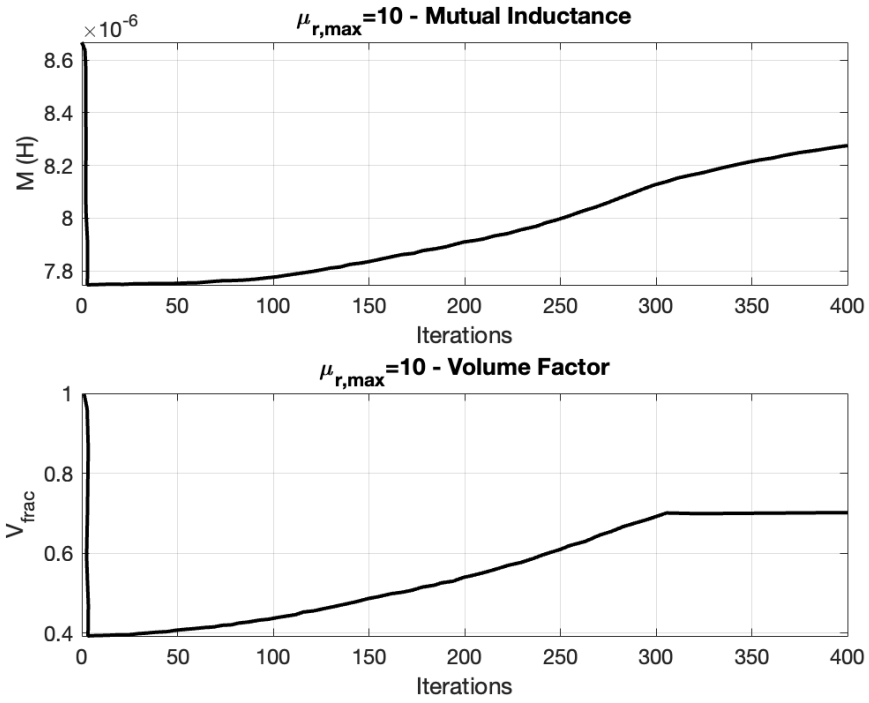

Figure 4.26. *Plots of the mutual inductance (above) and volume factor (below) for* $\mu_{r,max} = 10$ *with 400 iterations.*

graphs. As the optimization progresses, the volume fraction of ferrite gradually approaches zero, instigating a corresponding decrease in mutual inductance. However, as the optimization reaches its conclusion, M converges to a value closely mirroring its initial state. The initial decline in M finds an association with the exploration phase of the optimization algorithm, where diverse configurations of ferrite material above the coil are scrutinized. As the algorithm advances, M retraces its steps, converging to a value proximate to its initial condition. This convergence signifies that the optimization process aligns with the specified objectives and practical constraints. Notably, for cases where $\mu_{r,max} = 3300$, M stabilizes at a comparable level. This stabilization is attributed to the optimization strategy, which tends to distribute the material uniformly across the entire ferrite, essentially treating it as if it possessed higher permeability. Conversely, lower values of $\mu_{r,max}$ lead to lower M values, emphasizing the sensitivity of M to variations in the maximum relative permeability. The trend of the mutual inductance as a function of the relative permeability is shown in Fig. 4.27. A saturation appears for $\mu_{rmax} \approx 500$. The investigation into the behavior of the mutual inductance coefficient, concerning the relative permeability, is undertaken within a design domain filled with ferrite. The focal point of this analysis is a curve that delineates the intricate relationship between M and the relative permeability of the material. This graphical representation illustrates the profound impact that alterations in the material's relative permeability can exert on the magnetic coupling between coils within the system. As elucidated by the trend depicted in Fig. 4.27, a noteworthy saturation

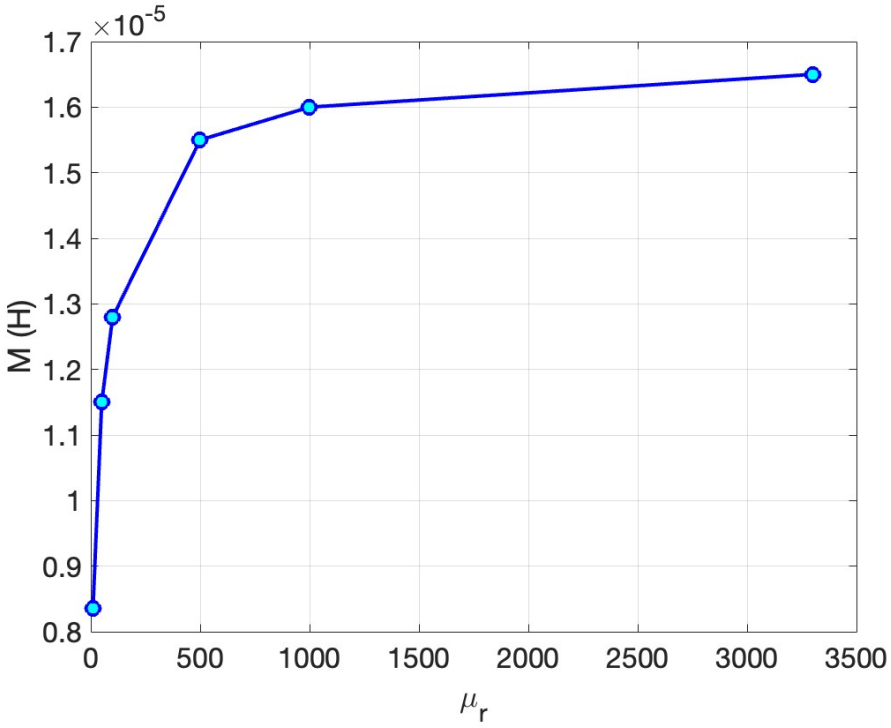

Figure 4.27. *Trend of mutual inductance M as a function of relative permeability μ_r. 3D massive coil considered.*

phenomenon in mutual inductance is observed when the maximum relative permeability ($\mu_{r,max}$) reaches approximately 500. This saturation region signifies an optimal range of relative permeability, wherein the material efficiently conducts magnetic flux, thereby contributing significantly to the enhancement of mutual inductance. Once this optimal range is attained, further adjustments to the relative permeability may not yield substantial improvements in M. For a detailed insight into the corresponding mutual inductance values, please refer to Table 4.3. The values in this Table provide a comprehensive overview of the mutual inductance at various points along the relative permeability curve. Extending the analysis beyond the graphical representation, the listed values offer a quantitative perspective on how changes in relative permeability manifest in the corresponding mutual inductance values. This comprehensive exploration is essential for understanding the nuanced interplay between material properties and magnetic coupling, ultimately informing the design and optimization of systems reliant on efficient magnetic interactions.

The corresponding mutual inductance values for $\mu_{rmax} = [10, 50, 500, 3300]$ are given in Table 4.3.

Within the presented Table detailing mutual inductance M and relative permeability (μ_r) values, a conspicuous pattern unfolds, shedding light on the profound influence of varying μ_r on the magnetic coupling between coils. The M values trace a discernible trajectory, initiating from $8.35 \cdot 10^{-6}$ H, escalating swiftly with the ascent of $\mu_{r,max}$, and ultimately stabilizing at a plateau around $1.55 \cdot 10^{-5}$ H. This plateau sig-

Table 4.3. *Mutual inductance of optimzed 3D WPT. 3D massive coil considered.*

Relative permeability (μ_r)	Mutual inductance (M) [H]
10	$8.35 \cdot 10^{-6}$
50	$11.55 \cdot 10^{-6}$
500	$1.55 \cdot 10^{-5}$
3300	$1.65 \cdot 10^{-5}$

nifies the system's saturation concerning mutual inductance, indicating that further increments in μ_r yield diminishing returns for the improvement of M. The point of saturation, where the increase in M levels off, denotes an optimal range of μ_r where the material's magnetic properties are maximally harnessed. Beyond this juncture, the material's magnetic characteristics become saturated, and additional increments in μ_r no longer yield substantial enhancements in magnetic coupling. The observed saturation behavior is pivotal in comprehending the limitations of the material's magnetic properties and facilitates the identification of the range wherein the material attains optimal performance about mutual inductance. This insight holds significant value for the design and optimization of systems reliant on efficient magnetic coupling, particularly in applications like WPT. By recognizing the saturation dynamics, it is possible to make informed decisions, tailoring material properties to achieve optimal performance in terms of mutual inductance and, consequently, enhancing the overall efficiency of systems leveraging magnetic coupling principles. In these simulations, both the Helmholtz filter and projection are considered. Helmholtz filters are commonly used in Topology Optimization as a regularization technique. In the context of Topology Optimization, Helmholtz filtering is used to achieve a more gradual transition between different material densities. This is important because sharp transitions between regions of different densities can lead to numerical instabilities and checkerboard patterns in the optimized results. The differences between using and not using the filter are shown in Figure 4.28.

With the filter, the material distribution is more homogeneous. The material distribution is likely to be smoother, promoting a more gradual transition between different material densities. This leads to designs that are physically realistic and manufacturable. Instead without filtering, the material distribution exhibits sharp transitions. The filter helps suppress checkerboard patterns, which are undesirable artifacts in Topology Optimization. The absence of these patterns indicates a more reliable and physically meaningful solution. In this example, a predefined iteration limit of 100 was set, but convergence was not achieved within this limit. As a result, the optimized solution in Figure 4.28 (b) shows a noticeable "gray scale". It is plausible that using a higher number of iterations could potentially alleviate this problem. This suggestion implies that a more extensive iteration process may be necessary to achieve convergence and effectively optimize the topology in the identified problem region.

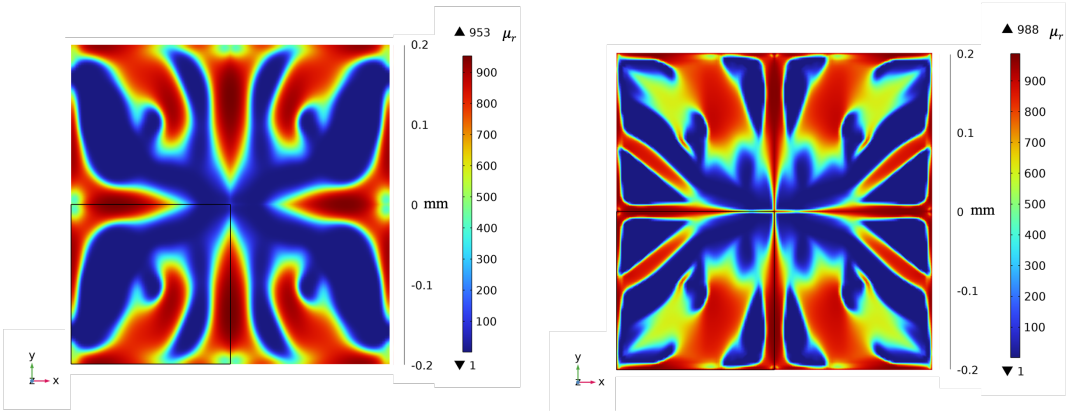

(a) **(b)**

Figure 4.28. *Material distribution during optimization produced by using $\alpha = 7$ (see Eq. (4.5)) with Helmholtz filter (a) and without Helmholtz filter (b). The color bar refers to the value of μ_r.*

4.3.2 WPT WITH SINGLE-TURN COILS

In this subsection, coils with turns of a WPT system are considered. The ferrite is surrounding the coils. The Topology Optimization technique is applied to the ferrite of the Vehicle Assembly. COMSOL® is used to construct the entire geometry. The different materials are assigned to each object and the mesh discretization is performed. Note that a geometric symmetrization strategy is used in the simulations. In essence, the simulation is performed on only one-quarter of the total geometry and then symmetry is applied to reflect the results over the entire structure. This reduces the computation time and allows for a more effective evaluation of the results since symmetrical conditions influence the system behavior over the entire range. The main geometry features are presented in Figure 4.29. On the VA side 8 turns are considered as indicated on [120] while on GA side 8 equivalent turns are considered.

The starting point of the simulation is chosen as $\rho = 1$, and the objective function of the problem is the maximization of the mutual inductance. The constraint is on the final occupancy of the volume. The Topology Optimization problem can be summed up as follows:

$$\max M \tag{4.14}$$

$$V/V_d \leq 0.7 \tag{4.15}$$

where M denotes the mutual inductance and V_d is the whole volume of the design domain. The M is evaluated as in Equation (4.1) where the symmetry geometry must be considered. Magnetic Field interface is chosen in COMSOL®. Therefore the relative permeability μ_r, is the material property interpolated by the linear power-law in Equation (4.5). In the simulations performed, the single-turn coils were included inside the ferrite. Topology Optimization is applied on the ferrite on VA side. As

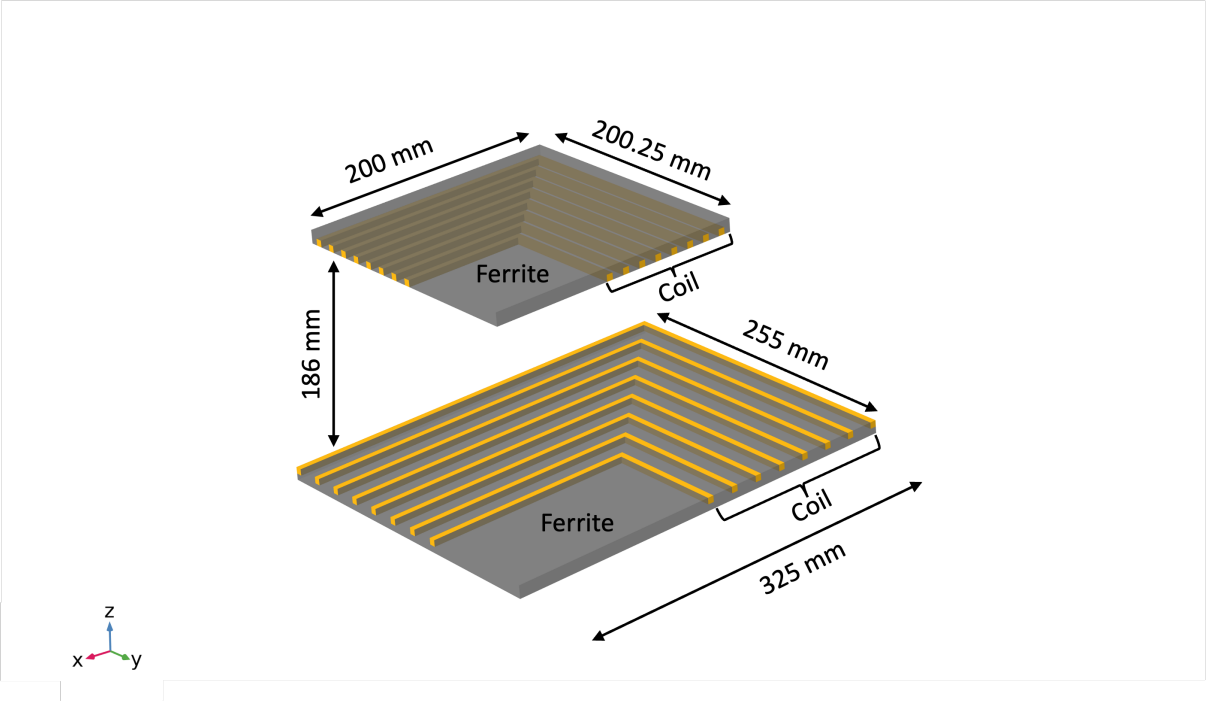

Figure 4.29. *Main geometrical dimensions of WPT device with single-turn coils.*

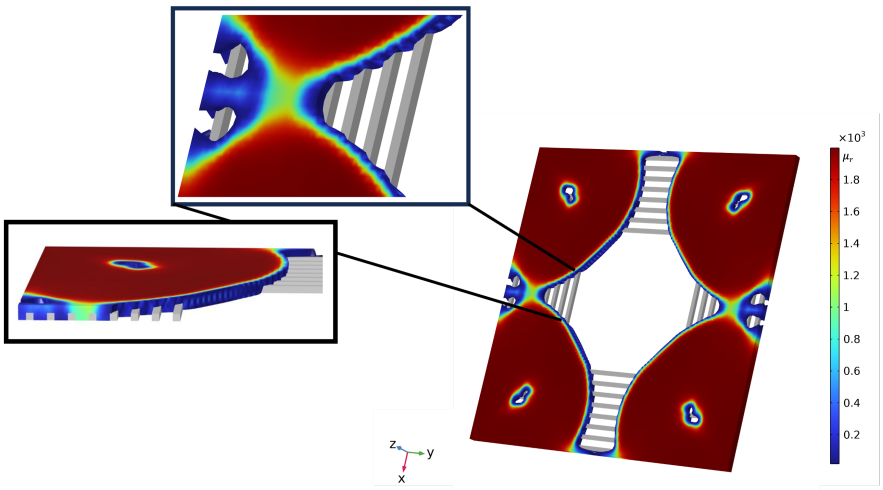

Figure 4.30. *TO with zoom on coils surrounding the ferrite. Value of* $\mu_{r,max}$ *is set on* 2000.

shown in Figure 4.30, upon completion of the optimization, the ferrite on the VA side encapsulates the coils, forming a coherent structure without the presence of exotic geometries. Therefore, the subsequent optimization geometries are presented from a planar perspective, focusing on the overall arrangement of the ferrite material.

The optimized geometries presented in Figures 4.31, 4.32, 4.33 and 4.34 are obtained for $\mu_{r,max} = [10, 50, 500, 3300]$. In the simulations both the Helmholtz filter and projection are considered.A hyperbolic tangent projection is selected with a projection slope (β) equal to 8. The number of iterations is set to 250.

After applying topology optimization to the ferrite on the VA side, it is observed

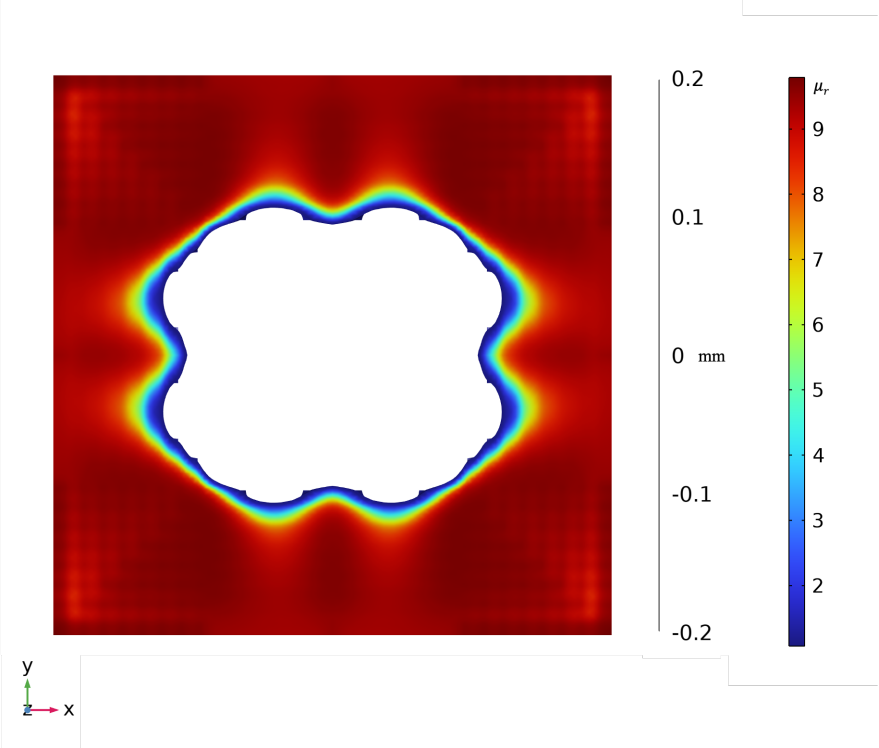

Figure 4.31. *TO of the ferrite for* $\mu_{r,max} = 10$. *The color bar refers to the value of* μ_r.

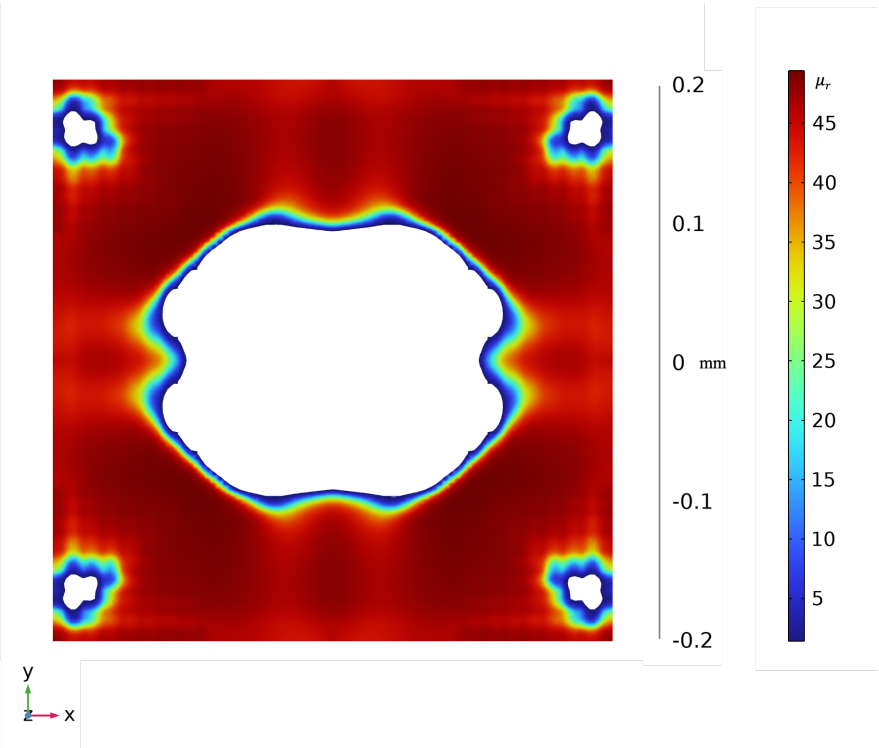

Figure 4.32. *TO of the ferrite for* $\mu_{r,max} = 50$. *The color bar refers to the value of* μ_r.

that the ferrite tends to be positioned above the coils, in the region corresponding to the coils, rather than at the center of VA ferrite.

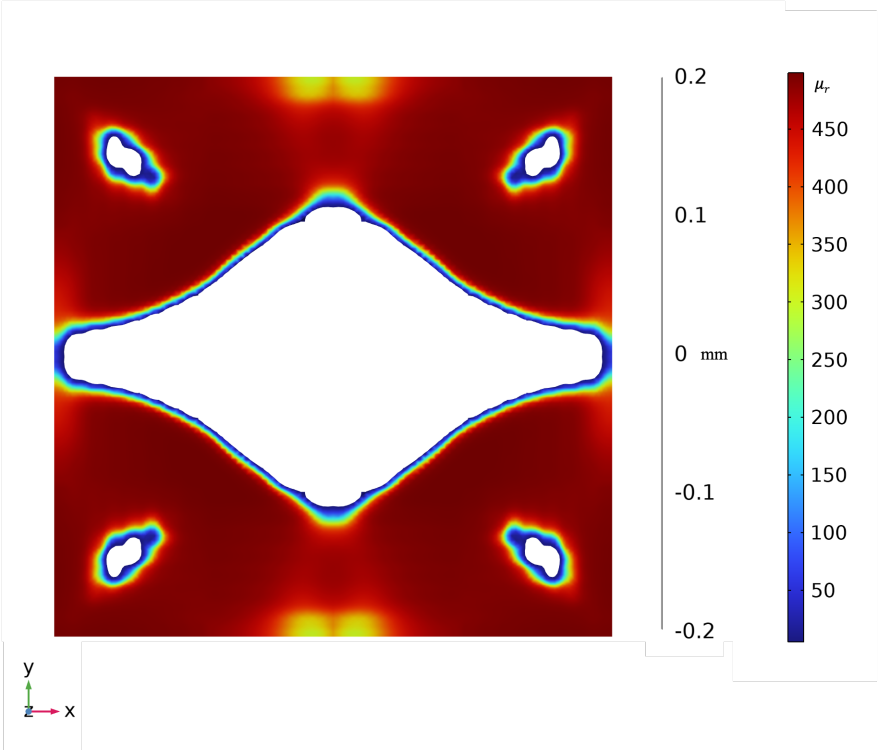

Figure 4.33. *TO of the ferrite for* $\mu_{r,max} = 500$. *The color bar refers to the value of* μ_r.

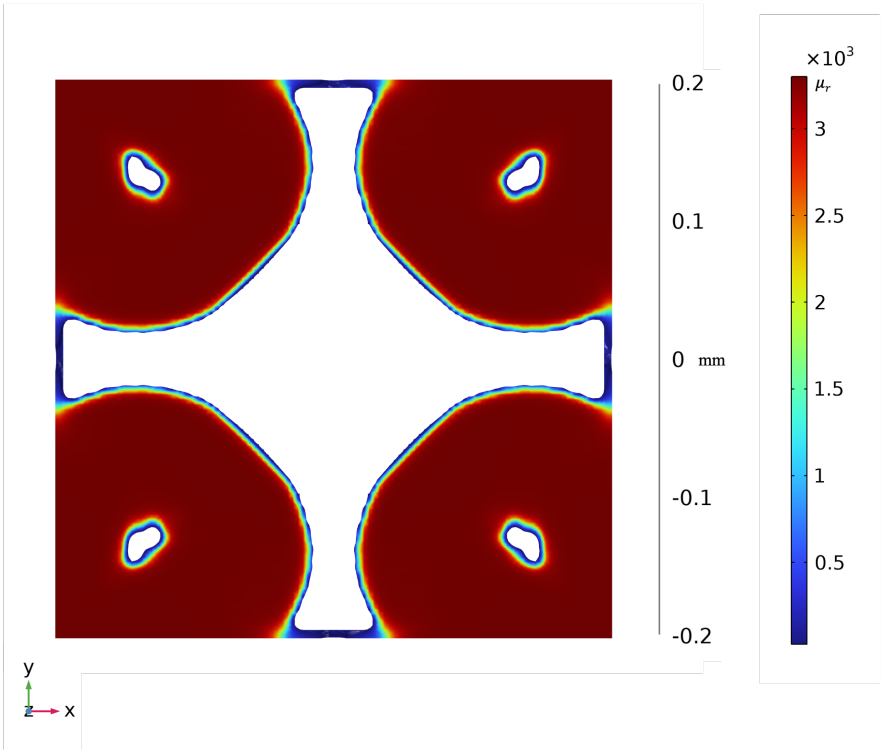

Figure 4.34. *TO of the ferrite for* $\mu_{r,max} = 3300$. *The color bar refers to the value of* μ_r.

As indicated in Equation 4.14, the objective function is the mutual inductance. Fig. 4.35 shows the trend of the mutual inductance with respect to the number of

iterations.

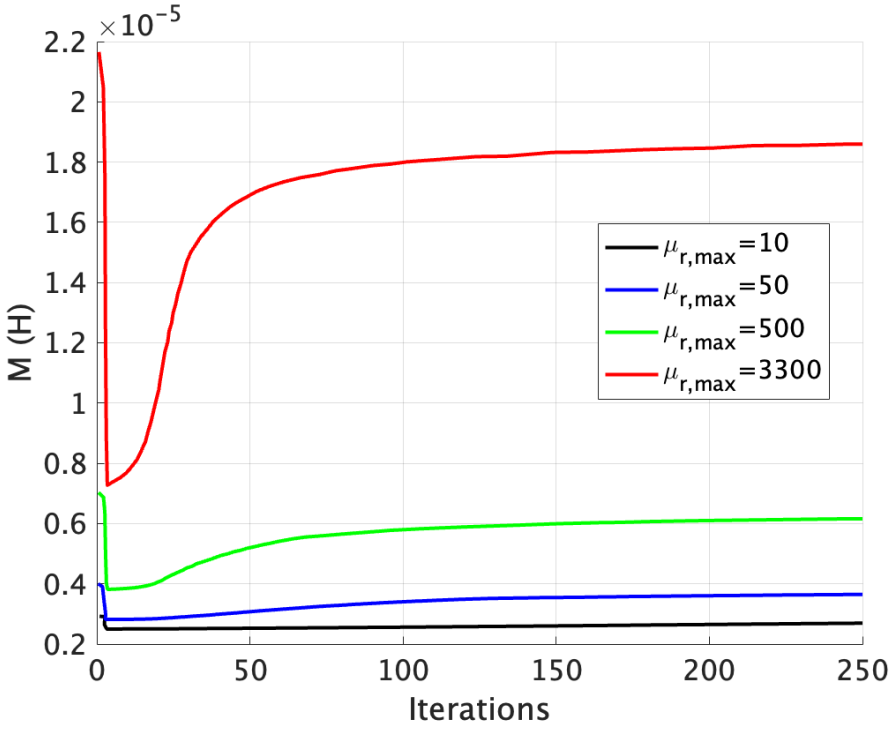

Figure 4.35. *Plots of the objective function M during the optimization produced by the value of* $\mu_{r,max} = [10, 50, 500, 3300]$. *3D separate coils considered.*

A zoom of the graphs for $\mu_{r,max} = [10, 50]$ is shown in Fig. 4.36 and Fig. 4.37 respectively.

The constraint on the volume occupied is placed on Equation (4.15). Figure 4.38 shows that this constraint is respected for the value of $\mu_{r,max} = [50, 500, 3300]$ within 250 iterations. A higher number of iterations is required for $\mu_{r,max} = 10$.

As can be seen in Fig. 4.38, 250 iterations are not enough to reach the constraint of 0.7 on the volume domain. Simulation has therefore been performed for 500 iterations as shown in Fig. 4.39.

To gain insight into the evolution of the mutual inductance during the iterative processes, it is instructive to examine its correlation with the average volume factor graphs. In the early stages, the mutual inductance value includes the entire ferrite volume occupied by the material, as reflected in the V_{frac} plot. As the optimization progresses, the volume fraction of ferrite gradually approaches zero, resulting in a corresponding decrease in mutual inductance. However, as the optimization nears completion, M converges to a value close to its initial state. The initial decrease in M is related to the exploration phase of the optimization algorithm, where different configurations of ferrite material above the coil are examined. As the algorithm progresses, M retraces its steps and converges to a value close to its initial state. For $\mu_{r,max} = 10$ can be noticed how the influence of reduced relative permeability emerges as a critical factor affecting the convergence of the optimization process in the context of Topology

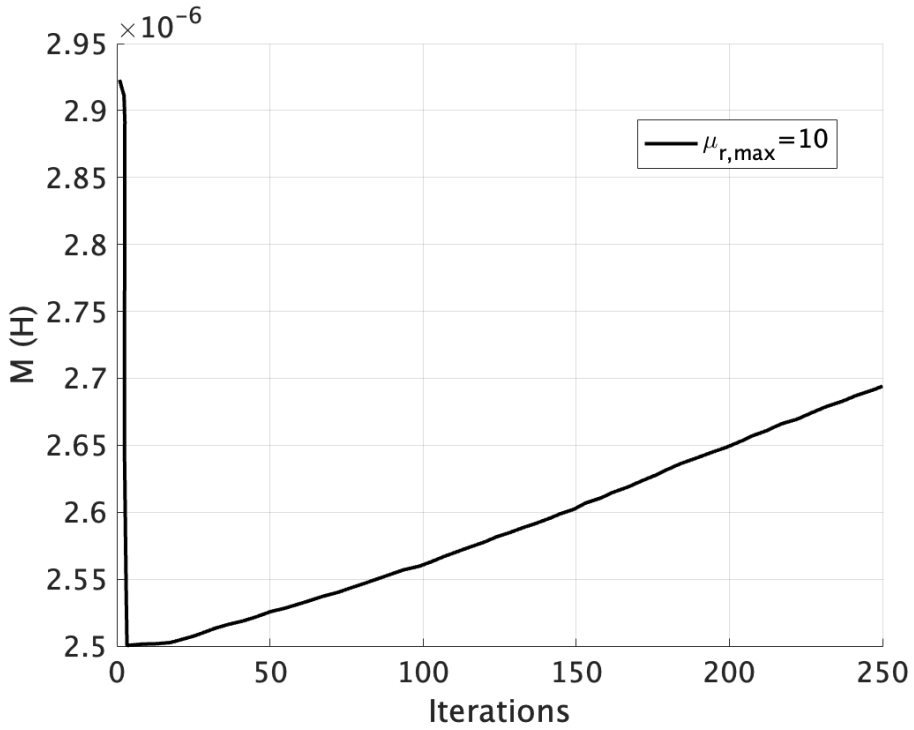

Figure 4.36. *Plots of the objective function M during the optimization produced by the value of* $\mu_{r,max} = 10$*. 3D separate coils considered.*

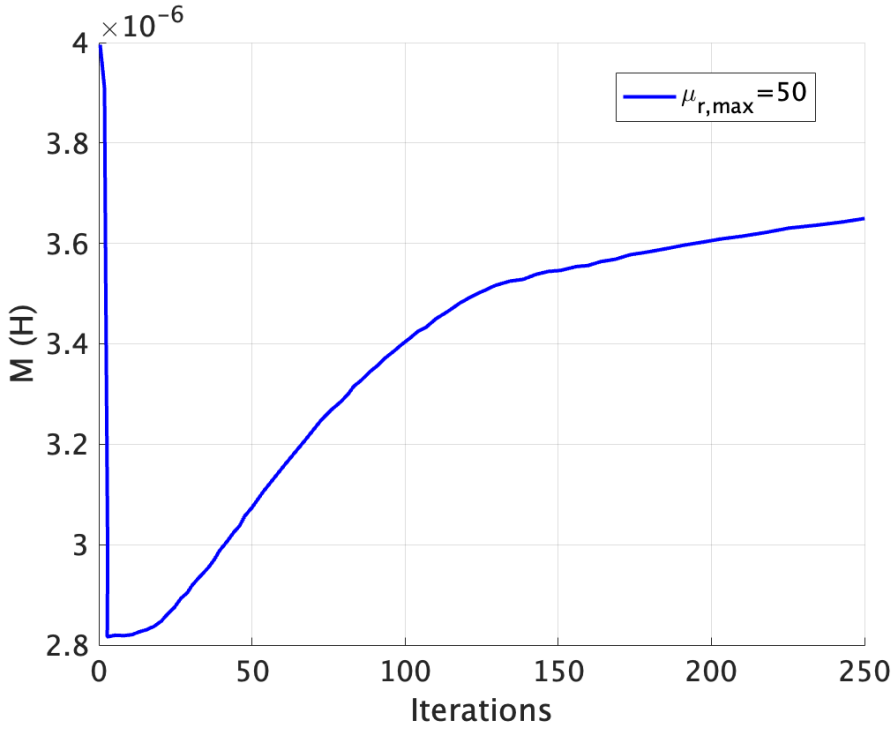

Figure 4.37. *Plots of the objective function M during the optimization produced by the value of* $\mu_{r,max} = 50$*. 3D separate coils considered.*

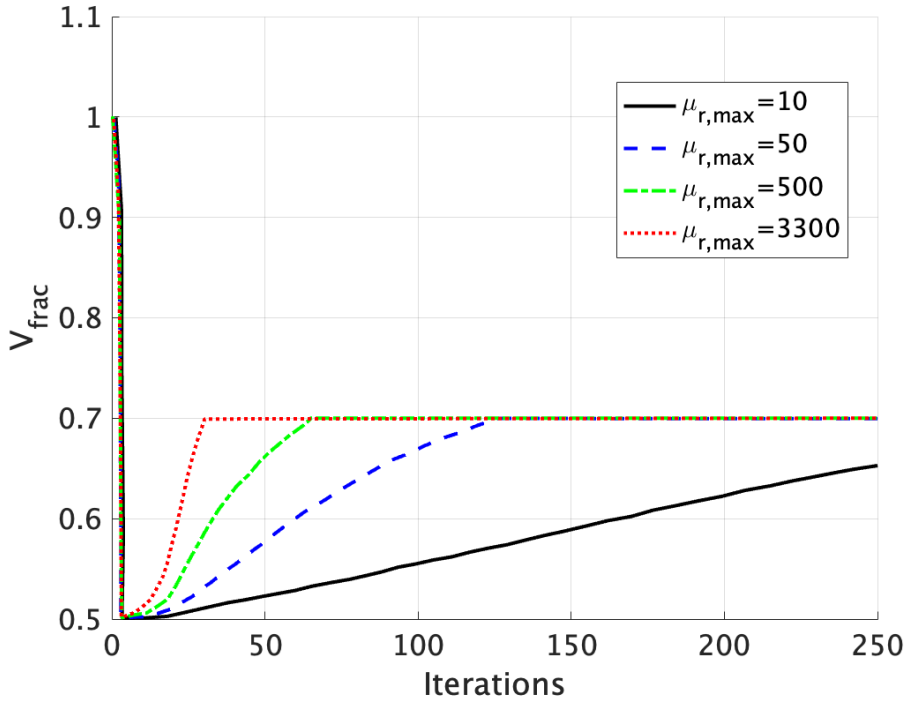

Figure 4.38. *Plots of the volume factor ($V_{frac} = 0.7$) during the optimization produced by value of $\mu_{r,max} = [10, 50, 500, 3300]$. 3D separate coils considered.*

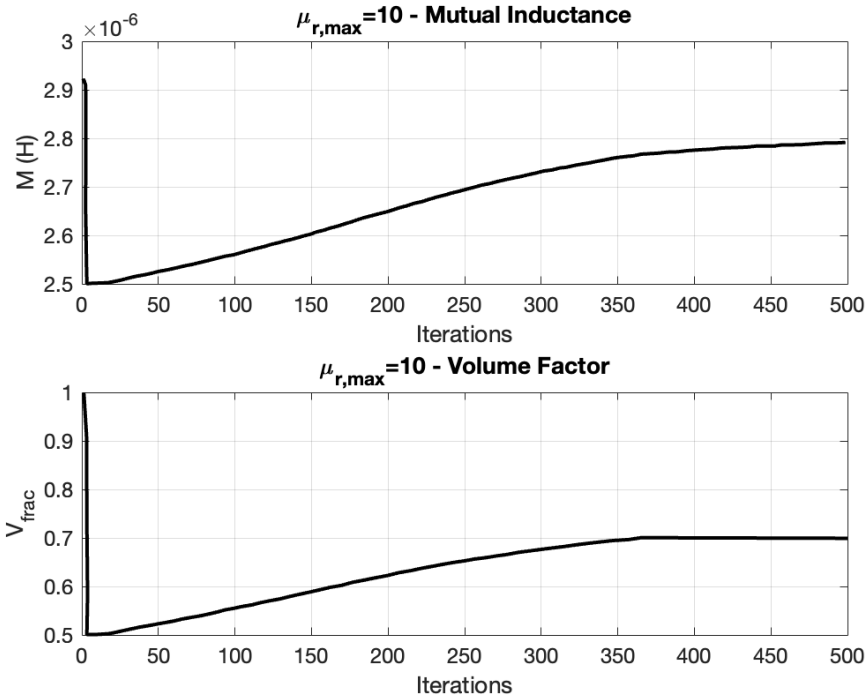

Figure 4.39. *Plots of the mutual inductance (above) and volume factor (below) for $\mu_{r,max} = 10$ with 500 iterations.*

Optimization. The value of the mutual inductance changes slowly, and the algorithm faces the challenge of determining an optimal material distribution. This observation underscores the complex interplay between material properties, magnetic characteristics, and the effectiveness of the topology optimization algorithm in attaining the specified outcomes.

As said before, in (4.15), the constraint on the volume of the design domain is set to 0.7. Fig. 4.40 shows a comparison between the Topology Optimization of the ferrite considering the constraint on $V_{frac} = 0.7$ and $V_{frac} = 0.4$ for $\mu_{r,max} = 1000$.

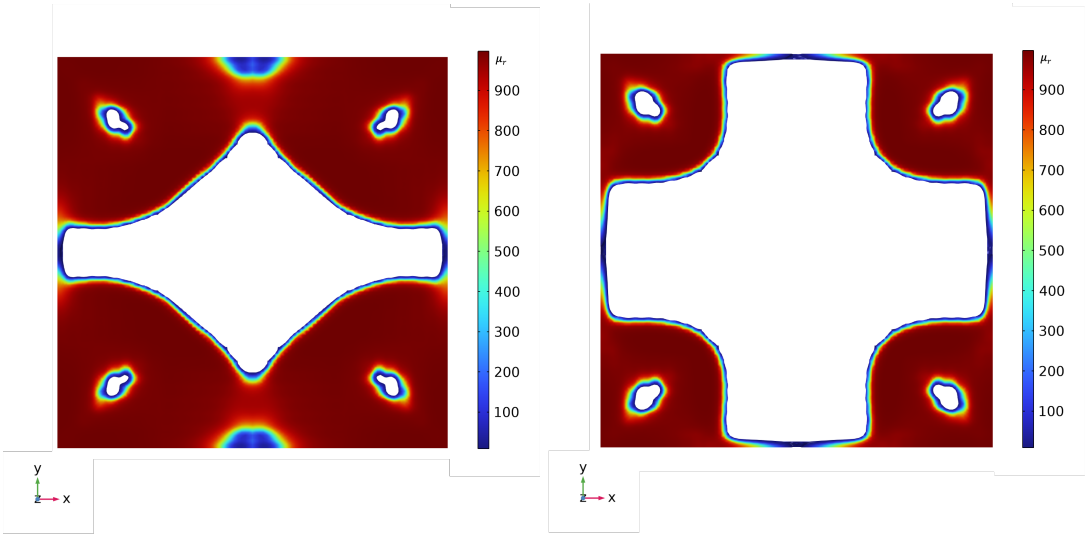

(a) **(b)**

Figure 4.40. *Material distribution during optimization produced by using $\alpha = 7$ (see (4.5)) with $V_{frac} = 0.7$ (a) and $V_{frac} = 0.4$ (b). The color bar refers to the value of μ_r.*

By diminishing the constraint on volume occupancy the material tends to be positioned on the corner of the coils. The difference lies in the volume constraint applied during the Topology Optimization process. A volume constraint of 0.7 restricts the optimized material up to 70% of the total available volume, while a constraint of 0.4 limits the optimized material to 40% of the total volume. In essence, the 0.7 constraint allows for a higher density of optimized material than the 0.4 constraint. This variation can affect the distribution and arrangement of the optimized material within the structure, potentially leading to different results in terms of the performance and behavior of the optimized structure.

Chapter 5

Conclusions and Future Works

The main objective of this work was to investigate the application of numerical methods for Topology Optimization (TO) within the realm of electromagnetic devices. Significant results have been achieved using TO, demonstrating the potential of this technique in designing innovative and optimized solutions not only in the field of structural mechanics but also in electromagnetics. In particular, the TO process was based on the Solid Isotropic Material with Penalization (SIMP) method, commonly adopted in the realm of TO for structural problems.

Utilizing the Finite Element Method (FEM) software COMSOL® Multiphysics, in-depth analyses were conducted to optimize these devices' geometry to enhance electromagnetic (EM) performance. Although the described approach can be used to carry out the TO of various electromagnetic devices, in this work the TO techniques are employed to minimize the weight of the magnetic core in the Vehicle Assembly (VA) side in electric vehicles, in the context of Wireless Power Transfer (WPT) systems. In particular, the effect of the variation of the relative permeability (μ_r) on the final results of the TO was investigated. Furthermore, from a more real perspective, innovative technologies have been analyzed to produce these optimized devices, which are hardly realizable with conventional subtractive techniques.

The use of numerical methods to investigate the effect of μ_r variability on topology optimization results is certainly an interesting outcome of this thesis. The analysis allowed to verify how changes in relative magnetic permeability affect the shape and performance of the optimized component. Furthermore, these analyses have been carried out on the basis that there are innovative manufacturing technologies available that are capable of using materials with different μ_r and realizing complex geometries.

In this thesis, single-objective problems are considered in the topology optimization framework, although multi-objective problems are of considerable interest in the scientific community, particularly in the context of WPT devices. However, the results of multi-objective analysis pose challenges, particularly in the use of gradient-based methods in optimization problems. Future research could explore the application of multi-objective optimization techniques to address the complex trade-offs inher-

ent in WPT device design. This would involve developing specialized optimization algorithms capable of efficiently navigating the multidimensional design space and identifying optimal solutions that balance conflicting objectives (i.e., Pareto optimal solutions).

Concerning the analysis of non-subtractive manufacturing techniques, a literature review was conducted regarding Additive Manufacturing (AM) technologies and their impact on the feasible implementation of TO results. AM is emerging as a promising technique for fabricating complex and customized components, offering new opportunities for translating simulation outcomes into tangible devices. Investigations have been conducted into methodologies for using materials such as ferrites and metallic compounds. Fused Deposition Modeling technique has enabled the integration of ferrite materials with high magnetic permeability. An interesting technique involves the use of UV-assisted 3D printing technologies. This work provided a comprehensive discussion of the use of topology optimization techniques in electromagnetism, supported by practical simulations and analyses. It laid the groundwork for future developments in this area, covering both device optimization and practical implementation through advanced manufacturing technologies.

References

[1] M. P. Bendsoe and O. Sigmund, *Topology optimization: theory, methods, and applications*. Springer Science & Business Media, 2003.

[2] M. P. Bendsøe and N. Kikuchi, "Generating optimal topologies in structural design using a homogenization method," *Computer methods in applied mechanics and engineering*, vol. 71, no. 2, pp. 197–224, 1988.

[3] O. Sigmund, "On the design of compliant mechanisms using topology optimization," *Journal of Structural Mechanics*, vol. 25, no. 4, pp. 493–524, 1997.

[4] A. Bandyopadhyay and S. Bose, *Additive manufacturing*. CRC press, 2019.

[5] T. DebRoy, H. Wei, J. Zuback, T. Mukherjee, J. Elmer, J. Milewski, A. M. Beese, A. d. Wilson-Heid, A. De, and W. Zhang, "Additive manufacturing of metallic components–process, structure and properties," *Progress in Materials Science*, vol. 92, pp. 112–224, 2018.

[6] T. J. Hughes, *The finite element method: linear static and dynamic finite element analysis*. Courier Corporation, 2012.

[7] K.-J. Bathe, *Finite element procedures*. Klaus-Jurgen Bathe, 2006.

[8] *COMSOL Multiphysics*. [Online]. Available: `https://www.comsol.com/`, (accessed Feb. 06, 2024).

[9] O. Bró, "Edge element formulations of eddy current problems," *Computer methods in applied mechanics and engineering*, vol. 169, no. 3-4, pp. 391–405, 1999.

[10] T. Morisue, "Magnetic vector potential and electric scalar potential in three-dimensional eddy current problem," *IEEE Transactions on magnetics*, vol. 18, no. 2, pp. 531–535, 1982.

[11] R. D. Mindlin, "Micro-structure in linear elasticity," *Archive for rational mechanics and analysis*, vol. 16, pp. 51–78, 1964.

[12] A. S. Saada, *Elasticity: theory and applications*. Elsevier, 2013, vol. 16.

[13] P. L. Gould and Y. Feng, *Introduction to linear elasticity*. Springer, 1994, vol. 2.

[14] O. C. Zienkiewicz, R. L. Taylor, and J. Z. Zhu, *The finite element method: its basis and fundamentals*. Elsevier, 2005.

[15] S. Sanogo, F. Messine, C. Henaux, and R. Vilamot, "Topology optimization for magnetic circuits dedicated to electric propulsion," *IEEE transactions on magnetics*, vol. 50, no. 12, pp. 1–13, 2014.

[16] A. Assadihaghi, S. Bila, C. Durousseau, D. Baillargeat, M. Aubourg, S. Verdeyme, M. Rochette, J. Puech, and L. Lapierre, "Design of microwave components using topology gradient optimization," in *2006 European Microwave Conference*, IEEE, 2006, pp. 462–465.

[17] T. Labbe and B. Dehez, "Convexity-oriented mapping method for the topology optimization of electromagnetic devices composed of iron and coils," *IEEE Transactions on Magnetics*, vol. 46, no. 5, pp. 1177–1185, 2009.

[18] R. El Bechari, F. Guyomarch, and S. Brisset, "The adjoint variable method for computational electromagnetics," *Mathematics*, vol. 10, no. 6, p. 885, 2022.

[19] International Organization for Standardization and ASTM International, *Additive manufacturing - General principles - Part 1: Data formats and data exchange for additive manufacturing*, Standard, 2022.

[20] V. Chaudhary, S. Mantri, R. Ramanujan, and R. Banerjee, "Additive manufacturing of magnetic materials," *Progress in Materials Science*, vol. 114, p. 100 688, 2020, ISSN: 0079-6425. DOI: https://doi.org/10.1016/j.pmatsci.2020.100688. [Online]. Available: https://www.sciencedirect.com/science/article/pii/S0079642520300529.

[21] T. D. Ngo, A. Kashani, G. Imbalzano, K. T. Nguyen, and D. Hui, "Additive manufacturing (3D printing): A review of materials, methods, applications and challenges," *Composites Part B: Engineering*, vol. 143, pp. 172–196, 2018.

[22] L. E. Murr and W. L. Johnson, "3D metal droplet printing development and advanced materials additive manufacturing," *Journal of Materials Research and Technology*, vol. 6, no. 1, pp. 77–89, 2017.

[23] D. Bourell, J. Beaman, M. Leu, and D. Rosen, *A Brief History of Additive Manufacturing and the 2009 Roadmap for Additive Manufacturing: Looking Back and Looking Ahead*, doi: 10.1016/S0190-9622(08)80898-5., 2009.

[24] T. Wohlers, T. Gornet, N. Mostow, I. Campbell, O. Diegel, J. Kowen, R. Huff, B. Stucker, I. Fidan, A. Doukas, *et al.*, "History of additive manufacturing," 2016.

[25] H. Tiismus, A. Kallaste, T. Vaimann, and A. Rassõlkin, "State of the art of additively manufactured electromagnetic materials for topology optimized electrical machines," *Additive Manufacturing*, vol. 55, p. 102 778, 2022.

[26] L.-E. Rännar, A. Glad, and C.-G. Gustafson, "Efficient cooling with tool inserts manufactured by electron beam melting," *Rapid Prototyping Journal*, vol. 13, no. 3, pp. 128–135, 2007.

[27] D. Herzog, V. Seyda, E. Wycisk, and C. Emmelmann, "Additive manufacturing of metals," *Acta Materialia*, vol. 117, pp. 371–392, 2016, ISSN: 1359-6454. DOI: https://doi.org/10.1016/j.actamat.2016.07.019. [Online]. Available: https://www.sciencedirect.com/science/article/pii/S1359645416305158.

[28] E. Sheydaeian and E. Toyserkani, "A new approach for fabrication of titanium-titanium boride periodic composite via additive manufacturing and pressureless sintering," *Composites Part B: Engineering*, vol. 138, pp. 140–148, 2018.

[29] Y. Hu, W. Cong, X. Wang, Y. Li, F. Ning, and H. Wang, "Laser deposition-additive manufacturing of TiB-Ti composites with novel three-dimensional quasi-continuous network microstructure: Effects on strengthening and toughening," *Composites Part B: Engineering*, vol. 133, pp. 91–100, 2018.

[30] L. Liu, T. Ge, K. D. Ngo, Y. Mei, and G.-Q. Lu, "Ferrite paste cured with ultraviolet light for additive manufacturing of magnetic components for power electronics," *IEEE Magnetics Letters*, vol. 9, pp. 1–5, 2018.

[31] L. Liu, T. Ge, Y. Yan, K. Ngo, and G. Lu, "UV-assisted 3D-printing of soft ferrite magnetic components for power electronics integration," in *2017 International Conference on Electronics Packaging (ICEP)*, IEEE, 2017, pp. 447–450.

[32] N. Giannotta, G. Sala, C. Bianchini, and A. Torreggiani, "A Review of Additive Manufacturing of Soft Magnetic Materials in Electrical Machines," *Machines*, vol. 11, no. 7, p. 702, 2023.

[33] Y. Bai and C. B. Williams, "An exploration of binder jetting of copper," *Rapid Prototyping Journal*, vol. 21, no. 2, pp. 177–185, 2015.

[34] D. Ramirez, L. Murr, E. Martinez, D. Hernandez, J. Martinez, B. I. Machado, F. Medina, P. Frigola, and R. Wicker, "Novel precipitate–microstructural architecture developed in the fabrication of solid copper components by additive manufacturing using electron beam melting," *Acta Materialia*, vol. 59, no. 10, pp. 4088–4099, 2011.

[35] B. Badrinarayan and J. Barlow, "Selective Laser of a Copper-PMMA System," in *1991 International Solid Freeform Fabrication Symposium*, 1991.

[36] B. Badrinarayan and J. Barlow, "Metal parts from selective laser sintering of metal-polymer powders," in *1992 International Solid Freeform Fabrication Symposium*, 1992.

[37] W. J. Sames, F. List, S. Pannala, R. R. Dehoff, and S. S. Babu, "The metallurgy and processing science of metal additive manufacturing," *International materials reviews*, vol. 61, no. 5, pp. 315–360, 2016.

[38] I. Gibson, D. Rosen, B. Stucker, I. Gibson, D. Rosen, and B. Stucker, "Directed energy deposition processes," *Additive manufacturing technologies: 3D printing, rapid prototyping, and direct digital manufacturing*, pp. 245–268, 2015.

[39] Y. Bai, G. Wagner, and C. B. Williams, "Effect of particle size distribution on powder packing and sintering in binder jetting additive manufacturing of metals," *Journal of Manufacturing Science and Engineering*, vol. 139, no. 8, p. 081 019, 2017.

[40] X. Lv, F. Ye, L. Cheng, S. Fan, and Y. Liu, "Binder jetting of ceramics: Powders, binders, printing parameters, equipment, and post-treatment," *Ceramics International*, vol. 45, no. 10, pp. 12 609–12 624, 2019.

[41] T. N. Lamichhane, L. Sethuraman, A. Dalagan, H. Wang, J. Keller, and M. P. Paranthaman, "Additive manufacturing of soft magnets for electrical machines–A review," *Materials Today Physics*, vol. 15, p. 100 255, 2020.

[42] C. L. Cramer, P. Nandwana, J. Yan, S. F. Evans, A. M. Elliott, C. Chinnasamy, and M. P. Paranthaman, "Binder jet additive manufacturing method to fabricate near net shape crack-free highly dense Fe-6.5 wt.% Si soft magnets," *Heliyon*, vol. 5, no. 11, 2019.

[43] S. Mirzababaei and S. Pasebani, "A review on binder jet additive manufacturing of 316L stainless steel," *Journal of Manufacturing and Materials Processing*, vol. 3, no. 3, p. 82, 2019.

[44] R. Dou, T. Wang, Y. Guo, and B. Derby, "Ink-jet printing of zirconia: Coffee staining and line stability," *Journal of the American Ceramic Society*, vol. 94, no. 11, pp. 3787–3792, 2011.

[45] N. Travitzky, A. Bonet, B. Dermeik, T. Fey, I. Filbert-Demut, L. Schlier, T. Schlordt, and P. Greil, "Additive manufacturing of ceramic-based materials," *Advanced engineering materials*, vol. 16, no. 6, pp. 729–754, 2014.

[46] H. Fayazfar, M. Salarian, A. Rogalsky, D. Sarker, P. Russo, V. Paserin, and E. Toyserkani, "A critical review of powder-based additive manufacturing of ferrous alloys: Process parameters, microstructure and mechanical properties," *Materials & Design*, vol. 144, pp. 98–128, 2018.

[47] M. Yakout, M. Elbestawi, and S. C. Veldhuis, "Density and mechanical properties in selective laser melting of Invar 36 and stainless steel 316L," *Journal of Materials Processing Technology*, vol. 266, pp. 397–420, 2019.

[48] X. Song, W. Zhai, R. Huang, J. Fu, M. W. Fu, and F. Li, "Metal-based 3D-printed micro parts & structures," 2022.

[49] *Dual Metal LPBF - Aerosint*. [Online]. Available: `https://aerosint.com/we-made-l-pbf-dual-metal/`, (accessed Feb. 06, 2024).

[50] H. Wong, K. Dawson, G. Ravi, L. Howlett, R. Jones, and C. Sutcliffe, "Multi-laser powder bed fusion benchmarkingInitial trials with Inconel 625," *The International Journal of Advanced Manufacturing Technology*, vol. 105, pp. 2891–2906, 2019.

[51] *LASERTEC 30 DUAL SLM - ADDITIVE MANUFACTURING Machines by DMG MORI*. [Online]. Available: `https://en.dmgmori.com/products/machines/additive-manufacturing/powder-bed/lasertec-30-slm`, (accessed Feb. 06, 2024).

[52] M. Kamariah, W. Harun, F. Ahmad, and F. Tarlochan, "Mechanical behaviours of selective laser melting 316L stainless steel," *J. Addit. Manuf. Adv. Mater.*, vol. 1, no. 1, pp. 1–18, 2020.

[53] A. Nassar and E. Reutzel, "Beyond Laser-by-Laser Additive Manufacturing-Voxel-Wise Directed Energy Deposition," in *2014 International Solid Freeform Fabrication Symposium*, University of Texas at Austin, 2015.

[54] S. A. Tofail, E. P. Koumoulos, A. Bandyopadhyay, S. Bose, L. ODonoghue, and C. Charitidis, "Additive manufacturing: Scientific and technological challenges, market uptake and opportunities," *Materials today*, vol. 21, no. 1, pp. 22–37, 2018.

[55] M. Ziaee and N. B. Crane, "Binder jetting: A review of process, materials, and methods," *Additive Manufacturing*, vol. 28, pp. 781–801, 2019.

[56] I. Rishmawi, M. Salarian, and M. Vlasea, "Tailoring green and sintered density of pure iron parts using binder jetting additive manufacturing," *Additive Manufacturing*, vol. 24, pp. 508–520, 2018.

[57] G. K. Meenashisundaram, Z. Xu, M. L. S. Nai, S. Lu, J. S. Ten, and J. Wei, "Binder jetting additive manufacturing of high porosity 316L stainless steel metal foams," *Materials*, vol. 13, no. 17, p. 3744, 2020.

[58] T. Do, T. J. Bauder, H. Suen, K. Rego, J. Yeom, and P. Kwon, "Additively manufactured full-density stainless steel 316L with binder jet printing," in *International Manufacturing Science and Engineering Conference*, American Society of Mechanical Engineers, vol. 51357, 2018, V001T01A017.

[59] C. E. Duty, V. Kunc, B. Compton, B. Post, D. Erdman, R. Smith, R. Lind, P. Lloyd, and L. Love, "Structure and mechanical behavior of Big Area Additive Manufacturing (BAAM) materials," *Rapid Prototyping Journal*, vol. 23, no. 1, pp. 181–189, 2017.

[60] F. Lorenz, J. Rudolph, and R. Wemer, "Design of 3D printed High Performance Windings for switched reluctance machines," in *2018 XIII international conference on electrical machines (ICEM)*, IEEE, 2018, pp. 2451–2457.

[61] M. Quarto, M. Carminati, and G. DUrso, "Density and shrinkage evaluation of AISI 316L parts printed via FDM process," *Materials and Manufacturing Processes*, vol. 36, no. 13, pp. 1535–1543, 2021.

[62] D. Syrlybayev, B. Zharylkassyn, A. Seisekulova, M. Akhmetov, A. Perveen, and D. Talamona, "Optimisation of strength properties of FDM printed parts–A critical review," *Polymers*, vol. 13, no. 10, p. 1587, 2021.

[63] M. Quarto, M. Carminati, G. DUrso, C. Giardini, and G. Maccarini, "Processability of metal-filament through polymer FDM machine," 2021.

[64] Y. Thompson, J. Gonzalez-Gutierrez, C. Kukla, and P. Felfer, "Fused filament fabrication, debinding and sintering as a low cost additive manufacturing method of 316L stainless steel," *Additive Manufacturing*, vol. 30, p. 100 861, 2019.

[65] C. Tosto, J. Tirillò, F. Sarasini, and G. Cicala, "Hybrid metal/polymer filaments for fused filament fabrication (FFF) to print metal parts," *Applied Sciences*, vol. 11, no. 4, p. 1444, 2021.

[66] M. Ralchev, V. Mateev, and I. Marinova, "3D printing of magnetic materials by FFF technology," in *2020 12th Electrical Engineering Faculty Conference (BulEF)*, IEEE, 2020, pp. 1–4.

[67] B. Khatri, K. Lappe, D. Noetzel, K. Pursche, and T. Hanemann, "A 3D-printable polymer-metal soft-magnetic functional composite–Development and characterization," *Materials*, vol. 11, no. 2, p. 189, 2018.

[68] E. Peng, X. Wei, T. S. Herng, U. Garbe, D. Yu, and J. Ding, "Ferrite-based soft and hard magnetic structures by extrusion free-forming," *RSC advances*, vol. 7, no. 43, pp. 27 128–27 138, 2017.

[69] S. J. Louis, B. Jan, and L. M. Willem, *Manganese zinc ferrite core*, US Patent 2,551,711, 1951.

[70] J. M. Silveyra, E. Ferrara, D. L. Huber, and T. C. Monson, "Soft magnetic materials for a sustainable and electrified world," *Science*, vol. 362, no. 6413, eaao0195, 2018.

[71] *Download-Ferroxcube*. [Online]. Available: `https://www.ferroxcube.com/en-global/download/index`, (accessed Feb. 07, 2024).

[72] KEMET Corporation, *EMC*. [Online]. Available: `https://ec.kemet.com/emc/`, (accessed Feb. 07, 2024).

[73] TDK Corporation, *Ferrites and Accessories | Products |TDK Product Center*. [Online]. Available: `https://product.tdk.com/info/en/products/ferrite/index.html`, (accessed Feb. 07, 2024).

[74] C. Ding, L. Liu, Y. Mei, K. D. T. Ngo, and G.-Q. Lu, "Magnetic paste as feedstock for additive manufacturing of power magnetics," in *2018 IEEE Applied Power Electronics Conference and Exposition (APEC)*, 2018, pp. 615–618. DOI: `10.1109/APEC.2018.8341075`.

[75] L. Liu, K. D. Ngo, and G.-Q. Lu, "Guideline for paste extrusion 3D printing of slump-free ferrite inductor cores," *Ceramics International*, vol. 47, no. 4, pp. 5803–5811, 2021.

[76] D. Mitra, R. Striker, J. Cleveland, B. D. Braaten, K. S. Kabir, A. Aqueeb, E. Burczek, S. Roy, and S. Ye, "A 3D printed microstrip patch antenna using electrifi filament for in-space manufacturing," in *2021 United States National Committee of URSI National Radio Science Meeting (USNC-URSI NRSM)*, IEEE, 2021, pp. 216–217.

[77] F. Corti, A. Reatti, L. Pugi, G. M. Lozito, A. Triviño-Cabrera, L. Luchetti, and G. Zini, "Evaluation of Additive Manufacturing for Wireless Power Transfer Applications," *IEEE Transactions on Industrial Electronics*, 2023.

[78] H. A. Eschenauer and N. Olhoff, "Topology optimization of continuum structures: A review," *Appl. Mech. Rev.*, vol. 54, no. 4, pp. 331–390, 2001.

[79] F. Lucchini, R. Torchio, V. Cirimele, P. Alotto, and P. Bettini, "Topology optimization for electromagnetics: A survey," *IEEE Access*, vol. 10, pp. 98 593–98 611, 2022.

[80] O. Sigmund and K. Maute, "Topology optimization approaches: A comparative review," *Structural and multidisciplinary optimization*, vol. 48, no. 6, pp. 1031–1055, 2013.

[81] E. Andreassen, A. Clausen, M. Schevenels, B. S. Lazarov, and O. Sigmund, "Efficient topology optimization in MATLAB using 88 lines of code," *Structural and Multidisciplinary Optimization*, vol. 43, pp. 1–16, 2011.

[82] J. Lee, J. H. Seo, and N. Kikuchi, "Topology optimization of switched reluctance motors for the desired torque profile," *Structural and multidisciplinary optimization*, vol. 42, pp. 783–796, 2010.

[83] S. Zhou, W. Li, and Q. Li, "Level-set based topology optimization for electromagnetic dipole antenna design," *Journal of Computational Physics*, vol. 229, no. 19, pp. 6915–6930, 2010.

[84] F. Campelo, J. Ramirez, and H. Igarashi, "A survey of topology optimization in electromagnetics: Considerations and current trends," *Academia*, vol. 46, p. 2010, 2010.

[85] E. Hassan, E. Wadbro, and M. Berggren, "Topology optimization of metallic antennas," *IEEE transactions on antennas and propagation*, vol. 62, no. 5, pp. 2488–2500, 2014.

[86] Y. Okamoto, R. Hoshino, S. Wakao, and T. Tsuburaya, "Improvement of torque characteristics for a synchronous reluctance motor using MMA-based topology optimization method," *IEEE transactions on magnetics*, vol. 54, no. 3, pp. 1–4, 2017.

[87] Y. Otomo and H. Igarashi, "A 3-D topology optimization of magnetic cores for wireless power transfer device," *IEEE Transactions on Magnetics*, vol. 55, no. 6, pp. 1–5, 2019.

[88] Y. Li, "Numerical methodologies for topology optimization of electromagnetic devices," Ph.D. dissertation, Sorbonne Université; Zhejiang University (Hangzhou, Chine), 2019.

[89] M. Abdalmagid, E. Sayed, M. H. Bakr, and A. Emadi, "Geometry and topology optimization of switched reluctance machines: A review," *IEEE Access*, vol. 10, pp. 5141–5170, 2022.

[90] R. El Bechari, V. Martin, F. Gillon, F. Guyomarch, S. Brisset, D. Najjar, and J.-F. Witz, "From Topology Optimization to 3D Printing of an Electromagnetic Core," *IEEE Transactions on Magnetics*, 2023.

[91] Y. Pei, L. Pichon, Y. Le Bihan, and M. Bensetti, "SIMP-method topology optimization of ferrite structures in inductive power transfer systems," *IEEE Transactions on Electromagnetic Compatibility*, 2023.

[92] S. Sanogo and F. Messine, "Topology optimization in electromagnetism using SIMP method: Issues of material interpolation schemes," *COMPEL-The international journal for computation and mathematics in electrical and electronic engineering*, vol. 37, no. 6, pp. 2138–2157, 2018.

[93] J. D. Deaton and R. V. Grandhi, "A survey of structural and multidisciplinary continuum topology optimization: Post 2000," *Structural and Multidisciplinary Optimization*, vol. 49, pp. 1–38, 2014.

[94] T. Q. Pham and S. N. Foster, "Additive manufacturing of non-homogeneous magnetic cores for electrical machines opportunities and challenges," in *2020 International Conference on Electrical Machines (ICEM)*, IEEE, vol. 1, 2020, pp. 1623–1629.

[95] P. Yla-Oijala, J. Markkanen, S. Jarvenpaa, and S. P. Kiminki, "Surface and volume integral equation methods for time-harmonic solutions of Maxwell's equations," *Progress in electromagnetics Research*, vol. 149, pp. 15–44, 2014.

[96] M. Passarotto, S. Pitassi, and R. Specogna, "Foundations of volume integral methods for eddy current problems," *Computer Methods in Applied Mechanics and Engineering*, vol. 392, p. 114 626, 2022.

[97] R. Torchio, "A volume PEEC formulation based on the cell method for electromagnetic problems from low to high frequency," *IEEE Transactions on Antennas and Propagation*, vol. 67, no. 12, pp. 7452–7465, 2019.

[98] J. Tucek, M. Capek, L. Jelinek, and O. Sigmund, "Density-Based Topology Optimization in Method of Moments: Q-Factor Minimization," *IEEE Transactions on Antennas and Propagation*, vol. 71, no. 12, pp. 9738–9751, 2023. DOI: 10.1109/TAP.2023.3321373.

[99] F. Lucchini, R. Torchio, P. Bettini, and F. Dughiero, "TopIE: An Integral Equation Tool for Topology Optimization in Electromagnetics," *IEEE Transactions on Antennas and Propagation*, 2023.

[100] N. Takahashi, S. Nakazaki, and D. Miyagi, "Optimization of electromagnetic and magnetic shielding using ON/OFF method," *IEEE Transactions on Magnetics*, vol. 46, no. 8, pp. 3153–3156, 2010.

[101] A. Thabuis, X. Ren, G. Burnand, and Y. Perriard, "Density-based topology optimization of conductor paths for windings in slotted electrical machines," in *2019 22nd International Conference on Electrical Machines and Systems (ICEMS)*, IEEE, 2019, pp. 1–6.

[102] B. B. S. Mohamodhosen, F. Gillon, M. Tounzi, and L. Chevallier, "Topology optimisation using nonlinear behaviour of ferromagnetic materials," *COMPEL-The international journal for computation and mathematics in electrical and electronic engineering*, vol. 37, no. 6, pp. 2211–2223, 2018.

[103] T. Gauthey, P. Gangl, and M. H. Hassan, "Multi-material topology optimization with continuous magnetization direction for permanent magnet synchronous reluctance motors," *arXiv preprint arXiv:2107.04825*, 2021.

[104] K. Svanberg, "The method of moving asymptotesa new method for structural optimization," *International journal for numerical methods in engineering*, vol. 24, no. 2, pp. 359–373, 1987.

[105] A. Sharma and K. Maute, "Stress-based topology optimization using spatial gradient stabilized XFEM," *Structural and Multidisciplinary Optimization*, vol. 57, pp. 17–38, 2018.

[106] A. Kawamoto, T. Matsumori, S. Yamasaki, T. Nomura, T. Kondoh, and S. Nishiwaki, "Heaviside projection based topology optimization by a PDE-filtered scalar function," *Structural and Multidisciplinary Optimization*, vol. 44, pp. 19–24, 2011.

[107] X. Qian and O. Sigmund, "Topological design of electromechanical actuators with robustness toward over-and under-etching," *Computer Methods in Applied Mechanics and Engineering*, vol. 253, pp. 237–251, 2013.

[108] R. Bosshard, "Multi-objective optimization of inductive power transfer systems for EV charging," Ph.D. dissertation, ETH Zurich, 2015.

[109] V. Cirimele, R. Torchio, A. Virgillito, F. Freschi, and P. Alotto, "Challenges in the electromagnetic modeling of road embedded wireless power transfer," *Energies*, vol. 12, no. 14, p. 2677, 2019.

[110] A. K. RamRakhyani, S. Mirabbasi, and M. Chiao, "Design and optimization of resonance-based efficient wireless power delivery systems for biomedical implants," *IEEE transactions on biomedical circuits and systems*, vol. 5, no. 1, pp. 48–63, 2010.

[111] C. Liu, K. Chau, Z. Zhang, C. Qiu, F. Lin, and T. Ching, "Multiple-receptor wireless power transfer for magnetic sensors charging on mars via magnetic resonant coupling," *Journal of Applied Physics*, vol. 117, no. 17, 2015.

[112] Y. Jang and M. M. Jovanovic, "A contactless electrical energy transmission system for portable-telephone battery chargers," *IEEE Transactions on Industrial Electronics*, vol. 50, no. 3, pp. 520–527, 2003.

[113] S. Laporte, G. Coquery, V. Deniau, A. De Bernardinis, and N. Hautiere, "Dynamic wireless power transfer charging infrastructure for future evs: From experimental track to real circulated roads demonstrations," *World Electric Vehicle Journal*, vol. 10, no. 4, p. 84, 2019.

[114] L. Sun, L. Wan, K. Liu, and X. Wang, "Cooperative-evolution-based WPT resource allocation for large-scale cognitive industrial IoT," *IEEE Transactions on Industrial Informatics*, vol. 16, no. 8, pp. 5401–5411, 2019.

[115] M. M. Rana, W. Xiang, E. Wang, X. Li, and B. J. Choi, "Internet of Things infrastructure for wireless power transfer systems," *IEEE Access*, vol. 6, pp. 19 295–19 303, 2018.

[116] Z. Zhang, H. Pang, A. Georgiadis, and C. Cecati, "Wireless power transfer–An overview," *IEEE transactions on industrial electronics*, vol. 66, no. 2, pp. 1044–1058, 2018.

[117] W. Chen, C. Liu, C. H. Lee, and Z. Shan, "Cost-effectiveness comparison of coupler designs of wireless power transfer for electric vehicle dynamic charging," *Energies*, vol. 9, no. 11, p. 906, 2016.

[118] F. Guo and I. P. Brown, "Simultaneous magnetic and structural topology optimization of synchronous reluctance machine rotors," *IEEE Transactions on Magnetics*, vol. 56, no. 10, pp. 1–12, 2020.

[119] Wireless Power Consortium, *Qi Specification Version 1.3*, Jan. 2021.

[120] Society of Automotive Engineers, *Wireless Power Transfer for Light-Duty Plug-in/Electric Vehicles and Alignment Methodology*, Aug. 2022.

[121] R. Bosshard and J. W. Kolar, "Multi-objective optimization of 50 kW/85 kHz IPT system for public transport," *IEEE Journal of Emerging and Selected Topics in Power Electronics*, vol. 4, no. 4, pp. 1370–1382, 2016.

[122] V. Cirimele, M. Diana, F. Freschi, and M. Mitolo, "Inductive power transfer for automotive applications: State-of-the-art and future trends," *IEEE Transactions on Industry Applications*, vol. 54, no. 5, pp. 4069–4079, 2018.

[123] G. A. Covic and J. T. Boys, "Modern trends in inductive power transfer for transportation applications," *IEEE Journal of Emerging and Selected topics in power electronics*, vol. 1, no. 1, pp. 28–41, 2013.

[124] S. Bandyopadhyay, P. Venugopal, J. Dong, and P. Bauer, "Comparison of magnetic couplers for IPT-based EV charging using multi-objective optimization," *IEEE Transactions on Vehicular Technology*, vol. 68, no. 6, pp. 5416–5429, 2019.

[125] S. Jeong, Y. J. Jang, and D. Kum, "Economic analysis of the dynamic charging electric vehicle," *IEEE Transactions on Power Electronics*, vol. 30, no. 11, pp. 6368–6377, 2015.

[126] V. Cirimele and F. Freschi, "Critical comparative review of international standards on wireless charging for light-duty electric vehicles," in *2023 IEEE Industry Applications Society Annual Meeting (IAS)*, 2023, pp. 1–6. DOI: 10.1109/IAS54024.2023.10406548.

[127] J. Schneider, "SAE J2954 overview and path forward," *SAE International: Warrendale, PA, USA*, 2013.

[128] A. Gil and J. Taiber, "A literature review in dynamic wireless power transfer for electric vehicles: Technology and infrastructure integration challenges," in *Sustainable Automotive Technologies 2013: Proceedings of the 5th International Conference ICSAT 2013*, Springer, 2013, pp. 289–298.

[129] R. Bosshard, U. Iruretagoyena, and J. W. Kolar, "Comprehensive evaluation of rectangular and double-D coil geometry for 50 kW/85 kHz IPT system," *IEEE Journal of Emerging and Selected Topics in Power Electronics*, vol. 4, no. 4, pp. 1406–1415, 2016.